# SURROGATE THEORY FOR HERTZIAN CONTACT PAIRS: APPLICATION TO SIMPLIFY WEAR TESTING OF CERAMIC HIP PROSTHESIS MATERIALS

by

Anthony Paul Sanders

A dissertation submitted to the faculty of
the University of Utah
in partial fulfillment of the requirements for the degree of

Doctor of Philosophy

Department of Mechanical Engineering

The University of Utah

December 2012

The University of Utah Graduate School

STATEMENT OF DISSERTATION APPROVAL

The dissertation of Anthony Paul Sanders

has been approved by the following supervisory committee members:

| | | |
|---|---|---|
| Rebecca Brannon | , Chair | 7/10/2012<br>Date Approved |
| Daniel Adams | , Member | 7/10/2012<br>Date Approved |
| Ken Monson | , Member | 7/10/2012<br>Date Approved |
| Ravi Chandran | , Member | 7/10/2012<br>Date Approved |
| Alan Lakshminarayanan | , Member | 7/10/2012<br>Date Approved |

and by Timothy Ameel, Chair of

the Department of Mechanical Engineering

and by Charles A. Wight, Dean of the Graduate School.

# ABSTRACT

This dissertation presents a series of research projects aimed at uncovering the causes of severe wear in ceramic-on-ceramic (CoC) hip prostheses and at devising novel contact and wear test methods that accurately replicate its root cause mechanics. CoC prostheses can provide lower wear rates than other types of prostheses; however, their clinical adoption has been inhibited by reports that they are liable to squeak annoyingly. Prior authors have theorized that acetabular edge loading is a precursor to squeaking. In this dissertation, one project has demonstrated the suitability of Hertzian contact theory for predicting the contact mechanics of edge-loaded CoC implants. Another project has shown that a small manufacturing artifact on the edge of ceramic acetabular liners exacerbates edge-loading wear. A third project has discovered the key to reproducing lubricated, recurrent CoC squeaking in vitro using a novel testing approach.

The culminating project has engineered a novel approach to averting the CoC squeaking problem. This project has designed and validated a new wear test method to efficiently evaluate ceramic materials' edge-loading wear performance. The new method uses simply shaped surrogate test specimens to substitute for full-scale ceramic hip implants, with the surrogates designed to accurately replicate the severe edge-loading contact stresses of the implants. Three series of wear tests were performed, one using the new approach with surrogate specimens, and the other two using a more direct but complicated approach with edge-loaded full-scale implants; each series included three different ceramic material pairs.

The first key outcome was that the surrogate test series yielded the same wear factor ranking as the two series performed using the more complicated method. The second key outcome was that the materials exhibited similar temporal trends in the measured friction force, which implies that the materials became damaged and fragmented by essentially the same mechanisms. These congruent results, comparing surrogate and full-scale test methods, demonstrate that the project has achieved its overarching objective of developing a simple, surrogate specimen wear test that will facilitate screening a larger pool of candidate new materials, at early stages in their development, for their wear performance under severe edge-loading contact stresses.

This dissertation is dedicated in memory of my high school classmate,

Dr. Elise (Lisa) Pokrzywinski Heslin.

That all could be blessed with such a good friend and rival.

TABLE OF CONTENTS

LIST OF TABLES

# ACKNOWLEDGMENTS

My faculty committee members each influenced my education and this research in their own unique way. Prof. Dan Adams, with his masterful teaching, assured me that the tenuous decision to step back onto a campus after many years' absence was the right move. Prof. Ravi Chandran has been a generous font of knowledge about his areas of expertise and a font of inspiration via his stories about our great engineering predecessors. Prof. Ken Monson has been dead accurate with each piece of advice he's shared about grants, proposals, reports, etc., and much of this project's success is due to the boost provided by his timely words. Dr. Alan Lakshminarayanan has routinely fielded crucial questions and deftly answered them by pointing me half way down the path; I owe him for his wisdom in leaving the other half for me to discover. These things I will always remember and be grateful for.

My faculty advisor, Prof. Rebecca Brannon, has been a true mentor. If that word, "mentor," meant as much in common speech as it now does to me, then that sentence alone would suffice. Yet, my experience as her student shows me that the word in the vernacular is bereft of meaning. Until I find a better word and convince the world to use it only with the respect I now hold for that word, I will simply have to live out my own sense of what a mentor is by struggling to be, to a few other persons, a fraction of the mentor that Prof. Brannon has been to me.

It has been a pleasure to work with fellow students Deepika Kakarla, Ira Tibbitts, and

Parth Dudhiya on this project. I will hold fond memories of our mutual triumphs in two arenas: the arena of ideas, where we built rockets to the moon using only markers and a whiteboard, and the arena of the laboratory, where we repeatedly proved that women and men are masters over metal and machines, mostly.

I cannot imagine a laboratory manager more keenly dedicated to students' learning and success than Jeff Kessler. The support he gave us was broad in scope and utterly reliable. Department staff members Sheila Olsen and Kiriaki Pentari kept my project administration on track while making the burden appear easier to them than it must actually have been. Dr. Brian Van Devener and Dr. Ian Harvey gave our team enthusiastic instruction and support while working in their surface science laboratory.

I owe the management at Ortho Development, especially Stan Despres, Brent Bartholomew, and Masao Okawa, my thanks for the latitude to pursue further education and this research. Virginia Sanders gave professional editorial input on many sections of this dissertation. D.K. Milovic Co. and AstroMet manufactured our custom ceramic specimens. Stephanie Siskey, Dr. Nicoli Ames, Dr. Kevin Ong, and Dr. Jorge Ochoa of Exponent contributed their expertise in biomechanical modeling. Machinists Steve Russell, Kirk Croxford, Travis Ballantyne, Steve Risely, Matt Dickinson, and Nick Oram contributed expert craftsmanship building the many fixtures used in this research.

This project was made possible by funding received from the NIH/National Institute of Arthritis and Musculoskeletal Diseases, grant number 1R21AR056374-01A1. The funding was allocated by Congress via the American Recovery and Reinvestment Act of 2009. I am dedicated to providing a positive return on the taxpayers' investment.

# CHAPTER 1

# OVERVIEW

## 1.1 Scope of research

### 1.1.1 Hip prosthesis bearing materials

Nearly all contemporary hip prosthesis bearings are made of plastic, metal, or ceramic materials. The plastic material is commonly ultra-high molecular weight polyethylene (UHMWPE) crosslinked by radiation treatment to improve its wear performance. This material is typically used only in the hip's socket component, which is variably termed as the acetabular liner or acetabular cup (or simply liner or cup) depending partly on details of its design. The metal is most frequently a Co-Cr-Mo (CoCr) alloy, and it is used in both liner and ball implants; the latter component is also called the femoral head, or simply head. Multiple ceramic materials have been used, chiefly alumina ($Al_2O_3$), zirconia ($ZrO_2$), and more recently, zirconia-toughened alumina (ZTA) and silicon nitride ($Si_3N_4$). These ceramics are employed in both head and liner components.

These implant materials have been deployed as the head and the liner in numerous different combinations, but four particular combinations stand out:

1. Metal-on-plastic (*MoP*): This type pairs a metal head with a plastic liner. Based on its historical precedence, it is sometimes considered as the "gold standard" bearing pair.
2. Ceramic-on-plastic (*CoP*): This type pairs a ceramic head with a plastic liner. Being harder and more scratch-resistant than metal, the ceramic head is purported to confer the advantage of wearing the counterface plastic less in the long term than does a metal head.
3. Metal-on-metal (*MoM*): This type mates a CoCr head with a CoCr liner. The use of a hard, metallic liner material is meant to make this type more wear resistant

than the preceding two types, whose soft plastic liner is more susceptible to being scratched and worn by asperities on the much harder ceramic or metal head.

4. Ceramic-on-ceramic (*CoC*): This type pairs a ceramic head with a ceramic liner. It is purported to be the lowest wearing of all four types [1], an advantage attributed to the ceramics' great hardness [2].

The principal aim in selecting materials for hip bearings is to maximize the longevity of the prosthesis by minimizing wear. The consequence of insufficient wear resistance may be that the hip replacement patient must undergo later surgery (called revision surgery) to replace the original implants with new ones, which is obviously an undesired outcome because of the hardship it imposes on the patient. Clinicians, engineers, and scientists have endeavored for several decades to minimize the incidence of such outcomes. Their efforts have produced these several bearing options and their specific designs in numerous commercial products from multiple manufacturers, along with myriad scientific journal articles reporting details of the implants' performance.

To set a context for the present research program, the following briefly surveys the history behind this contemporary set of material options for prosthetic hip bearings.

### 1.1.2 A concise history of major bearing types

Sir John Charnley, an orthopaedic surgeon who practiced in Wrightington, U.K., pioneered the use of plastic as a hip bearing material; he termed his novel implant design and the associated surgical technique as "low-friction arthroplasty" [3]. His first generation of MoP bearings paired a stainless steel head with a polytetrafluoroethylene (PTFE) cup. Unfortunately, these cups wore rapidly, and the wear debris commonly evoked severe in-

flammatory reactions requiring revision surgery. This unsatisfactory performance led him in 1962 to turn to UHMWPE cups. These were much more successful, as evidenced by the subsequent widespread adoption of UHMWPE as one of the principal bearing materials for arthroplasty, and also by numerous long-term clinical follow-up studies [4-6]. Nevertheless, these studies also point out that wear of the UHMWPE cup is one of the main long-term limitations [5]. UHMWPE wear is a serious problem because it can cause osteolysis [7], a harmful physiologic reaction to the UHMWPE wear particles that causes loss of bone surrounding the hip implants, which seriously complicates any revision surgery. Recognition of this issue led to the introduction in the late 1990s of UHMWPE that is expressly crosslinked by radiation exposure to improve its wear performance [8]. Hip simulator wear tests have shown that crosslinked UHMWPE can provide 80-90% reduction in wear compared to non-crosslinked UHWMPE [9-11]. One review of clinical data found that crosslinked UHMWPE results in an 87% reduction in the risk of osteolysis [12]. Mating crosslinked UHMWPE with a ceramic femoral head may convey better resistance to edge-loading damage [13] and also better wear rates than MoP due to the ceramic's smoother surface and its scratch resistance [14-16]. In 1999, fewer than 20% of liners implanted in the United States were made of crosslinked UHMWPE [17]; by 2010, that market share had risen to 83% [18].

Several authors have reviewed the history of MoM hip bearings [8,19-21]. British surgeons G. K. McKee and J. Watson-Farrar pioneered the use of these implants, and in 1966, they reported a 90% four-year success rate in their first series of 50 patients [22]. However, longer term results were poorer [23], which caused the first generation of MoM prostheses such as the McKee-Farrar to be widely abandoned during the 1970s in favor of MoP

[19,24,25]. In the late 1980s, a resurgence of MoM arthroplasty was prompted by clinical reports that some first-generation MoM arthroplasties performed as well as Charnley MoP hips at mid to long-term follow-up [26,27]. Since then, numerous manufacturers have marketed second-generation MoM designs [8], whose market share has increased during the 2000s to 16% of liners in 2008 [18]. However, a recent and growing body of literature has raised many doubts about the efficacy of MoM arthroplasties. Adverse biologic reactions to MoM bearings, such as idiopathic pain, aseptic lymphocytic lesions, joint effusion, elevated levels of metal ions in the blood serum, soft tissue necrosis, and pseudotumors have been increasingly reported [28-32]. Many reports have pointed to metallic wear debris as the cause of these problems [30,31,33-35]. In 2010, a large manufacturer issued recalls of two MoM bearing systems [36] because of an unacceptable five-year revision rate of 13% [37].

Several reviews have described the history of CoC hip bearings [8,19,38-41]. French surgeon Pierre Boutin pioneered this bearing type, implanting the first alumina-on-alumina hip prosthesis in 1970 [40]. The first generation of CoC implants used monolithic ceramic acetabular cups, and these were beset by poor pelvic fixation [42-46]. Another significant problem was a high incidence of component fracture, due to the brittle nature of ceramics and sometimes poor manufacturing quality [38,45-47]. Yet, progress with CoC implants continued because, despite these problems, many also exhibited very low wear rates [38,48,49]. The problem of poor fixation was addressed by implementing two-piece designs wherein an acetabular liner is coupled with a metallic outer shell having a coating surface designed to enhance biological fixation [2,8]. A 14-year follow up of patients with such a design showed a survivorship of 97%, considering cup loosening as the endpoint

[50]. Important advancements in the quality of alumina implants have included the refinement of grain size, the addition of hot isostatic pressing, and the implementation of overload proof testing on every unit produced, for final quality assurance [39,51]. According to one key manufacturer's implant tracking data, these changes reduced the rate of femoral head fracture from 0.026% for their first generation alumina to 0.004% for their third generation alumina manufactured after 1994 [51]. Fracture of alumina implants, including intraoperative chipping, persists as a problem even with the latest generation of materials [52-54].

Recently, the market for CoC hips has declined in apparent response to their potential to squeak annoyingly after several months' in-vivo use. In the United States, between the years 2000 and 2005, CoC implants rose in market share, from practically 0% in 2000 to a peak of 8% in 2004 and 2005; since then, their market share has fallen steadily, to 2% in 2010 [18]. Clinical reports from several series have shown incidences of squeaking or other noises varying from 2 to 21% [55-62]. Some patients endure occasional noises as a mild annoyance, but for others, the noise is bothersome enough that they insist on revision surgery. Several authors have pointed to edge loading as the likely root cause of squeaking [59,61,63,64]. As described in Chapter 3, edge loading occurs when the femoral head subluxes from the liner's intended spherical bearing surface and bears instead on the liner's edge. The propensity of edge loading to cause CoC wear was recognized via analysis of retrieved CoC hips, where the problem was associated with cup orientation and component loosening [49,65].

### 1.1.3 Research problem and opportunity

The U.S. market share of CoC hips is low considering that this bearing type has the potential to be the lowest wearing, longest lasting type of hip bearing that the field can offer to a patient. In-vitro studies have shown that CoC joints wear less than the other bearing types by a wide margin. One simulator study showed that CoC hips wore 500X less than MoP and 50X less than MoM and CoP [10]. Another showed that CoC alumina liners wore at a rate 3,000X lower than MoP UHMWPE liners [1]. Although crosslinked UHMWPE has much better wear resistance than non-crosslinked, questions persist about its long-term fatigue strength [66-68] because crosslinking is known to negatively affect that property [69,70]. Long-term oxidative degradation is another ongoing concern with UHMWPE [71-73]. Newly introduced types of UHWMPE incorporating vitamin E as an antioxidant appear to exhibit relatively durable oxidation resistance [74,75], but such materials have as yet very little clinical track record. MoM bearings are inherently subject to oxidation of their surfaces. CoCr resists corrosion due to a thin, adherent oxide layer that forms on its surface. Yet, because MoM bearings operate mainly under mixed and boundary lubrication [76,77], the oxide layer is subject to wear from counterface asperities. This leads to re-oxidation of the underlying surface, and hence a cyclic, erosive process known as tribocorrosion [78]. In contrast with both UHMWPE and CoCr, oxide ceramics exist already in their highest state of oxidation, and hence are immune to further oxidation in-vivo [79]. Weighing all of these facts, there are many reasons that CoC bearings are arguably the most advantageous of the available bearing options.

There are ancillary reasons for CoC implants' low U.S. market share. Surgeons' risk of being sued by their patients in the event of implant fracture is a likely contributing factor

[79]. Further, the history of fractures in past designs is one reason that the U.S.F.D.A. has classified CoC implants in the highest risk category for medical devices (Class III) [80,81]. This classification obliges any company desiring to market a CoC implant to investigate its performance in a lengthy clinical trial with a limited number of patients. Since clinical trials are expensive and complicated [82], companies may be reluctant to undertake them. Moreover, in the current market of declining CoC sales in the U.S., such an endeavor may be difficult to justify as a wise investment.

Young candidate patients, such as those under 50 years old, could especially benefit from an extremely low-wearing hip prosthesis whose material properties are known stable. Surgeons are naturally concerned about implant material longevity in these younger patients because they are more active and place greater demands on their implants than elderly patients [83]. Conventional wisdom has been that MoM and CoC implants were preferred for younger patients because these materials wear much less than UHMWPE and so have lower risk of osteolysis. Yet, of late, the mounting problems with MoM implants, the squeaking problem with CoC implants, and the good mid-term (e.g., 5-8 years) results with crosslinked UHMWPE hips [66,67,84,85] have resulted in declining use of MoM and CoC and increasing use of crosslinked UHMWPE. Although these UHMWPE results are cause for optimism, these reports' authors caution that longer follow-up is needed to understand the long-term performance of new UHMWPE formulations. Such caution is warranted in view of past clinical failures of UHMWPE variants that showed excellent properties in laboratory testing but performed poorly in-vivo [86-90]. The many advantages and disadvantages of the different bearing types leave room for debate about which is optimal,

especially considering the needs of young patients who wish to remain active and whose life expectancies require a hip prosthesis to endure 30 years or more of use.

This research project has focused on improving CoC bearings as a means of meeting such needs. Ceramic materials' great wear resistance and biocompatibility (including biological responses to wear debris) make them the best candidates to function as bearings in-vivo over a period of several decades [50,91]. In the past, several key problems of CoC hips have been rooted in design details unrelated to the bearing surfaces, and many of these problems have been tackled with success [50]. Walter et al. have described a design detail of contemporary ceramic liners that may make CoC bearings susceptible to edge-loading wear [92]. Hence, there appear to be design problems that could be overcome to reduce the incidence of squeaking. Also, improved surgeon training and experience could improve the accuracy of cup placement and thereby reduce edge loading and squeaking [49]. The risk of brittle fracture in alumina has been diminished by decades of material and manufacturing improvements. Recently introduced ceramic materials ZTA and Si3N4 have even greater fracture toughness (6.5 [93] and 10 MPa√m [94], respectively) than alumina (3.2 MPa√m [93]), which should further diminish the risk of fracture. Further, in a clinical trial of 177 ZTA CoC hips with an average 31-month follow-up, no patients reported squeaking noises, which suggests that new ceramics may prove to be less susceptible to this problem.

Besides these new ceramics, there are many promising developments in the ceramics field that could improve CoC hip performance. A nanocomposite ZTA has exhibited a fracture toughness of 10 MPa√m; nonetheless, its wear was greater than that of alumina in simulator wear tests [95]. This indicates that increased fracture toughness does not necessarily lead to greater wear resistance, which is important to the present research effort,

where squeaking is attributed to abnormal wear (Chapter 6). Nanostructured ceramics are typically difficult to produce because long sintering times can lead to grain enlargement. However, the technique of spark plasma sintering can overcome this limitation because it rapidly heats the ceramic powders internally via a pulsed DC current rather than externally as in typical furnace sintering processes [96]. Hard coatings or claddings may also provide advancements. Already, thin zirconium oxide coatings are used successfully in CoP hip and knee bearings [97-100]. Thick (10 μm) chromium nitride ceramic coatings on CoCr heads and liners have been tested in hip simulator wear tests with severe microseparation, and three of five specimens showed no particular edge-loading damage, whereas five of five uncoated CoCr heads exhibited wear scars up to 40 μm deep [101]. Several reports have shown the high wear resistance of diamond coatings [102-107], including a hip simulator test with both head and liner coated with 40-100 μm thick amorphous diamond [104]. A much thicker cladding (>500 μm) of polycrystalline diamond is also being investigated for self-mated hip application [108,109].

Thus, there exist numerous pathways for progress in hip bearings made of low-wearing hard materials. However, the path to clinical use for any promising innovation in this field is long and costly due to CoC hips' high-risk F.D.A. classification and to the high cost of making and testing prototype components made of advanced ceramics. Such high costs stifle the innovation needed to make advancements. They also limit the cycle of iterations that engineers should use to optimize designs. An example from the author's experience developing crosslinked UHMWPE liners helps to illustrate the cost and time burdens. This example describes the time and cost required to make and to wear test a new liner design and new crosslinked UHMWPE after the geometric and material specifications had been

completed. To manufacture the raw material required 3 months. Manufacturing the liners required an additional 2 months. Inspecting, packaging, and sterilizing the liners required 3 weeks. Then, performing the 5 Mcycle hip simulator wear test took 4 months and cost $80,000. The entire process took almost 10 months, and as a consequence, it was performed only one time, after the designs of components and material had been finalized. As such, the wear test served only as a final design assurance; in no way did it inform an iterative process that led to an optimized design. Since much of the time involved in the given example is inherent to the processes and testing needed for finalized full-scale implants, it appears that opportunities to iterate must be found earlier in the design cycle.

The present research has sought to develop ways to increase the number of engineering iterations undertaken early in the development of new materials for CoC hip bearings. The motivating premise is that more iterations, performed earlier, at an accelerated pace, will lead ultimately to greatly improved products. Taking account of this aim and this premise, along with the current state of the field, the underlying thesis of this research is outlined as follows:

1. Wear reduces the longevity of prosthetic hip bearings.
2. New and improved materials and designs are needed to limit the bearings' wear.
3. Tests for wear performance must address the most severe wear modes known.
4. Wear tests on full-scale implants can be accurately simulated using simpler tests performed on simpler, surrogate specimens.
5. The tests on surrogate specimens can be performed more rapidly, less expensively, and earlier in the design cycle, creating the opportunity to iteratively test new candidate materials, which will lead to better final products.

6. Faster in-vitro wear testing protocols can facilitate identification and elimination of causes of in-vivo service problems, such as squeaking.

Points #1 and #2 are conclusions drawn from analyzing the state of the field. Point #5 describes the desired outcome of the research. Point #6 makes a business case for the research, since reducing in-vivo problems reduces health care costs and also leads to more desirable products. In between, points #3 and #4 allude to the majority of the work reported in this dissertation. Point #3 alludes to understanding edge loading, which appears to be the most severe contact stress condition faced by CoC bearings. Point #4 alludes to the scientific hypothesis, stated below, that was the foundation for the approach taken.

### 1.1.4 Hypothesis

The failure modes of full-scale components can be reproduced in simpler, less costly material specimens by subjecting the specimens to contact stresses that mimic those in the components.

## 1.2 Research approach

This research had the following operating objectives:

1. Achieve a better understanding of the forces and stresses that arise during edge loading.
2. Apply the determined forces and stresses in wear tests of simply shaped surrogate test specimens.
3. Apply the same forces and stresses in wear tests of full-scale implants.

4. Compare the results of #2 and #3 to validate the hypothesis that the simpler specimens may be tested as surrogates for the full-scale implants.

The plan to achieve these objectives was divided into multiple phases and required multiple contributors. To organize the project's workflow and to clarify the different contributors' responsibilities, a project flowchart similar to the one in Figure 1.1 was created.

In overview, the flowchart is laid out with a leading task at the top that flows into tasks grouped into four distinct quadrants as indicated by the "Lead" and "Quad X" labels and the separate shaded backdrops The initial task was to research a means to design a simply

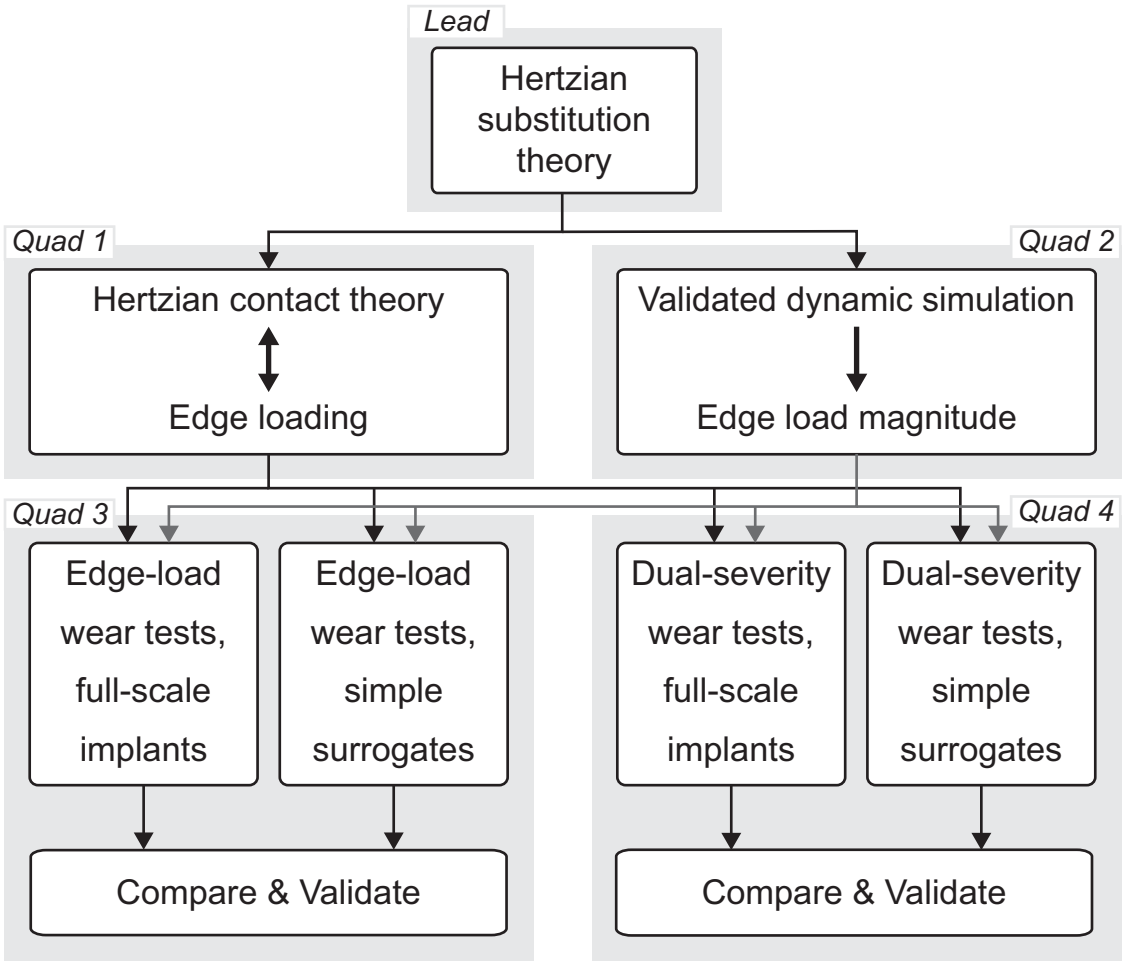


Figure 1.1. Project flowchart

shaped contact pair that could substitute for a pair composed of more complicated shapes while maintaining congruent contact mechanics between the substitutes and the originals. Since this task was a foundation for the entire project, its output flows to all lower tasks.

In Quadrant 1, the objective was to determine the suitability of Hertzian contact theory for describing the contact mechanics of edge loading. This task was a keystone in the project. Educing the range of applicability of Hertzian theory would guide physics-based design of surrogate specimens to represent edge loading. The output of this task flows to Quadrants 3 and 4 because the design of those tasks' wear test specimens would depend on this task's findings.

In Quadrant 2, the objective was to create and validate a finite-element simulation of a hip prosthesis undergoing a dynamic edge loading event and to extract from the simulation values of the contact force during the event. The output of this task flows to Quadrants 3 and 4 because the force determined would guide the choice of loads to be applied in the wear tests of those later tasks.

The objective in Quadrant 3 was to design, construct, and perform an edge-loading wear test of full-scale implants and to do the same for simpler material specimens designed as surrogates for the full-scale parts. In each test, this would be performed on three different material pairs to generate a ranking of wear performance. Then, the rankings from the two test methods would be compared. The test of surrogate specimens would be judged as a suitable surrogate test method if the two rankings matched.

The objective in Quadrant 4 was to design, construct, and perform a wear test combining edge loading and concentric articulation (the combination being termed dual-severity articulation) of full-scale implants and to do the same for a test of simpler, surrogate test

specimens. Each test would be used to rank the wear of three different material pairs, and an equivalent ranking between the two test methods would validate the test of surrogates as a suitable substitute for the test of full-scale implants.

The end objective was hence to develop two test methods applicable to simply shaped material specimens designed as surrogates for full-scale hip implants. One test method (from Quadrant 3) would focus solely on edge-loading wear, and the other method (from Quadrant 4) would merge edge loading and concentric articulation to examine the combined effects of these two distinct articulation modes. The test methods would be practical for the early stages of material development because the specimens would be simple shapes such as cylinders, spheroids, and disks. Despite their simple form, the specimen pairs would simulate the contact mechanics of more complicated full-scale components, as provided by the findings of the lead task. The simple specimen shapes would be like those that material researchers already produce in early work, and they would permit many pieces to be made at relatively low cost, so that the researchers could investigate multiple innovative materials or multiple variants of a single concept. Subjecting the materials to the severest loading condition known, edge loading, would establish a relevant and conservative standard. Only those materials appreciably surpassing the performance benchmark of current materials would become candidates for further development toward eventual testing as full-scale implants in hip simulator test machines.

Completion of this plan would thus achieve the strategic objective of fostering more cycles of design iteration – specifically, facilitating more testing of more candidate materials – in future work to develop next-generation CoC hip joints.

### 1.3 Attributions to important contributors

The described research plan was executed through a coordinated effort of several personnel. Although each of these persons received direct instructions or guidance from the author, acknowledgement of their individual accomplishments clarifies the division of labor in the project plan. Because some of the team members were also students of the University pursuing their own master's degrees, some parts of this project are described elsewhere, in those students' master's theses, rather than in this dissertation.

Parth Dudhiya provided significant early contributions to the development of the edge-loading wear test for full-scale implants, Quadrant 3 of the plan. He specified important aspects of the design, completed CAD drawings, and contracted its manufacture. Mr. Dudhiya participated in the wear testing to quantify the harmful effects of the crest existing on ceramic liners (Chapter 6). He also provided SEM analysis that pinpointed the root cause of troublesome roughness in custom-made ceramic specimens.

Deepika Kakarla and Ira Tibbitts made significant contributions to the work in Quadrant 2. Together, they helped the author to set up and perform the rod impact tests through which the team built its skills with the measurement instruments that would later be used for the dynamic edge loading test. Mr. Tibbitts made individual contributions in calibrating the instrumentation, and Ms. Kakarla made individual contributions in setting up the data acquisition system.

Ms. Kakarla made other significant contributions to Quadrant 2, which is the subject of her master's thesis [110]. She independently analyzed a rod impact experiment, and she worked with the author to perform all dynamic edge loading tests. Her thesis elaborates the experimental techniques applied in the rod impact experiment – dynamic strain

measurement, laser vibrometry, and contact area and timing measurement – which led to a well-validated finite-element model. Further, her thesis details the laboratory validation and modeling approach of a finite-element model that simulated dynamic edge loading of a CoC bearing pair. The model provided estimates of contact forces that are valuable for defining applied loads in edge-loading wear tests.

Mr. Tibbitts made other important contributions, particularly in Quadrant 4 of the plan. He designed several parts of the dual-severity test apparatus and sourced its components. He also built electronic gear and programmed the software components needed to perform tests with that apparatus. The tests that produced routine squeaking in CoC implants (Chapter 5) are the subject of his upcoming master's thesis [111]. In addition to discovering and correcting numerous friction-induced operating problems while performing repetitive edge loading tests, Mr. Tibbitts was instrumental in troubleshooting a serious calibration problem in the laser vibrometer that was used in Ms. Kakarla's rod-impact verification and validation study.

The three-dimensional finite-element modeling of the rod impact tests and the dynamic edge loading tests was contributed by Stephanie Siskey, Dr. Nicoli Ames, Dr. Kevin Ong, and Dr. Jorge Ochoa, all of Exponent, Inc. These contributors lent the project valuable expertise in biomechanical modeling, which they shared in numerous teleconferences to coordinate testing and analysis strategies. They performed the analyses to high quality standards, working closely with us to meet both their own and our verification and validation metrics driven by relatively recent ASME guidelines on quality of simulations in mechanics [112].

## 1.4 Chapter overviews

This dissertation is mostly composed of separate scientific articles that either have been published (5 articles) or will be submitted for publication (1 article). These appear unaltered in Chapters 2-7. Chapter 8 briefly describes five recommendations for further research, including some parts of Quadrant 4 which were not completed in the course of this project. Chapter 9 concludes the dissertation. The following subsections give brief overviews of Chapters 2-8 and link them to the entire project plan described in Section 1.2.

### 1.4.1 Hertzian contact theory re-examined and re-purposed: Chapter 2

This chapter is an article published in the Journal of Tribology [113] that describes the research that achieved the project's lead task. The first major part of the article reviews the geometric description of contacting surfaces that underpins Hertzian contact theory. It does this using direct vector-tensor notation, which was a novel approach that yielded a concise derivation of two key geometric propositions in Hertzian theory and emphasized their second-order accuracy. The second major part derives formulas for computing the dimensions of surrogate contact pairs and validates them with empirical tests. The derivation for a surrogate pair consisting of a spheroid and a flat plane is given in detail. The result for another type of surrogate pair, a spheroid-cylinder pair, is also given; this was the type of pair used for surrogate pair wear tests later in the project (Chapter 7). This article was published in a journal not specifically related to the field of orthopaedic implants because its subject matter would appeal to a wider audience.

### 1.4.2 A validated analytical model for edge loading of hip bearings: Chapter 3

This article, published in the Journal of Biomechanics [114], describes the work that achieved the aims of Quadrant 1 in the project plan. The research validated the hypothesis that edge loading in CoC hips can be accurately described using Hertzian contact theory. The article describes the method of analysis and the validation tests and results. A supplement to the article describes in detail the novel method – coined the "fingerprinting" technique because it was inspired from crime-scene diagnostics – invented as a means to measure very small contact patches more effectively than commercially available contact paper. Edge loading is an important topic for MoM and MoP or CoP bearings as well, and so the tests and analyses were also conducted for those bearing pairs. It was seen that MoM bearing contact patches were accurately predicted only at low loads, and that Hertzian theory gave poor predictions of CoP contact patches.

The successes in this work and the project's lead task were vital to the project. The lead task accomplished the goal of finding the means to design surrogate Hertzian contact pairs, but if edge-loaded bearings' contact mechanics were not in close agreement with Hertzian theory, then the surrogate theory could possibly be inapplicable to them. Such was not the case, per the findings in this article for CoC bearings. Taking together the positive results of the lead task and this article, it was deemed reasonable to design surrogate pairs to substitute for edge-loaded full-scale implant pairs and to use the surrogates in wear tests with confidence that their contact mechanics would closely mimic those of their full-scale counterparts.

### 1.4.3 Requisite preliminaries to dynamic contact analysis and testing: Chapter 4

This article, which was published in the proceedings of the Society for Experimental Mechanics for its 2011 annual meeting [115], describes preliminary work for Quadrant 2. The end objective of this quadrant, a validated dynamic finite-element model to analyze edge-loaded hip bearings, was judged to be a complicated task demanding new skills in measurement and analysis from multiple personnel. Therefore, a preliminary task was developed to build those skills in a simpler but relevant context before applying them to the end objective. The task was to validate a finite-element model of two slender rods impacting axially at low velocity. This article describes the work that fulfilled this task.

The article first describes the novel derivation of an analytical model for the problem. This was a Hertzian-contact-coupled system of delay differential equations describing displacement wave propagation in the two rods. Once this system was programmed in a solver, it was used as a design tool for the laboratory experiment; iterative solving yielded system inputs (e.g., impact speed and rod dimensions) and outputs (e.g., strain, contact area, and wave speed) to assure that the outputs were within the measurement capabilities of the available equipment. The article further describes the close agreement that was achieved among the results of the analytical model, the experimental measurements, and the finite-element model. This achievement prepared the team to confidently approach the more complicated biomechanical problem of dynamic edge loading. That work is detailed in Ms. Kakarla's master's thesis [110]; as it concerns this dissertation, the key result was the prediction of dynamic edge-loading contact forces in the range of 200-300 N, which became the basis for the contact force applied in the edge-loading wear tests described in Chapters 5 and 7.

### 1.4.4 Identifying a design flaw in commercial ceramic acetabular liners: Chapter 5

This chapter describes an investigation showing that a particular feature – a small, sharp "crest" – on the edge of commercial ceramic liners exacerbates edge-loading wear of CoC bearings. The article was published in the Journal of Arthroplasty [116].

In 2004, in a paper which described that edge loading causes severe wear of CoC bearings, Walter et al. identified the crest feature and postulated that it could contribute to such wear [92]. Yet, no subsequent articles had probed this hypothesis, and evidence from the ceramic liners we possessed suggested that the crest feature is typical and present in products to this day. Since the wear test apparatus we had constructed for Quadrant 3 was suited to investigating Walter's hypothesis, we undertook this study. The results in this article clearly demonstrate that the crest feature exacerbates edge-loading wear, and this knowledge is anticipated to bring about improved manufacturing standards for ceramic liners. This could be done in the short term to reduce clinical edge-loading wear with current ceramic materials, or else, the knowledge could be combined with findings on prospective new materials, obtained using the methods described in Chapter 7, to produce CoC bearings that last longer due to both design and material improvements.

### 1.4.5 In-vitro reproduction of CoC squeaking: Chapter 6

This chapter, published in the Journal of Orthopaedic Research [117], describes a study that demonstrates that a chain of events involving edge-loading wear and concentric articulation can cause squeaking in lubricated CoC bearings.

To reproduce squeaking in CoC bearings in-vitro was not originally a specific aim of the project. Nevertheless, as we developed our concepts for the dual-severity wear test

for Quadrant 4 of the project, and as we observed the results of the first edge-loading wear tests (Chapter 5), we simultaneously developed a hypothesis for the cause of in-vivo squeaking. Briefly, we hypothesized that edge-loading wear leads to wear of the concentric articulating surfaces, and the latter wear causes surface roughening that incites vibrations perceived as squeaking. Furthermore, we hypothesized that this mechanism would occur in the presence of lubrication; this point is significant because several recent articles have reproduced squeaking in-vitro under implausible dry conditions [118-120], and others have found in-vitro squeaking with lubricated conditions to be elusive [121]. Our research suggests that roughening (wear) on the interior of the liner is a missing detail that made lubricated squeaking elusive in prior research on the subject.

Our achievement of lubricated, recurrent CoC squeaking led to an illustrated, qualitative theory which explains that squeaking evolves as progressive roughening of both concentric bearing surfaces causes asperity impacts that generate component vibrations that eventually rise to a critical, resonance-inducing magnitude. The article concludes with key guidelines for future tests that will aim to investigate CoC wear with conditions that could realistically evoke squeaking. These guidelines could be implemented, for example, in wear tests that would demonstrate that prospective new materials, shown via the methods in Chapter 7 to perform better under edge loading conditions, have a reduced propensity to squeak.

### 1.4.6 Ranking ceramic wear couples with surrogate specimens: Chapter 7

This chapter culminates the research program, as it reports on the ranking wear tests performed on surrogate pairs and full-scale, edge-loaded CoC pairs (Quadrant 3). The ar-

ticle will be submitted for publication in the Journal of Orthopaedic Research, in particular, for review and consideration for the Orthopaedic Research Society's annual William H. Harris Award, which recognizes outstanding research dedicated to furthering understanding of the hip.

The aim of this work was to validate a wear test that uses simple surrogate test specimens to reproduce the wear mechanisms of CoC hip implant edge loading. The surrogate specimens were designed on the basis of the Hertzian substitution theory developed in the project's lead task, combined with the observation in Quadrant 1 (Chapter 3) that CoC edge loading can be accurately estimated using Hertzian contact theory. The force magnitudes used in the wear tests were similar to those determined in the biomechanical edge-loading simulation of Quadrant 2 (Ms. Kakarla's master's thesis [110]). The surrogates were tested in three different material pairs, and full-scale, edge-loaded components were tested in the same three pairs. The criterion for validating the surrogate test was that the wear ranking it produced would match that from the full-scale component test.

The key result was twofold. First, the wear ranking yielded by the surrogates was identical to that of the full-scale implants. Second, during the wear tests, the friction force that evolved in the surrogates exhibited a trend that closely mimicked the trend in the full-scale implants. These congruent results in two important tribological measures imply that the surrogate test method elicited essentially the same wear mechanisms as the more complicated test method involving full-scale implants. This endorses the utility of the surrogate test method for screening candidate new materials for CoC hip bearings, thus fulfilling the project's overarching objective to develop rapid materials testing protocols. The ultimate benefit is a broadening of the design space to accommodate more speculative materials

choices, thereby potentially producing better hip prostheses with reduced research and development expenditures.

### 1.4.7 Opportunities for further advancements: Chapter 8

This chapter describes several recommendations for further work to advance the outcomes of this dissertation. The following list summarizes three of those recommendations.

1. Perform dual-severity wear testing that ranks multiple material pairs. This project has not achieved the full aims of Quadrant 4; dual-severity wear testing was performed only on full-scale implants, to investigate the emergence of squeaking. The apparatus has been designed and built for ranking tests of simple surrogate components, and many such components have already been made.
2. Pursue further simplification of the surrogate edge loading test. In the cylinder-spheroid pair, the spheroid is difficult to make, but the cylinder is much simpler. A cylinder-cylinder pair composed of the very cylinders already made will represent the contact stress distribution of the middle cross-section of the cylinder-spheroid pair, and that is the worst-case section of the contact stress field. Extra cylinders were made for this purpose, and they are ready to test.
3. Rank different material pairs for squeaking performance. Full-scale components in multiple materials are available for testing in the dual-severity test that produced squeaking in-vitro. It would be of value to quantify the squeaking performance of multiple material pairs in that test method.

## 1.5 References

[1] Clarke, I. C., Good, V., Williams, P., Schroeder, D., Anissian, L., Stark, A., Oonishi, H., Schuldies, J., and Gustafson, G., 2000, "Ultra-Low Wear Rates for Rigid-on-Rigid Bearings in Total Hip Replacements," Proc Inst Mech Eng H, 214(4), pp. 331-47.

[2] Clarke, I. C., 1992, "Role of Ceramic Implants. Design and Clinical Success with Total Hip Prosthetic Ceramic-to-Ceramic Bearings," Clin Orthop, 282, pp. 19-30.

[3] Kurtz, S. M., 2009, UHMWPE Biomaterials Handbook, Academic Press, Burlington, MA, "The Origins of UHMWPE in Total Hip Arthroplasty," pp. 31-41.

[4] Wroblewski, B. M., Siney, P. D., and Fleming, P. A., 2007, "Charnley Low-Friction Arthroplasty: Survival Patterns to 38 Years," J Bone Joint Surg Br, 89-B(8), pp. 1015-18.

[5] Wroblewski, B. M., Fleming, P. A., and Siney, P. D., 1999, "Charnley Low-Frictional Torque Arthroplasty of the Hip: 20- to 30-Year Results," J Bone Joint Surg Br, 81-B(3), pp. 427-30.

[6] Callaghan, J. J., Bracha, P., Liu, S. S., Piyaworakhun, S., Goetz, D. D., and Johnston, R. C., 2009, "Survivorship of a Charnley Total Hip Arthroplasty. A Concise Follow-up, at a Minimum of Thirty-Five Years, of Previous Reports," J Bone Joint Surg Am, 91(11), pp. 2617-21.

[7] Willert, H. G., Bertram, H., and Buchhorn, G. H., 1990, "Osteolysis in Alloarthroplasty of the Hip. The Role of Ultra-High Molecular Weight Polyethylene Wear Particles," Clin Orthop, 258, pp. 95-107.

[8] Kurtz, S. M., and Ong, K., 2009, UHMWPE Biomaterials Handbook, Academic Press, Burlington, MA, "Contemporary Total Hip Arthroplasty: Hard-on-Hard Bearings and Highly Crosslinked UHMWPE," pp. 55-79.

[9] D'Lima, D. D., Hermida, J. C., Chen, P. C., and Colwell Jr, C. W., 2003, "Polyethylene Cross-Linking by Two Different Methods Reduces Acetabular Liner Wear in a Hip Joint Wear Simulator," J Orthop Res, 21(5), pp. 761-66.

[10] Essner, A., Sutton, K., and Wang, A., 2005, "Hip Simulator Wear Comparison of Metal-on-Metal, Ceramic-on-Ceramic and Crosslinked UHMWPE Bearings," Wear, 259(7-12), pp. 992-5.

[11] Galvin, A. L., Tipper, J. L., Jennings, L. M., Stone, M. H., Jin, Z. M., Ingham, E., and Fisher, J., 2007, "Wear and Biological Activity of Highly Crosslinked Polyethylene in the Hip under Low Serum Protein Concentrations," Proc Inst Mech Eng H, 221(1), pp. 1-10.

[12] Kurtz, S., Gawel, H., and Patel, J., 2011, "History and Systematic Review of Wear and Osteolysis Outcomes for First-Generation Highly Crosslinked Polyethylene," Clin Orthop, 469(8), pp. 2262-77.

[13] Williams, S., Butterfield, M., Stewart, T., Ingham, E., Stone, M., and Fisher, J., 2003, "Wear and Deformation of Ceramic-on-Polyethylene Total Hip Replacements with Joint Laxity and Swing Phase Microseparation," Proc Inst Mech Eng H, 217(2), pp. 147-53.

[14] Bistolfi, A., and Bellare, A., 2011, "The Relative Effects of Radiation Crosslinking and Type of Counterface on the Wear Resistance of Ultrahigh-Molecular-Weight Polyethylene," Acta Biomater, 7(9), pp. 3398-403.

[15] Liao, Y. S., Greer, K., and Alberts, A., 2008, "Effect of Head Material and Roughness on the Wear of 7.5 Mrad Crosslinked-Remelted UHMWPE Acetabular Inserts," 54th Annual Meeting of the Orthopaedic Research Society, San Francisco, CA.

[16] Kim, Y. H., 2005, "Comparison of Polyethylene Wear Associated with Cobalt-Chromium and Zirconia Heads after Total Hip Replacement. A Prospective, Randomized Study," J Bone Joint Surg Am, 87(8), pp. 1769-76.

[17] 2003, "Hospital Resources and Implant Cost Management - a 2002 Update," Orthopedic Network News, S. Mendenhall, ed., Mendenhall Associates, Ann Arbor, MI, 14(3), pp. 9-15.

[18] 2011, "Hospital Resources and Implant Cost Management - a 2010 Update," Orthopaedic Network News, S. Mendenhall, ed., Mendenhall Associates, Ann Arbor, MI, 22(3), pp. 9-19.

[19] Zywiel, M. G., Sayeed, S. A., Johnson, A. J., Schmalzried, T. P., and Mont, M. A., 2011, "State of the Art in Hard-on-Hard Bearings: How Did We Get Here and What Have We Achieved?," Expert Rev Med Devices, 8(2), pp. 187-207.

[20] Shetty, V., and Villar, R., 2006, "Development and Problems of Metal-on-Metal Hip Arthroplasty," Proc Inst Mech Eng H, 220(2), pp. 371-77.

[21] Isaac, G. H., Thompson, J., Williams, S., and Fisher, J., 2006, "Metal-on-Metal Bearings Surfaces: Materials, Manufacture, Design, Optimization, and Alternatives," Proc Inst Mech Eng H, 220(2), pp. 119-33.

[22] McKee, G. K., and Watson-Farrar, J., 1966, "Replacement of Arthritic Hips by the McKee-Farrar Prosthesis," J Bone Joint Surg Br, 48(2), pp. 245-59.

[23] August, A. C., Aldam, C. H., and Pynsent, P. B., 1986, "The McKee-Farrar Hip Arthroplasty. A Long-Term Study," J Bone Joint Surg Br, 68(4), pp. 520-7.

[24] Muller, M. E., 1995, "The Benefits of Metal-on-Metal Total Hip Replacements," Clin Orthop, 311, pp. 54-9.

[25] Zahiri, C. A., Schmalzried, T. P., Ebramzadeh, E., Szuszczewicz, E. S., Salib, D., Kim, C., and Amstutz, H. C., 1999, "Lessons Learned from Loosening of the McKee-Farrar Metal-on-Metal Total Hip Replacement," J Arthroplasty, 14(3), pp. 326-32.

[26] Djerf, K., and Wahlstrom, O., 1986, "Total Hip Replacement Comparison between the McKee-Farrar and Charnley Prostheses in a 5-Year Follow-up Study," Arch Orthop Trauma Surg, 105(3), pp. 158-62.

[27] Jacobsson, S. A., Djerf, K., and Wahlstrom, O., 1990, "A Comparative Study between McKee-Farrar and Charnley Arthroplasty with Long-Term Follow-up Periods," J Arthroplasty, 5(1), pp. 9-14.

[28] Campbell, P., Beaule, P. E., Ebramzadeh, E., Leduff, M., De Smet, K., Lu, Z., and Amstutz, H. C., 2006, "The John Charnley Award: A Study of Implant Failure in Metal-on-Metal Surface Arthroplasties," Clin Orthop, 453, pp. 35-46.

[29] Mikhael, M. M., Hanssen, A. D., and Sierra, R. J., 2009, "Failure of Metal-on-Metal Total Hip Arthroplasty Mimicking Hip Infection. A Report of Two Cases," J Bone Joint Surg Am, 91(2), pp. 443-46.

[30] Kwon, Y. M., Glyn-Jones, S., Simpson, D. J., Kamali, A., Mclardy-Smith, P., Gill, H. S., and Murray, D. W., 2010, "Analysis of Wear of Retrieved Metal-on-Metal Hip Resurfacing Implants Revised Due to Pseudotumours," J Bone Joint Surg Br, 92(3), pp. 356-61.

[31] Langton, D. J., Jameson, S. S., Joyce, T. J., Hallab, N. J., Natu, S., and Nargol, A. V., 2010, "Early Failure of Metal-on-Metal Bearings in Hip Resurfacing and Large-Diameter Total Hip Replacement: A Consequence of Excess Wear," J Bone Joint Surg Br, 92(1), pp. 38-46.

[32] Huber, M., Reinisch, G., Zenz, P., Zweymuller, K., and Lintner, F., 2010, "Postmortem Study of Femoral Osteolysis Associated with Metal-on-Metal Articulation in Total Hip Replacement: An Analysis of Nine Cases," J Bone Joint Surg Am, 92(8), pp. 1720-31.

[33] Goodman, S. B., 2007, "Wear Particles, Periprosthetic Osteolysis and the Immune System," Biomaterials, 28(34), pp. 5044-8.

[34] Glyn-Jones, S., Roques, A., Taylor, A., Kwon, Y. M., Mclardy-Smith, P., Gill, H. S., Walter, W., Tuke, M., and Murray, D., 2011, "The in Vivo Linear and Volumetric Wear of Hip Resurfacing Implants Revised for Pseudotumor," J Bone Joint Surg Am, 93(23), pp. 2180-8.

[35] Polyzois, I., Nikolopoulos, D., Michos, I., Patsouris, E., and Theocharis, S., 2012, "Local and Systemic Toxicity of Nanoscale Debris Particles in Total Hip Arthroplasty," J Appl Toxicol, 32(4), pp. 255-69.

[36] Singer, N., 2010, "Johnson&Johnson Recalls Hip Implants", The New York Times, Aug. 27, 2010.

[37] Otsuka, A., Sugawara, H., and Shomura, M., 1996, "A Test Method for Mode II Fatigue Crack Growth Relating to a Model for Rolling Contact Fatigue," Fatigue & Fracture of Engineering Materials & Structures, 19(10), pp. 1265-75.

[38] Mittelmeier, H., and Heisel, J., 1992, "Sixteen-Years' Experience with Ceramic Hip Prostheses," Clin Orthop, 282, pp. 64-72.

[39] Heros, R. J., and Willman, G., 1998, "Ceramics in Total Hip Arthroplasty: History, Mechanical Properties, Clinical Results, and Current Manufacturing State of the Art," Seminars in Arthroplasty, 9(2), pp. 114-22.

[40] Sedel, L., 2000, "Total Hip Arthroplasty Using a Ceramic Prosthesis. Pierre Boutin (1924-1989)," Clin Orthop, 379, pp. 3-11.

[41] Hannouche, D., Zaoui, A., Zadegan, F., Sedel, L., and Nizard, R., 2011, "Thirty Years of Experience with Alumina-on-Alumina Bearings in Total Hip Arthroplasty," Int Orthop, 35(2), pp. 207-13.

[42] Boutin, P., Christel, P., Dorlot, J. M., Meunier, A., De Roquancourt, A., Blanquaert, D., Herman, S., Sedel, L., and Witvoet, J., 1988, "The Use of Dense Alumina-Alumina Ceramic Combination in Total Hip Replacement," J Biomed Mater Res, 22(12), pp. 1203-32.

[43] Jacob, H. A., and Schreiber, A., 1985, "[Erosion with Loosening of an Aluminum Oxide Ceramic Acetabulum. Case Report]," Z Orthop Ihre Grenzgeb, 123(5), pp. 803-7.

[44] Sedel, L., Christel, P., Kerboull, L., and Witvoet, J., 1990, "[Total Hip Prosthesis in Patients Less Than 50 Years of Age. Value of Ceramic Materials]," Rev Rhum Mal Osteoartic, 57(9), pp. 605-11.

[45] Winter, M., Griss, P., Scheller, G., and Moser, T., 1992, "Ten- to 14-Year Results of a Ceramic Hip Prosthesis," Clin Orthop, 282, pp. 73-80.

[46] Nizard, R. S., Sedel, L., Christel, P., Meunier, A., Soudry, M., and Witvoet, J., 1992, "Ten-Year Survivorship of Cemented Ceramic-Ceramic Total Hip Prosthesis," Clin Orthop, 282, pp. 53-63.

[47] Piconi, C., Labanti, M., Magnani, G., Caporale, M., Maccauro, G., and Magliocchetti, G., 1999, "Analysis of a Failed Alumina THR Ball Head," Biomaterials, 20(18), pp. 1637-46.

[48] Boutin, P., and Blanquaert, D., 1981, "[a Study of the Mechanical Properties of Alumina-on-Alumina Total Hip Prosthesis (Author's Transl)]," Rev Chir Orthop Reparatrice Appar Mot, 67(3), pp. 279-87.

[49] Dorlot, J. M., Christel, P., and Meunier, A., 1989, "Wear Analysis of Retrieved Alumina Heads and Sockets of Hip Prostheses," J Biomed Mater Res, 23(A3 Suppl), pp. 299-310.

[50] Sedel, L., and Raould, A., 2007, "Engineering Aspect of Alumina on Alumina Hip Prosthesis," Proc Inst Mech Eng H, 221(1), pp. 21-27.

[51] Willmann, G., 2000, “Ceramic Femoral Head Retrieval Data,” Clin Orthop, 379, pp. 22-28.

[52] Lusty, P. J., Tai, C. C., Sew-Hoy, R. P., Walter, W. L., Walter, W. K., and Zicat, B. A., 2007, “Third-Generation Alumina-on-Alumina Ceramic Bearings in Cementless Total Hip Arthroplasty,” J Bone Joint Surg Am, 89(12), pp. 2676-83.

[53] Poggie, R. A., Turgeon, T. R., and Coutts, R. D., 2007, “Failure Analysis of a Ceramic Bearing Acetabular Component,” J Bone Joint Surg Am, 89(2), pp. 367-75.

[54] D’Antonio, J., Capello, W., Manley, M., Naughton, M., and Sutton, K., 2005, “Alumina Ceramic Bearings for Total Hip Arthroplasty: Five-Year Results of a Prospective Randomized Study,” Clin Orthop, 436, pp. 164-71.

[55] Schroder, D., Bornstein, L., Bostrom, M. P., Nestor, B. J., Padgett, D. E., and Westrich, G. H., 2011, “Ceramic-on-Ceramic Total Hip Arthroplasty: Incidence of Instability and Noise,” Clin Orthop, 469(2), pp. 437-42.

[56] Jagt, D. R., Mokete, L., Gelbart, B. R., Nwokeyi, K., and Schepers, A., 2011, Tribology in Total Hip Arthroplasty, Springer, Berlin, “Noise Emissions in Total Hip Replacements, with an Emphasis on Ceramic-on-Ceramic and Ceramic-on-Metal Bearings and Different Articular Sizes,” pp. 85-90.

[57] Cogan, A., Nizard, R., and Sedel, L., 2011, “Occurrence of Noise in Alumina-on-Alumina Total Hip Arthroplasty. A Survey on 284 Consecutive Hips,” Orthop Trauma Surg Res, 97(2), pp. 206-10.

[58] Restrepo, C., Post, Z. D., Kai, B., and Hozack, W. J., 2010, “The Effect of Stem Design on the Prevalence of Squeaking Following Ceramic-on-Ceramic Bearing Total Hip Arthroplasty,” J Bone Joint Surg Am, 92(3), pp. 550-57.

[59] Mai, K., Verioti, C., Ezzet, K. A., Copp, S. N., Walker, R. H., and Colwell, C. W., Jr., 2010, “Incidence of ‘Squeaking’ after Ceramic-on-Ceramic Total Hip Arthroplasty,” Clin Orthop, 468(2), pp. 413-17.

[60] Varnum, C., Vester, T., Revald, P., and Kjaersgaard-Andersen, P., 2008, “Ceramic Bearings in Total Hip Arthroplasty: Frequency and Types of Noises,” 9th Congress of the European Federation of National Associations of Orthopaedics and Traumatology, Nice, France.

[61] Restrepo, C., Parvizi, J., Kurtz, S. M., Sharkey, P. F., Hozack, W. J., and Rothman, R. H., 2008, “The Noisy Ceramic Hip: Is Component Malpositioning the Cause?,” J Arthroplasty, 23(5), pp. 643-49.

[62] Keurentjes, J. C., Kuipers, R. M., Wever, D. J., and Schreurs, B. W., 2008, “High Incidence of Squeaking in THAs with Alumina Ceramic-on-Ceramic Bearings,” Clin Orthop, 466(6), pp. 1438-43.

[63] Walter, W. L., Waters, T. S., Gillies, M., Donohoo, S., Kurtz, S. M., Ranawat, A. S., Hozack, W. J., and Tuke, M. A., 2008, "Squeaking Hips," J Bone Joint Surg Am, 90(Supplement_4), pp. 102-11.

[64] Sariali, E., Stewart, T., Jin, Z., and Fisher, J., 2010, "Three-Dimensional Modeling of in Vitro Hip Kinematics under Micro-Separation Regime for Ceramic on Ceramic Total Hip Prosthesis: An Analysis of Vibration and Noise," J Biomech, 43(2), pp. 326-33.

[65] Kummer, F. J., Stuchin, S. A., and Frankel, V. H., 1990, "Analysis of Removed Autophor Ceramic-on-Ceramic Components," J Arthroplasty, 5(1), pp. 28-33.

[66] Mutimer, J., Devane, P. A., Adams, K., and Horne, J. G., 2010, "Highly Crosslinked Polyethylene Reduces Wear in Total Hip Arthroplasty at 5 Years," Clin Orthop, 468(12), pp. 3228-33.

[67] McCalden, R. W., Macdonald, S. J., Rorabeck, C. H., Bourne, R. B., Chess, D. G., and Charron, K. D., 2009, "Wear Rate of Highly Cross-Linked Polyethylene in Total Hip Arthroplasty. A Randomized Controlled Trial," J Bone Joint Surg Am, 91(4), pp. 773-82.

[68] Calvert, G. T., Devane, P. A., Fielden, J., Adams, K., and Horne, J. G., 2009, "A Double-Blind, Prospective, Randomized Controlled Trial Comparing Highly Cross-Linked and Conventional Polyethylene in Primary Total Hip Arthroplasty," J Arthroplasty, 24(4), pp. 505-10.

[69] Cole, J. C., Lemons, J. E., and Eberhardt, A. W., 2002, "Gamma Irradiation Alters Fatigue-Crack Behavior and Fracture Toughness in 1900h and GUR 1050 UHMWPE," J Biomed Mater Res, 63(5), pp. 559-66.

[70] Baker, D. A., Bellare, A., and Pruitt, L., 2003, "The Effects of Degree of Crosslinking on the Fatigue Crack Initiation and Propagation Resistance of Orthopedic-Grade Polyethylene," J Biomed Mater Res A, 66A(1), pp. 146-54.

[71] Medel, F. J., Kurtz, S. M., Hozack, W. J., Parvizi, J., Purtill, J. J., Sharkey, P. F., Macdonald, D., Kraay, M. J., Goldberg, V., and Rimnac, C. M., 2009, "Gamma Inert Sterilization: A Solution to Polyethylene Oxidation?," J Bone Joint Surg Am, 91(4), pp. 839-49.

[72] Currier, B. H., Currier, J. H., Mayor, M. B., Lyford, K. A., Collier, J. P., and Van Citters, D. W., 2007, "Evaluation of Oxidation and Fatigue Damage of Retrieved Crossfire Polyethylene Acetabular Cups," J Bone Joint Surg Am, 89(9), pp. 2023-9.

[73] Costa, L., and Bracco, P., 2009, UHMWPE Biomaterials Handbook, Academic Press, Burlington, MA, "Mechanisms of Crosslinking, Oxidative Degradation, and Stabilization of UHMWPE," pp. 309-23.

[74] Lerf, R., Zurbrugg, D., and Delfosse, D., 2010, "Use of Vitamin E to Protect Cross-Linked UHMWPE from Oxidation," Biomaterials, 31(13), pp. 3643-8.

[75] Bracco, P., and Oral, E., 2011, "Vitamin E-Stabilized UHMWPE for Total Joint Implants: A Review," Clin Orthop, 469(8), pp. 2286-93.

[76] Chan, F. W., Bobyn, J. D., Medley, J. B., Krygier, J. J., and Tanzer, M., 1999, "The Otto Aufranc Award. Wear and Lubrication of Metal-on-Metal Hip Implants," Clin Orthop, 369, pp. 10-24.

[77] Dowson, D., and Jin, Z. M., 2006, "Metal-on-Metal Hip Joint Tribology," Proc Inst Mech Eng H, 220(2), pp. 107-18.

[78] Figueiredo-Pina, C. G., Yan, Y., Neville, A., and Fisher, J., 2008, "Understanding the Differences between the Wear of Metal-on-Metal and Ceramic-on-Metal Total Hip Replacements," Proc Inst Mech Eng H, 222(3), pp. 285-96.

[79] Hannouche, D., Hamadouche, M., Nizard, R., Bizot, P., Meunier, A., and Sedel, L., 2005, "Ceramics in Total Hip Replacement," Clin Orthop, 430, pp. 62-71.

[80] Van Eck, C. F., Chen, A. F., Klatt, B. A., D'Antonio, J., and Fu, F., 2009, "The Classification of Implants: Class I, II, III," J Long Term Eff Med Implants, 19(3), pp. 185-93.

[81] Sheth, U., Nguyen, N. A., Gaines, S., Bhandari, M., Mehlman, C. T., and Klein, G., 2009, "New Orthopedic Devices and the FDA," J Long Term Eff Med Implants, 19(3), pp. 173-84.

[82] Kaplan, A. V., Baim, D. S., Smith, J. J., Feigal, D. A., Simons, M., Jefferys, D., Fogarty, T. J., Kuntz, R. E., and Leon, M. B., 2004, "Medical Device Development," Circulation, 109(25), pp. 3068-72.

[83] Mcauley, J. P., Szuszczewicz, E. S., Young, A., and Engh, C. A., Sr., 2004, "Total Hip Arthroplasty in Patients 50 Years and Younger," Clin Orthop, 418, pp. 119-25.

[84] Rajadhyaksha, A. D., Brotea, C., Cheung, Y., Kuhn, C., Ramakrishnan, R., and Zelicof, S. B., 2009, "Five-Year Comparative Study of Highly Cross-Linked (Crossfire) and Traditional Polyethylene," J Arthroplasty, 24(2), pp. 161-67.

[85] Geerdink, C. H., Grimm, B., Vencken, W., Heyligers, I. C., and Tonino, A. J., 2009, "Cross-Linked Compared with Historical Polyethylene in THA: An 8-Year Clinical Study," Clin Orthop, 467(4), pp. 979-84.

[86] Kurtz, S. M., Muratoglu, O. K., Evans, M., and Edidin, A. A., 1999, "Advances in the Processing, Sterilization, and Crosslinking of Ultra-High Molecular Weight Polyethylene for Total Joint Arthroplasty," Biomaterials, 20(18), pp. 1659-88.

[87] Livingston, B. J., Chmell, M. J., Spector, M., and Poss, R., 1997, "Complications of Total Hip Arthroplasty Associated with the Use of an Acetabular Component with a Hylamer Liner," J Bone Joint Surg Am, 79(10), pp. 1529-38.

[88] Wright, T. M., Astion, D. J., Bansal, M., Rimnac, C. M., Green, T., Insall, J. N., and Robinson, R. P., 1988, "Failure of Carbon Fiber-Reinforced Polyethylene Total Knee-Replacement Components. A Report of Two Cases," J Bone Joint Surg Am, 70(6), pp. 926-32.

[89] Bloebaum, R. D., Nelson, K., Dorr, L. D., Hofmann, A. A., and Lyman, D. J., 1991, "Investigation of Early Surface Delamination Observed in Retrieved Heat-Pressed Tibial Inserts," Clin Orthop Relat Res, 269, pp. 120-7.

[90] Engh, G., Dwyer, K., and Hanes, C., 1992, "Polyethylene Wear of Metal-Backed Tibial Components in Total and Unicompartmental Knee Prostheses," J Bone Joint Surg Br, 74-B(1), pp. 9-17.

[91] Fisher, J., Jin, Z., Tipper, J., Stone, M., and Ingham, E., 2006, "Tribology of Alternative Bearings," Clin Orthop, 453, pp. 25-34.

[92] Walter, W. L., Insley, G. M., Walter, W. K., and Tuke, M. A., 2004, "Edge Loading in Third Generation Alumina Ceramic-on-Ceramic Bearings: Stripe Wear," J Arthroplasty, 19(4), pp. 402-13.

[93] "Biolox Delta - Nanocomposite for Arthroplasty," Ceramtec AG, Plochingen, Germany.

[94] Bal, B. S., Khandkar, A., Lakshminarayanan, R., I., C., Hoffman, A. A., and Rahaman, M. N., 2008, "Testing of Silicon Nitride Ceramic Bearings for Total Hip Arthroplasty," J Biomed Mater Res B Appl Biomater, 87B(2), pp. 447-54.

[95] Affatato, S., Torrecillas, R., Taddei, P., Rocchi, M., Fagnano, C., Ciapetti, G., and Toni, A., 2006, "Advanced Nanocomposite Materials for Orthopaedic Applications. I. A Long-Term in Vitro Wear Study of Zirconia-Toughened Alumina," J Biomed. Mater Res B Appl Biomater, 78(1), pp. 76-82.

[96] Hungría, T., Galy, J., and Castro, A., 2009, "Spark Plasma Sintering as a Useful Technique to the Nanostructuration of Piezo-Ferroelectric Materials," Adv Eng Mater, 11(8), pp. 615-31.

[97] Hunter, G., Dickinson, J., Herb, B., and Graham, R., 2005, "Creation of Oxidized Zirconium Orthopaedic Implants," J ASTM International, 2(7), pp. 1-14.

[98] Good, V., Ries, M., Barrack, R. L., Widding, K., Hunter, G., and Heuer, D., 2003, "Reduced Wear with Oxidized Zirconium Femoral Heads," J Bone Joint Surg Am, 85-A Suppl 4, pp. 105-10.

[99] Ries, M. D., Salehi, A., Widding, K., and Hunter, G., 2002, "Polyethylene Wear Performance of Oxidized Zirconium and Cobalt-Chromium Knee Components under Abrasive Conditions," J Bone Joint Surg Am, 84-A Suppl 2, pp. 129-35.

[100] Spector, B. M., Ries, M. D., Bourne, R. B., Sauer, W. S., Long, M., and Hunter, G., 2001, "Wear Performance of Ultra-High Molecular Weight Polyethylene on Oxidized Zirconium Total Knee Femoral Components," J Bone Joint Surg Am, 83-A Suppl 2 Pt 2, pp. 80-6.

[101] Williams, S., Isaac, G., Hatto, P., Stone, M. H., Ingham, E., and Fisher, J., 2004, "Comparative Wear under Different Conditions of Surface-Engineered Metal-on-Metal Bearings for Total Hip Arthroplasty," J Arthroplasty, 19(8), pp. 112-17.

[102] Lappalainen, R., and Santavirta, S. S., 2005, "Potential of Coatings in Total Hip Replacement," Clin Orthop, 430, pp. 72-9.

[103] Santavirta, S., 2003, "Compatibility of the Totally Replaced Hip. Reduction of Wear by Amorphous Diamond Coating," Acta Orthop Scand Suppl, 74(310), pp. 1-19.

[104] Lappalainen, R., Selenius, M., Anttila, A., Konttinen, Y. T., and Santavirta, S. S., 2003, "Reduction of Wear in Total Hip Replacement Prostheses by Amorphous Diamond Coatings," J Biomed. Mater Res B Appl Biomater, 66(1), pp. 410-3.

[105] Affatato, S., Frigo, M., and Toni, A., 2000, "An in Vitro Investigation of Diamond-Like Carbon as a Femoral Head Coating," J Biomed Mater Res, 53(3), pp. 221-6.

[106] Santavirta, S. S., Lappalainen, R., Pekko, P., Anttila, A., and Konttinen, Y. T., 1999, "The Counterface, Surface Smoothness, Tolerances, and Coatings in Total Joint Prostheses," Clin Orthop, 369, pp. 92-102.

[107] Lappalainen, R., Anttila, A., and Heinonen, H., 1998, "Diamond Coated Total Hip Replacements," Clin Orthop, 352, pp. 118-27.

[108] Taylor, J. K., and Pope, B. J., 2000, "The Development of Diamond as a Bearing for Total Hip Arthroplasty," 67th Annual Meeting of the American Academy of Orthopaedic Surgeons, Orlando, Florida.

[109] Pope, B. J., and Taylor, J., 2007, "The Development of Diamond as a Bearing for Arthroplasty Applications," BoneZone, 4(4), pp. 32-35.

[110] Kakarla, D., 2012, "Contact Force Analysis under Femoral Head Micro-Lateralization for Ceramic-on-Ceramic Hip Implants: Finite Element Analysis and Experimental Validation," M.S. thesis, University of Utah, Salt Lake City.

[111] Tibbitts, I. B., 2012, "Dual-Severity Loading Conditions in THA Implants and Their Propensity to Cause Wear-Induced Squeaking in Ceramic-on-Ceramic Bearing Couples," M.S. thesis, University of Utah, Salt Lake City.

[112] 2006, "ASME V&V 10-2006: Guide for Verification and Validation in Computational Solid Mechanics," American Society of Mechanical Engineers, New York.

[113] Sanders, A. P., and Brannon, R. M., 2011, “Determining a Surrogate Contact Pair in a Hertzian Contact Problem,” J Tribol, 133(2), pp. 024502-6.

[114] Sanders, A. P., and Brannon, R. M., 2011, “Assessment of the Applicability of the Hertzian Contact Theory to Edge-Loaded Prosthetic Hip Bearings,” J Biomech, 44(16), pp. 2802-08.

[115] Sanders, A., Tibbitts, I., Kakarla, D., Siskey, S., Ochoa, J., Ong, K., and Brannon, R., 2011, Dynamic Behavior of Materials, Volume 1, Springer New York, “Contact Mechanics of Impacting Slender Rods: Measurement and Analysis,” pp. 229-36.

[116] Sanders, A. P., Dudhiya, P. J., and Brannon, R. M., 2012, “Thin Hard Crest on the Edge of Ceramic Acetabular Liners Accelerates Wear in Edge Loading,” J Arthroplasty, 27(1), pp. 150-52.

[117] Sanders, A., Tibbitts, I., and Brannon, R., 2012, “Concomitant Evolution of Wear and Squeaking in Dual-Severity, Lubricated Wear Testing of Ceramic-on-Ceramic Hip Prostheses,” J Orthop Res, 30(9), pp. 1377-83.

[118] Currier, J. H., Anderson, D. E., and Van Citters, D. W., 2010, “A Proposed Mechanism for Squeaking of Ceramic-on-Ceramic Hips,” Wear, 269(11-12), pp. 782-89.

[119] Hothan, A., Huber, G., Weiss, C., Hoffmann, N., and Morlock, M., 2011, “The Influence of Component Design, Bearing Clearance and Axial Load on the Squeaking Characteristics of Ceramic Hip Articulations,” J Biomech, 44(5), pp. 837-41.

[120] Weiss, C., Hothan, A., Huber, G., Morlock, M. M., and Hoffmann, N. P., 2012, “Friction-Induced Whirl Vibration: Root Cause of Squeaking in Total Hip Arthroplasty,” J Biomech, 45(2), pp. 297-303.

[121] Chevillotte, C., Trousdale, R. T., Chen, Q., Guyen, O., and An, K. N., 2010, “The 2009 Frank Stinchfield Award: “Hip Squeaking”: A Biomechanical Study of Ceramic-on-Ceramic Bearing Surfaces,” Clin Orthop, 468(2), pp. 345-50.

# CHAPTER 2

# DETERMINING A SURROGATE CONTACT PAIR IN A HERTZIAN CONTACT PROBLEM

Reprinted with permission from the American Society of Mechanical Engineers:

Sanders, A.P. and Brannon, R.M., 2011, "Determining a Surrogate Contact Pair in a Hertzian Contact Problem," Journal of Tribology, 133(2), pp. 024502-6.

# Determining a Surrogate Contact Pair in a Hertzian Contact Problem

**Anthony P. Sanders**
Ortho Development Corp.,
12187 S. Business Park Dr.,
Draper, UT 84020
e-mail: tsanders@odev.com

**Rebecca M. Brannon**
Department of Mechanical Engineering,
University of Utah,
50 S. Central Campus Dr.,
2134 Merrill Engineering Bldg.,
Salt Lake City, UT 84112
e-mail: brannon@mech.utah.edu

*Laboratory testing of contact phenomena can be prohibitively expensive if the interacting bodies are geometrically complicated. This work demonstrates means to mitigate such problems by exploiting the established observation that two geometrically dissimilar contact pairs may exhibit the same contact mechanics. Specific formulas are derived that allow a complicated Hertzian contact pair to be replaced with an inexpensively manufactured and more easily fixtured surrogate pair, consisting of a plane and a spheroid, which has the same (to second-order accuracy) contact area and pressure distribution as the original complicated geometry. This observation is elucidated by using direct tensor notation to review a key assertion in Hertzian theory; namely, geometrically complicated contacting surfaces can be described to second-order accuracy as contacting ellipsoids. The surrogate spheroid geometry is found via spectral decomposition of the original pair's combined Hessian tensor. Some numerical examples using free-form surfaces illustrate the theory, and a laboratory test validates the theory under a common scenario of normally compressed convex surfaces. This theory for a Hertzian contact substitution may be useful in simplifying the contact, wear, or impact testing of complicated components or of their constituent materials.* [DOI: 10.1115/1.4003492]

*Keywords: contact mechanics, Hertzian theory, elliptical contact, contact testing, wear testing, substitute contact*

## 1 Introduction

Hertz's theory of elastic contact was originally introduced in 1882 [1]. Johnson [2] noted that the theory met with early appreciation and has "stood the test of time." Notwithstanding myriad pertinent developments in the intervening century, Hertz's geometric propositions are somewhat obfuscated by the common, but cumbersome, use of scalar notation where tensor notation would be clearer [3]. Also, the theory's geometric details lead quite naturally to the concept that the local deformation and stress fields of a complicated contact pair may be replicated to second-order accuracy by a simpler pair having the same relative curvatures. This is a known, but not yet developed or implemented, aspect of the prior work that offers practical benefits of simplifying potentially difficult contact and wear testing projects. Accordingly, the present article has two specific aims:

1. To show that direct tensor notation improves clarity of the geometric propositions in the Hertz contact theory. The theory is underpinned by two propositions that describe the geometry of two smooth contacting surfaces:

- each surface can be described with two principal curvatures lying on mutually orthogonal planes
- the distance between opposing points on the contacting surfaces can be described by a quadratic form, which implies that lines of constant separation are ellipses

Despite seeming to be very limiting, these propositions are, in fact, second-order accurate for arbitrary differentiable surfaces. In this work, a novel tensor description of the geometric problem will be used to clarify and justify these propositions.

2. To prove that an arbitrarily shaped Hertzian contact pair can be substituted with a simpler pair consisting of a spheroid and a flat plane, without altering the original contact area or contact pressure. As shown by upcoming Eqs. (21), (19), and (13), the dimensions of the spheroid can be readily computed using simple functions of the original pair's geometry. Verification is offered by geometric analysis and contact stress analysis of a pair of complicated 3D surfaces. A laboratory validation demonstrates the substitution theory with convex surfaces. This substitution concept clearly has potential to reduce costs of contact and wear testing by using simply manufactured and easily fixtured surrogate geometries.

## 2 Geometry in Hertzian Contact

**2.1 The Assumptions Concerning Geometry.** Assumptions behind Hertzian theory have been amply justified [2,4,5]. Two of the key geometric propositions that describe the contacting surfaces are mathematical statements:

1. Each surface may be described by an equation that includes the surface's two principal curvatures at the contact point
$$z = \tfrac{1}{2}\rho_1 x^2 + \tfrac{1}{2}\rho_2 y^2 \tag{1}$$
2. Closed curves on the two surfaces that are separated by a constant distance $h$ have a projection onto the tangent plane that is an ellipse:
$$h = Ax^2 + By^2 \tag{2}$$

The focus of this section is to elucidate these descriptions via a novel tensor formulation of Hertzian geometry and to illustrate their second-order accuracy in describing the geometry of contact.

**2.2 Description of a Single Surface.** We begin with a description of a general surface in $R^3$ and several vectors associated with a point on that surface (Fig. 1(*a*)). An orthonormal coordinate basis with base vectors $\mathbf{e}_i$ is introduced for convenience. Vector $\mathbf{x}$ describes a variable point on the surface, and vector $\mathbf{p}$ describes the contact point. An analytic function $f$ describes the surface as the set of all points $\mathbf{x}$ satisfying the equation $f(\mathbf{x})=0$. The normal at $\mathbf{p}$ is $\hat{\mathbf{n}}=\nabla f/\|\nabla f\|$. The vector from $\mathbf{p}$ to another point on the surface is $(\mathbf{x}\text{-}\mathbf{p})$, and the vector $\mathbf{r}$ is defined as the part of $(\mathbf{x}\text{-}\mathbf{p})$

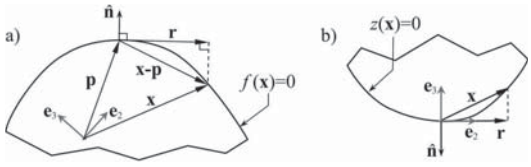


**Fig. 1** (*a*) **Section view through a general surface.** (*b*) **Section view through a surface with the laboratory basis positioned at the point of contact.**

Contributed by the Tribology Division of ASME for publication in the JOURNAL OF TRIBOLOGY. Manuscript received March 21, 2010; final manuscript received January 12, 2011; published online March 17, 2011. Assoc. Editor: Ilya I. Kudish.

  

lying in the plane tangent to the surface at **p**.

For convenience, the basis is positioned at the initial contact point, with one base vector aligned opposite to the surface normal (Fig. 1(*b*)). The other two base vectors span the tangent plane. Disallowing cusps in the surface, the scalar-valued function for the height $z(\mathbf{r})$ of the surface above the tangent plane may be expanded in a Taylor series about the origin as follows:

$$z(\mathbf{r}) = z(\mathbf{0}) + \mathbf{z}'(\mathbf{0}) \bullet \mathbf{r} + \tfrac{1}{2}\mathbf{z}''(\mathbf{0}):\mathbf{rr} + \cdots \tag{3}$$

Here, ":" denotes the tensor inner product operation. The vector- and tensor-valued functions are

$$\mathbf{z}' = \nabla z \text{ and } \mathbf{z}'' = \nabla\nabla z \text{ or: } z_i = \frac{\partial z}{\partial x_i} \text{ and } z_{ij} = \frac{\partial^2 z}{\partial x_i \partial x_j} \quad i,j = 1,2 \tag{4}$$

The higher-order terms are neglected in view of the typical assumption that the contact region is small. The first term in the series is zero because the surface is positioned at the origin; i.e., $z(\mathbf{0}) = 0$. Moreover, the second term is zero because $\mathbf{z}'(\mathbf{0})$ is normal to the surface while **r** is tangent to the surface. Thus, Eq. (3) reduces to one quadratic form $z(\mathbf{r}) \approx \frac{1}{2}\mathbf{z}'':\mathbf{rr}$. Here, $\mathbf{z}''$ is understood to be $\mathbf{z}''(\mathbf{0})$. The matrix and indicial forms are

$$z(\mathbf{r}) \approx \tfrac{1}{2}\{\mathbf{r}\}^{\mathrm{T}}[\mathbf{z}'']\{\mathbf{r}\} \quad \text{and} \quad z(r_1, r_2) = \tfrac{1}{2} r_i (\mathbf{z}'')_{ij} r_j \tag{5}$$

where $\{\mathbf{r}\}$ is the $2 \times 1$ array of in-plane components of **r**, and $[\mathbf{z}'']$ is the $2 \times 2$ component matrix of $\mathbf{z}''$, and repeated indices are implicitly understood to be summed from 1 to 2. Since $[\mathbf{z}'']$ is real and symmetric, there exists an orthonormal principal basis in which it will be diagonal with its eigenvalues as the diagonal components. This matrix $[\mathbf{Z}]$ is related to $[\mathbf{z}'']$ via the basis transformation

$$[\mathbf{z}''] = [\mathbf{Q}][\mathbf{Z}][\mathbf{Q}]^{\mathrm{T}} \tag{6}$$

Here, $[\mathbf{Q}]$ is an orthogonal $2 \times 2$ direction cosine matrix whose columns contain the components of the orthonormalized eigenvectors of $[\mathbf{z}'']$. The matrix $[\mathbf{z}'']$ is also known as the *Hessian* matrix [6]. Its eigenvalues are the principal curvatures ($\eta_1$ and $\eta_2$) of the surface at $\mathbf{r}=\mathbf{0}$. Symmetry of $[\mathbf{z}'']$ ensures that principal curvatures are located on two mutually orthogonal planes.

Thus, Eq. (1) is an approximation based on a Taylor series expansion [3], and the appearance of the principal curvatures results from a spectral analysis of $[\mathbf{z}'']$. The orthogonal orientation between the principal curvature directions stems from the fact that the curvatures are eigenvalues of a symmetric Hessian tensor $\mathbf{z}''$. Substituting Eq. (6) into Eq. (5) yields an equation of the form proposed in Eq. (1) as follows:

$$z = \tfrac{1}{2}\{\mathbf{r}\}^{\mathrm{T}}([\mathbf{Q}][\mathbf{Z}][\mathbf{Q}]^{\mathrm{T}})\{\mathbf{r}\} = \tfrac{1}{2}\{\mathbf{y}\}^{\mathrm{T}}[\mathbf{Z}]\{\mathbf{y}\} \tag{7}$$

where $\{\mathbf{y}\} = [\mathbf{Q}]^{\mathrm{T}}\{\mathbf{r}\}$ so that, because $[\mathbf{Z}]$ is diagonal

$$z = \tfrac{1}{2}(\eta_1 y_1^2 + \eta_2 y_2^2) \tag{8}$$

The $y_i$ are the components of **r** with respect to an orthonormal basis aligned with the eigenvectors of $[\mathbf{z}'']$.

**2.3 Distance Between Surfaces.** Equation (2) pertains to two contacting surfaces (Fig. 2). The principal basis of Surface *K* is the **a**-basis, and that of Surface *P* is the **b**-basis. The following shows in direct tensor notation that points (e.g., *k* and *p*) separated by a fixed distance, $z = z_K + z_P$, form a locus given by a quadratic form analogous to Eq. (2).

Let $\boldsymbol{\kappa}$ represent the Hessian ($\mathbf{z}''$) tensor of Surface *K*, and $\boldsymbol{\rho}$ that of *P*. Thus, Eq. (5) for Surface *K* is $z_K = \frac{1}{2}\mathbf{r} \bullet \boldsymbol{\kappa} \bullet \mathbf{r}$, and for Surface *P* is $z_P = \frac{1}{2}\mathbf{r} \bullet \boldsymbol{\rho} \bullet \mathbf{r}$. Thus, the total separation distance of two points *k* and *p*, $z = z_K + z_P$, is

$$z = \mathbf{r} \bullet \mathbf{A} \bullet \mathbf{r} \quad \text{where} \quad \mathbf{A} = \tfrac{1}{2}(\boldsymbol{\kappa} + \boldsymbol{\rho}) \tag{9}$$

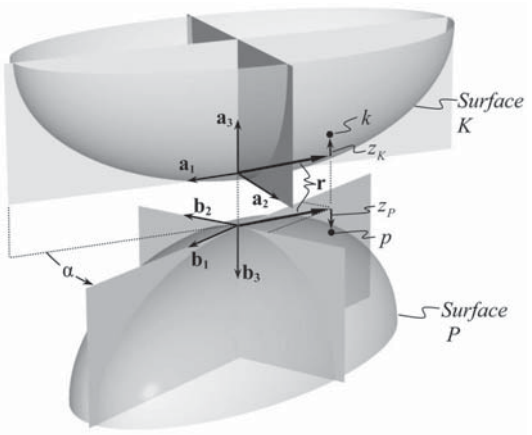


**Fig. 2 Contacting curved surfaces (separated for clarity). Section planes contain principal curvatures. For clarity, points *k* and *p* are shown at an exaggerated distance from the origin.**

Each Hessian tensor is symmetric; therefore, tensor **A** in Eq. (9) is symmetric. The eigenvectors of **A** are not generally aligned with those of $\boldsymbol{\kappa}$ or $\boldsymbol{\rho}$. Since Eq. (9) is in direct notation, it is valid in any basis; with respect to the principal basis of **A**, it may be written in component form as

$$z = \{\mathbf{y}\}^{\mathrm{T}}[\mathbf{D}]\{\mathbf{y}\} = \lambda_1 y_1^2 + \lambda_2 y_2^2 \tag{10}$$

Here, $[\mathbf{D}]$ is a diagonal matrix whose diagonal components, $\lambda_1$ and $\lambda_2$, are the eigenvalues of $[\mathbf{A}]$, and $y_1$ and $y_2$ are the components of **r** with respect to an orthonormal basis aligned with the eigenvectors of $[\mathbf{A}]$. Equation (10) describes an ellipse; ordering the eigenvalues $\lambda_1 < \lambda_2$, and then substituting

$$c = \sqrt{z/\lambda_1} \quad \text{and} \quad d = \sqrt{z/\lambda_2} \tag{11}$$

yields the common form $y_1^2/c^2 + y_2^2/d^2 = 1$, where $c > d$. This describes an ellipse centered at $\mathbf{r}=\mathbf{0}$, with its major semiaxis *c* aligned with the eigenvector associated with $\lambda_1$ and its minor semiaxis *d* aligned with the eigenvector of $\lambda_2$. We term a locus of points satisfying Eq. (10) for a particular *z* as a *tangent ellipse*. For all such points **r**, there are corresponding points $z_K(\mathbf{r})$ and $z_P(\mathbf{r})$ on *K* and *P*. We call these loci *separation curves* (Fig. 3). Viewed along the normal axis, the separation curves are coincident with the tangent ellipse.

**2.4 Spectral Analysis.** Spectral analysis of $[\mathbf{A}]$ is used to find its eigenvalues. Selecting a basis that coincides with the principal basis of Surface *K* (the **a**-basis), the component form of $[\mathbf{A}]$ is

$$[\mathbf{A}] = \frac{1}{2}\left(\begin{bmatrix} \kappa_1 & 0 \\ 0 & \kappa_2 \end{bmatrix} + \begin{bmatrix} \cos\alpha & \sin\alpha \\ \sin\alpha & -\cos\alpha \end{bmatrix}\begin{bmatrix} \rho_1 & 0 \\ 0 & \rho_2 \end{bmatrix} \begin{bmatrix} \cos\alpha & \sin\alpha \\ \sin\alpha & -\cos\alpha \end{bmatrix}\right) \tag{12}$$

Here, the principal curvatures of $\boldsymbol{\kappa}$ and $\boldsymbol{\rho}$ are ordered such that $|\kappa_1| < |\kappa_2|$ and $|\rho_1| < |\rho_2|$. The orientation angle $\alpha$ shown in Fig. 2 is the angle between principal directions of $\boldsymbol{\kappa}$ and $\boldsymbol{\rho}$. The eigenvalues of $[\mathbf{A}]$ are

$$\lambda_1 = \tfrac{1}{4}(\Sigma - \Delta) \quad \text{and} \quad \lambda_2 = \tfrac{1}{4}(\Sigma + \Delta) \quad \text{where}$$

$$\Sigma = \kappa_1 + \kappa_2 + \rho_1 + \rho_2 = 2\ \mathrm{tr}(\mathbf{A})$$

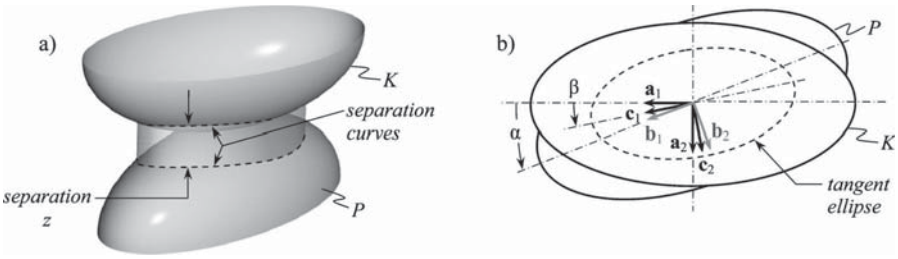


**Fig. 3** (*a*) **Separation curves, joined by a transparent surface for visual reference.** (*b*) **In plan view, separation curves overlie the tangent ellipse; also, a c-basis is aligned with the principal axes of the tangent ellipse.**

$$\Delta = [(\kappa_1 - \kappa_2)^2 + (\rho_1 - \rho_2)^2 + 2(\kappa_1 - \kappa_2)(\rho_1 - \rho_2)\cos(2\alpha)]^{1/2} \tag{13}$$

In summary, Eq. (2) is derivable using a symmetric tensor **A** composed of the principal curvatures of the two surfaces. Spectral analysis of this tensor reveals the key dimensions of the tangent ellipse: its major and minor semiaxis lengths. This derivation illustrates how the separation distance and the tangent ellipse can be determined from the surface configuration using direct tensor notation, which is clearer than scalar analysis because of the intrinsic invariance of tensors to basis change.

**2.5 Verification.** Numerical simulations were performed to examine the accuracy of the derived formulas. The simulation objects were arbitrarily curved surfaces created using computer-aided design (CAD) software. First, a curved surface was created, as in Fig. 4(*a*). Then, portions of the surface were extracted and transformed into an initial contact configuration, as in Fig. 4(*b*). Both surfaces were measured in the software to determine the normal vectors, principal curvatures, and principal curvature orientations (Table 1). The laboratory basis was positioned at the contact point and aligned with one surface's normal and principal curvatures.

Next, one surface was translated a small distance $\delta$ into the other along the normal. The intersection curve between the surfaces was equivalent to a separation curve for the distance $\delta$. This 3D curve was projected onto the tangent plane at the origin, forming a 2D curve that was termed a *quasi-ellipse* because corresponding semiaxes were unequal in length. A sequence of such translations (Sim 1) was compiled for a range of $\delta$. For each, the lengths of both of the quasi-ellipse's major semiaxes were recorded. In a second simulation (Sim 2), one member was concave.

For comparison with each constructed quasi-ellipse, the corresponding tangent ellipse was determined. Its major semiaxis length was computed using Eqs. (13) and (11) along with the data in Table 1 and the values of $\delta$ as data for $z$ in Eq. (11). Figure 5 illustrates the second-order accuracy of the computed dimensions; it shows that the difference between the quasi-ellipse (generated from arbitrary surfaces) and the tangent ellipse (from the theory) tends toward zero as the separation distance decreases.

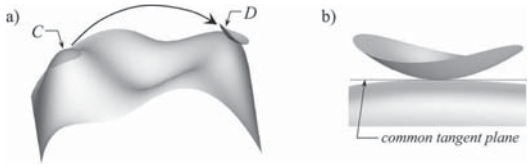


**Fig. 4** (*a*) **Free-form virtual surface; region at *C* extracted and transformed to contact the original surface at *D*.** (*b*) **Surfaces at *D* (viewed along tangent plane) initially touch at a point.**

## 3 Systematic Determination of a Surrogate Contact Pair

We seek to replace an original, presumably complicated, Hertzian contact pair with a surrogate pair that will exhibit the same Hertzian contact mechanics as the original pair to second-order accuracy. The replacing pair should meet two design conditions to fulfill this purpose. Condition 1 is that prior to loading, the replacing pair should exhibit the same separation curves as the original pair. Thus, from Eq. (10), the replacing pair should have the same constants $\lambda_1$ and $\lambda_2$ as the original pair; hence, these are combined into an equality expressing the following condition:

$$\lambda_{1R} + \lambda_{2R} = \lambda_{1O} + \lambda_{2O} \tag{14}$$

Here, subscripts $R$ and $O$ denote the replacing pair and the original pair, respectively.

Condition 2 is that upon loading, the replacing pair must exhibit the same contact area to second-order accuracy, given identical normal force, materials, etc. The tangent ellipse due to a constant separation distance $z$ in Eq. (10) is not identical to the ellipse that borders the loaded contact area (termed the *contact ellipse*). Instead, the two ellipses are related by the following equation, written in terms of the original pair [2]:

$$\frac{\lambda_{2O}}{\lambda_{1O}} = \frac{(a/b)^2\mathbf{E}(e) - \mathbf{K}(e)}{\mathbf{K}(e) - \mathbf{E}(e)} \tag{15}$$

Here, $a$ and $b$ are the major and minor semiaxes of the original

**Table 1 Principal curvatures and orientation for each simulation**

| | Surface 1 ($mm^{-1}$) | | Surface 2 ($mm^{-1}$) | | |
|---|---|---|---|---|---|
| Sim | $\kappa_1$ | $\kappa_2$ | $\rho_1$ | $\rho_2$ | $\alpha$ (rad) |
| 1 | 0.1821 | 0.2849 | 0.0454 | 0.3076 | $\pi/6$ |
| 2 | −0.0298 | −0.0995 | 0.1014 | 0.2932 | $\pi/9$ |

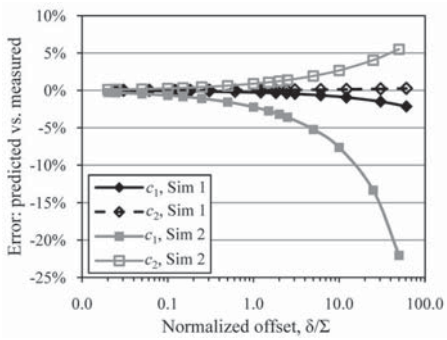


**Fig. 5 Major semiaxis lengths from Sims 1 and 2, compared with predictions. There were two values for each semiaxis (i.e., $c_1$ and $c_2$) since the quasi-ellipses' complementary semiaxes were not identical.**

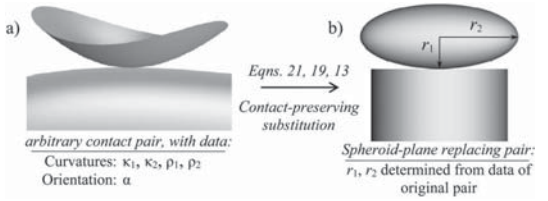


**Fig. 6 Hertzian substitution concept: An arbitrary contact pair (*a*), with given principal curvatures and orientation, is substituted with a simpler contact pair (*b*) consisting of a spheroid and a plane**

pair's contact ellipse, $e=\sqrt{1-(b^2/a^2)}$ is the *eccentricity*, and **K** and **E** are the complete elliptic integrals of the first and second kinds, respectively. Condition 2 means that the replacing pair must also satisfy Eq. (15), from which a second equality is deduced as follows:

$$\lambda_{2R}/\lambda_{1R}=\lambda_{2O}/\lambda_{1O} \tag{16}$$

In the replacing pair, the second body is chosen to be a plane; thus, $\rho_{1R}=\rho_{2R}=0$. Then, using Eq. (16), Eq. (14) reduces to

$$\kappa_{1R}+\kappa_{2R}=\Sigma_O \tag{17}$$

and Eq. (16) reduces to

$$\frac{\kappa_{2R}}{\kappa_{1R}}=\frac{\Sigma_O+\Delta_O}{\Sigma_O-\Delta_O} \tag{18}$$

Solving these simultaneously yields the following:

$$\kappa_{1R}=\tfrac{1}{2}(\Sigma_O-\Delta_O),\quad \kappa_{2R}=\tfrac{1}{2}(\Sigma_O+\Delta_O) \tag{19}$$

where $\kappa_{1R}$ and $\kappa_{2R}$ are the principal curvatures of the first body in the replacing pair. The quantities $\Sigma_O$ and $\Delta_O$ are simple functions of the original pair's configuration, per Eq. (13). Equation (19) shows that the principal curvatures of the first body in the replacing pair can be expressed entirely in terms of known geometric properties of the original surfaces. By using a lathe, a prolate spheroid can be inexpensively produced to provide the two required curvatures. The spheroid is described by the equation

$$\frac{x^2}{r_1^2}+\frac{y^2}{r_2^2}+\frac{z^2}{r_1^2}=1 \quad \text{where} \quad r_2>r_1 \tag{20}$$

To form the replacing pair, this spheroid would be placed in contact with its planar counterpart, with its $z$ axis normal to the plane. For this configuration, the spheroid's defining radii can be computed as

$$r_1=1/\kappa_{2R},\quad r_2=\sqrt{1/(\kappa_{1R}\kappa_{2R})} \tag{21}$$

The result in Eq. (21) provides a means to substitute an arbitrary contact pair with a surrogate pair, consisting of a spheroid and a plane, which will provide the same contact area and pressure to second-order accuracy. This concept of Hertzian substitution is illustrated in Fig. 6.

It is alternatively possible to determine the dimensions of a surrogate pair consisting of a cylinder and a spheroid. Choosing a value for the radius of the replacing cylinder $r_2$ yields the cylinder principal curvatures $\rho_{1R}=0$ and $\rho_{2R}=1/r_2$. Then, the curvatures of the replacing spheroid can be computed as

$$\kappa_{1R}=\tfrac{1}{2}(\Sigma_O-\Delta_O),\quad \kappa_{2R}=\tfrac{1}{2}(\Sigma_O+\Delta_O-2\rho_{2R}) \tag{22}$$

**3.1 Verification.** To verify these analytical results, the free-form virtual contact pair of Fig. 6(*a*) was taken as an original pair, and it was compared with its replacing pair of Fig. 6(*b*). In the following simulations, the surfaces were built, manipulated, and measured in the CAD software.

*Sim A.* Comparison of tangent ellipse dimensions to demonstrate the second-order equivalence of the replacing pair as a surrogate for the original pair.

*Sim B.* Comparison of contact ellipse dimensions to substantiate use of the replacing pair as a surrogate for the original pair in testing scenarios.

The geometry of the replacing pair was computed from the original pair's data using Eqs. (21), (19), and (13). The data and results are given in Table 2.

In Sim A, the dimensions of the tangent ellipses were computed using Eqs. (13) and (11) with the data in Table 2. Results were computed across a range of $z$, and at every value, the difference between the semiaxis lengths was zero (Fig. 7(*a*)). This parity between the tangent ellipses demonstrates that the original and replacing pairs are equivalent contact pairs to second-order accuracy.

In Sim B, the virtual surfaces were assumed to be solid bodies, and both contact pairs were examined by Hertzian contact analysis for normal loading. The first body in each pair was assigned an elastic modulus of 200 GPa and Poisson's ratio of 0.3, and the second body was assigned values of 150 GPa and 0.3. The dimensions of the contact ellipse and the peak contact pressure were computed for a range of loads, using formulas described elsewhere [2]. The results, given in Fig. 7(*b*), were identical for the two pairs, which further demonstrates their equivalence as Hertzian contact pairs.

**3.2 Validation.** Experimental validation was performed by comparing the contact ellipses of several different original pairs with those of their replacing pairs. Results from one such trial are presented here.

A novel "fingerprinting" technique was developed for recording a contact patch. Specifically, one surface was dabbed with grease, and the grease was wiped repeatedly (e.g., 20 times) with clean paper towels to leave a scant film. When the two surfaces were

**Table 2 Geometry of original and replacing pairs for Sims A and B (curvatures in $mm^{-1}$ and radii in mm)**

| Original pair, with $\alpha=\pi/6$ | | | |
|---|---|---|---|
| $\kappa_1$ | $\kappa_2$ | $\rho_1$ | $\rho_2$ |
| 0.1820980 | 0.2848800 | 0.0453731 | 0.3076450 |
| Replacing pair | | | |
| $\kappa_{1R}$ | $\kappa_{2R}$ | $r_1$ | $r_2$ |
| 0.246974 | 0.573022 | 1.745133 | 2.658207 |

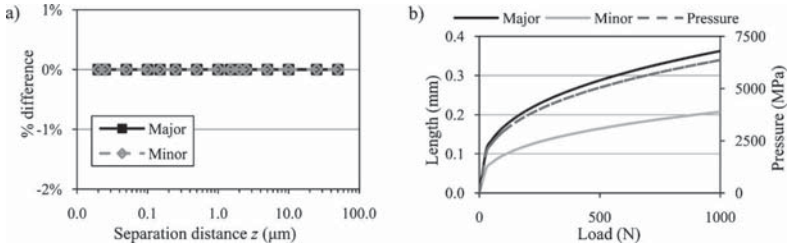


**Fig. 7 Simulation results. (*a*) Sim A tangent ellipses: results show zero difference. (*b*) Sim B: Contact analysis: results for semiaxis lengths and pressure were identical for the pairs.**

loaded, a thin layer of the grease was transferred onto the originally clean surface at the contact patch. After the test, this surface was sprinkled with photocopier toner powder, and then the powder was blown off with dry compressed air. This left black powder adhered to the transferred grease, which provided a record of the contact patch with better defined boundaries than could be obtained with commercially available methods for marking contact patches. The contact patch was then measured and photographed using an optical coordinate measuring machine (Nexiv, Nikon, Japan).

In one validation test, the original pair consisted of two $\varnothing 37.5 \times 76$ mm cylinders made of extruded polyetherimide plastic. The cylinders were arranged one on top of the other, with their axes mutually angled at 45 deg. The replacing pair consisted of a spheroid mated with a flat disk, with the spheroid's dimensions computed using Eq. (21). All surfaces were polished to a surface texture of $\sim 0.2$ $\mu$m roughness average ($R_a$). Each pair was compressed under loads from 200 N to 600 N. The major and minor axes of the contact patches were measured, and the results are compared in Fig. 8.

## 4 Discussion

The key geometric propositions in Hertz's theory, which are sometimes obfuscated through the use of scalar notation, have been presented here using a concise and relatively intuitive tensor notation that groups related properties that would otherwise appear as separate variables. For example, the Hessian tensor in Eq. (4) is represented compactly by $\mathbf{z}''$, and trigonometric terms of the orientation angle $\alpha$ are not introduced until the combined Hessian tensor $\mathbf{A}$ is expressed in component form in Eq. (12). The use of a truncated, multivariate Taylor series expansion to represent the distance between the contacting surfaces rigorously showed the Hertzian approximation of the contacting surfaces to be second-order accurate.

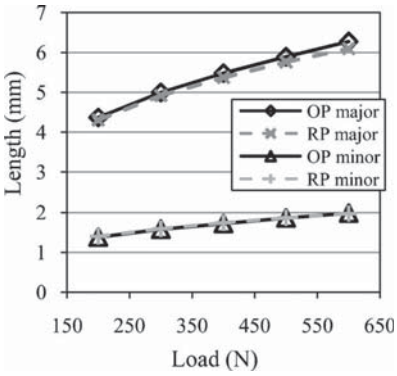


**Fig. 8 Results of one validation test: comparison of contact patch major and minor axes. Legend: "OP" is the original pair, and "RP" is its replacing pair. Results for minor axes overlie one another.**

Two simulations have been here described to potentially set a standard for verification of codes that employ the Hertzian geometric propositions. Differences between the quasi-ellipses and the tangent ellipses are shown to arise because the separation distance, as represented by the tangent ellipse equation, is second-order accurate, not exact. By reducing the normal offset ($\delta$) of one surface into the other, the Hertzian formulation was shown to become increasingly accurate in the sense that the quasi-ellipse approached an ellipse. This exercise nicely illustrates the small-displacement limitation of Hertzian theory.

The second part of this article developed simple equations to compute the dimensions of a spheroid-plane contact pair that can substitute for a complicated contact pair and exhibit the same contact behavior, which is appealing for reducing costs in wear testing. Sims A and B demonstrated that the original and replacing pairs have separation distances, contact ellipses, and contact pressures that are equal to second-order accuracy. A simple laboratory experiment validated the substitution theory in a convex contact pair. Johnson showed [2] that the coefficients $A$ and $B$ describing the separation of contacting surfaces (Eq. (2)) determine in part the contact ellipse. The present article has thoroughly demonstrated a consequence of that observation via a validated analysis giving explicit equations for a simple surrogate contact pair.

## 5 Summary and Conclusions

The established notion that two geometrically dissimilar contact pairs may exhibit the same contact mechanics can be exploited to advantage. An original, complicated Hertzian contact pair may be substituted by a simpler, surrogate contact pair that will replicate the original pair's contact mechanics to second-order accuracy.

The surrogate contact pair can take the form of a spheroid-plane pair or of a spheroid-cylinder pair. The geometric simplicity of these replacing pairs may make them useful surrogates for expensive or complicated components in contact testing, such as ranking of materials for their wear resistance.

The geometric propositions of Hertzian contact theory are elucidated by using direct tensor notation. This approach clarifies the simplifying representation of an arbitrary surface by its two principal curvatures. Further, the approach shows that the Hertzian formulation of surface separation as a quadratic form results from a second-order Taylor series approximation. The coefficients in the quadratic form are the eigenvalues of the combined Hessian tensors of the two contacting surfaces.

## Acknowledgment

This work was supported by Award No. R21AR056374 from the National Institute of Arthritis and Musculoskeletal and Skin Diseases (NIAMS).

## Nomenclature

### Vectors, Tensors, and Matrices

Vector and tensor quantities are in bold; in matrix form they are enclosed in brackets or braces. For example, a tensor $\mathbf{T}$ in matrix form is denoted as $[\mathbf{T}]$. Likewise, a vector $\mathbf{v}$ in array form is denoted as $\{\mathbf{v}\}$.

- $\mathbf{A}$ = Hessian tensors combined under a common laboratory basis
- $[\mathbf{D}]$ = diagonalized component matrix of $\mathbf{A}$
- $[\mathbf{Q}]$ = rotation matrix formed from components of eigenvectors of $\mathbf{z}''$
- $[\mathbf{Z}]$ = diagonal matrix of principal curvatures of a surface
- $\mathbf{a}_i, \mathbf{b}_i$ = $i$th base vector of a basis aligned with principal curvatures of Surfaces $K$ and $P$
- $\mathbf{c}_i$ = $i$th base vector of a basis aligned with the principal axes of the tangent ellipse
- $\mathbf{e}_i$ = $i$th base vector of a fixed orthonormal laboratory reference basis
- $\hat{\mathbf{n}}$ = unit vector normal to a surface
- $\mathbf{p}$ = the initial point of contact on a surface
- $\mathbf{r}$ = the part of ($\mathbf{x}$-$\mathbf{p}$) that lies in the mutual tangent plane
- $\mathbf{x}$ = vector to a point on a surface
- $\mathbf{y}$ = coordinate vector of basis aligned with surface principal curvatures
- $\mathbf{z}'$ = gradient of $z$
- $\mathbf{z}''$ = double gradient of $z$; tensor of surface curvatures
- $\boldsymbol{\kappa}, \boldsymbol{\rho}$ = Hessian tensors of Surfaces $K$ and $P$
- $\mathbf{0}$ = the zero vector

### Scalars

- $A$, $B$ = coefficients in ellipse equation
- $K$, $P$ = labels for two contacting surfaces
- $R^3$ = real, three-dimensional space
- $a$, $b$ = major and minor semiaxes of the contact ellipse
- $c$, $d$ = major and minor semiaxes of the tangent ellipse
- $e$ = eccentricity of an ellipse
- $h$ = distance between opposing points on contacting surfaces
- $k$, $p$ = opposing points on contacting surfaces
- $r_1$, $r_2$ = principal radii of a prolate spheroid
- $z$ = distance of a surface point from the tangent plane; alternately, distance between opposing points on two surfaces
- $\alpha$ = angle between planes of minimum absolute principal curvature, measured relative to the surface initially expressed in the $\mathbf{a}$-basis
- $\beta$ = orientation angle of the tangent ellipse relative to the laboratory basis
- $\Delta$ = function of principal curvatures and their relative orientation
- $\Sigma$ = sum of principal curvatures of both surfaces
- $\delta$ = a displacement along the common normal axis
- $\kappa_1$, $\kappa_2$ = principal curvatures at the contact point on the surface aligned with the $\mathbf{a}$-basis
- $\lambda_1$, $\lambda_2$ = eigenvalues of $[\mathbf{A}]$
- $\eta_1$, $\eta_2$ = principal curvatures at the contact point on a lone surface
- $\rho_1$, $\rho_2$ = principal curvatures at the contact point on the surface aligned with the $\mathbf{b}$-basis

### Special Functions

- $\mathbf{K}$, $\mathbf{E}$ = complete elliptic integrals of first and second kinds of modulus $e$

### Subscripts

- $K$, $P$ = surfaces $K$ and $P$
- $O$, $R$ = original pair and replacing pair

## References


[1] Hertz, H., 1882, "Uber Die Beruhrung Fester Elastischer Korper (on the Contact of Elastic Solids)," J. Reine Angew. Math., **92**, pp. 156–171.

[2] Johnson, K. L., 1985, *Contact Mechanics*, Cambridge University Press, Cambridge.

[3] Lur'e, A. I., 1964, *Three-Dimensional Problems in the Theory of Elasticity*, Wiley, New York.

[4] Antoine, J. F., Visa, C., Sauvey, C., and Abba, G., 2006, "Approximate Analytical Model for Hertzian Elliptical Contact Problems," ASME J. Tribol., **128**(3), pp. 660–664.

[5] Timoshenko, S. P., and Goodier, J. N., 1970, *Theory of Elasticity*, McGraw-Hill, New York.

[6] Frankel, T., 1997, *The Geometry of Physics: An Introduction*, Cambridge University Press, Cambridge.

# CHAPTER 3

# ASSESSMENT OF THE APPLICABILITY OF THE HERTZIAN CONTACT THEORY TO EDGE-LOADED PROSTHETIC HIP BEARINGS

Reprinted with permission from Elsevier, Ltd.:

Sanders, A.P. and Brannon, R.M., 2011, "Assessment of the Applicability of the Hertzian Contact Theory to Edge-Loaded Prosthetic Hip Bearings," Journal of Biomechanics, 44(16), pp. 2802-2808.

Journal of Biomechanics 44 (2011) 2802–2808

Contents lists available at SciVerse ScienceDirect

Journal of Biomechanics

journal homepage: www.elsevier.com/locate/jbiomech
www.JBiomech.com

# Assessment of the applicability of the Hertzian contact theory to edge-loaded prosthetic hip bearings

Anthony P. Sanders [a,b,*], Rebecca M. Brannon [a]

[a] Department of Mechanical Engineering, University of Utah, Salt Lake City, UT 84112, USA
[b] Ortho Development Corporation, 12187 Business Park Dr., Draper, UT 84020, USA

ARTICLE INFO

*Article history:*
Accepted 11 August 2011

*Keywords:*
Prosthetic hip bearings
Hertzian contact
Edge loading
Microseparation
Ceramic-on-ceramic

ABSTRACT

The components of prosthetic hip bearings may experience *in-vivo* subluxation and edge loading on the acetabular socket as a result of joint laxity, causing abnormally high, damaging contact stresses. In this research, edge-loaded contact of prosthetic hips is examined analytically and experimentally in the most commonly used categories of material pairs. In edge-loaded ceramic-on-ceramic hips, the Hertzian contact theory yields accurate (conservatively, $<10\%$ error) predictions of the contact dimensions. Moreover, the Hertzian theory successfully captures slope and curvature trends in the dependence of contact patch geometry on the applied load. In an edge-loaded ceramic-on-metal pair, a similar degree of accuracy is observed in the contact patch length; however, the contact width is less accurately predicted due to the onset of subsurface plasticity, which is predicted for loads $>400$ N. The Hertzian contact theory is shown to be ill-suited to edge-loaded ceramic-on-polyethylene pairs due to polyethylene's nonlinear material behavior. This work elucidates the methods and the accuracy of applying classical contact theory to edge-loaded hip bearings. The results help to define the applicability of the Hertzian theory to the design of new components and materials to better resist severe edge loading contact stresses.



## 1. Introduction

The femoral head and acetabular liner of a prosthetic hip joint may not always function as the ideal ball-and-socket joint they are designed to be, which may be a root cause for clinically observed wear modes. Hip replacement surgery may alter the structural dimensions and the tissue constraints of a hip joint such that the ball and socket are held together more loosely than planned for in design. Thus, when examining the potential wear modes of prosthetic hips, it is important to consider that the joint has the potential to be damaged from adverse behaviors such as disassociation and eccentric contact.

Previous investigations have described various abnormal behaviors in prosthetic hip joints. Dislocation, with the ball (or *head*) fully exiting the socket, has been widely reported and is the extreme example (Lewinnek et al., 1978). Fluoroscopic studies have revealed smaller ball-socket separations (subluxation) during various hip motions (Lombardi et al., 2000; Dennis et al., 2001; Komistek et al., 2002). Such subluxation has been called *microseparation* (Nevelos et al., 2000) and *micro-lateralization* (Sariali et al., 2010). Implant malalignment and small femoral heads may contribute to femoral neck impingement on the liner's rim (Nadzadi et al., 2002; Crowninshield et al., 2004). Impingement may lever the head out of the socket, causing subluxation where the head bears upon the socket's edge (*edge loading*) (Scifert et al., 2001; Kluess et al., 2007). A relatively vertical cup orientation may cause edge loading (Mellon et al., 2010), and a recent clinical study found 34% of 1884 acetabular cups to be abducted above the ideal 45° maximum (Callanan et al., 2010). Thus, systematic laboratory investigations are needed to quantify the wear characteristics or other consequences of these ways that a prosthetic hip might deviate from ideal behavior.

Dislocation can severely scratch the femoral head (Bourne et al., 2005). Microseparation can cause ceramic component stripe wear (Walter et al., 2004; Yamamoto et al., 2005), and in laboratory tests, stripe wear has contributed to squeaking in ceramic hips (Taylor et al., 2007). Finite element analyses (FEA) of edge loading contact stresses from microseparation (Mak et al., 2002) and impingement (Kluess et al., 2007) have revealed markedly elevated contact stresses. Hip simulator wear tests imparting microseparation and edge loading have elicited clinically relevant stripe wear on ceramic prostheses (Nevelos et al., 2000; Manaka et al., 2004). Each of these effects is a potential failure mode in the sense that the bearings accrue potentially harmful damage.

* Corresponding author at: Ortho Development Corp., 12187 Business Park Dr., Draper, UT 84020, USA. Tel.: +1 801 619 3436; fax: +1 801 619 8936.
*E-mail address:* ap.sanders@utah.edu (A.P. Sanders).

0021-9290/$ - see front matter © 2011 Elsevier Ltd. All rights reserved.
doi:10.1016/j.jbiomech.2011.08.007

**Nomenclature**

| | |
|---|---|
| $E$, $E^*$ | Young's modulus, apparent elastic modulus |
| $\mathbf{K}(e)$, $\mathbf{E}(e)$ | complete elliptic integrals of first, second kind, for modulus $e$ |
| $H$, $K$ | mean, Gaussian curvatures |
| ID, OD | inner diameter, outer diameter |
| $Q$ | normal contact force |
| $P_{max}$ | maximum contact pressure |
| $\overline{P}$ | mean contact pressure |
| $R$, $r$ | major, minor radii of a torus |
| $a$, $b$ | major, minor semi-axes of a contact patch |
| $e$ | ellipse eccentricity |
| $e'$ | complementary eccentricity |
| $\alpha$ | angle between planes of minimum absolute principal curvature |
| $\theta$ | orientation angle between a contacting torus and nested sphere |
| $\delta$ | polar separation between femoral head and acetabular liner |
| $\Sigma$, $\Delta$ | functions of the principal curvatures and orientation of contacting surfaces |
| $\kappa_1$, $\kappa_2$ | principal curvatures at the contact point of a first body in a contact couple |
| $\rho_1$, $\rho_2$ | principal curvatures at the contact point of a second body in a contact couple |
| $\nu$ | Poisson's ratio |
| $\phi$ | angle about a minor diameter in parametric equations of a torus |

In ideal concentric loading, the ball and socket are in conforming contact, meaning that their contacting surface radii are closely matched (e.g. $<100\,\mu m$ difference); thus, loads produce large contact areas and low contact stresses. On the contrary, adverse loading (e.g. edge loading) induces high contact stress because the ball and socket come into non-conforming contact, meaning that the contacting surfaces have radii that differ greatly. Under such conditions, loads generate smaller contact areas and higher contact stresses.

Although the Hertzian contact theory has been applied in the case of concentric ceramic-on-ceramic hip contact (Mak and Jin, 2002), its merits and shortcomings have not been assessed in abnormal states and multiple material couples. For analyses of adverse loading, the Hertzian theory may be useful and applicable provided that the following key assumptions of the theory are approximately satisfied: (1) the materials are homogeneous, linear elastic, and isotropic; (2) the surfaces are perfectly smooth and frictionless; (3) the surfaces are non-conforming; and (4) the contact dimensions are much smaller than the surface radii at the contact point (Hertz, 1882; Johnson, 1985). Considering these in the case of edge-loaded ceramic and metal hip prostheses, the following three preliminary observations are made:

- Items 1 and 2 are as closely approximated as they are in the case of concentric contact.
- For Item 3, the surfaces are less conforming than in the case of concentric contact.
- Thus, Item 4 is more likely to be valid than in the case of concentric contact.

Based on these observations, this study examines the hypothesis that the contact dimensions of edge-loaded ceramic and metal hip bearings can be accurately estimated using the Hertzian theory. For contrast, the study also examines the hypothesis that a plastic bearing material with nonlinear constitutive behavior will not be accurately modeled by the theory.

## 2. Materials and Methods

### 2.1. Hertzian contact analysis

Contact between a femoral head and a liner's radiused edge was modeled as a sphere-torus contact (Fig. 1). Predictions of the contact dimensions were computed using the Hertzian contact theory. For a contact point on the torus surface, the principal curvatures are given by (Irons, 2005)

$$\kappa_1 = H - \sqrt{H^2 - K}, \quad \kappa_2 = H + \sqrt{H^2 - K} \tag{1}$$

Here, $K$ is the Gaussian curvature and $H$ is the mean curvature, which are

$$K = \frac{\cos\phi}{r(R + r\cos\phi)}, \quad H = \frac{R + 2r\cos\phi}{2r(R + r\cos\phi)} \tag{2}$$

Here, $R$ and $r$ are the torus' major and minor radii, respectively, and $\phi$ is the angle about the torus' minor diameter. Given the liner inclination $\theta$ in Fig. 1, $\phi$ was related to $\theta$ as: $\phi = \pi - \theta$. The dimensions of the contact ellipse relate to the contacting surfaces' configuration as (Nikas, 2002)

$$\frac{(1-e^2)^{-1}\mathbf{E}(e) - \mathbf{K}(e)}{\mathbf{K}(e) - \mathbf{E}(e)} = \frac{\Sigma + \Delta}{\Sigma - \Delta} \tag{3}$$

where (Hertz, 1882; Harris, 1991)

$$\Sigma = \kappa_1 + \kappa_2 + \rho_1 + \rho_2 \quad \text{and}$$

$$\Delta = [(\kappa_1 - \kappa_2)^2 + (\rho_1 - \rho_2)^2 + 2(\kappa_1 - \kappa_2)(\rho_1 - \rho_2)\cos(2\alpha)]^{1/2} \tag{4}$$

Here, $\rho_1$ ($=\rho_2$) was the curvature of the sphere, and $\alpha = 0$ since one surface was spherical. Further, $e = \sqrt{(1 - b^2/a^2)}$, where $a$ is the contact ellipse's major semi-axis and $b$ its minor semi-axis. $\mathbf{K}(e)$ and $\mathbf{E}(e)$ are the complete elliptic integrals of the first and second kind. Eq. (3) was solved numerically for $e$.

Starting from Hertz's integral formulas (Hertz, 1882), we derived formulas for the contact ellipse dimensions:

$$a = \left\{\frac{6Q[\mathbf{K}(e) - \mathbf{E}(e)]}{\pi e^2 E^*(\Sigma - \Delta)}\right\}^{1/3}, \quad b = \left\{\frac{6Qe'\left[\mathbf{E}(e) - (e')^2\mathbf{K}(e)\right]}{\pi e^2 E^*(\Sigma + \Delta)}\right\}^{1/3} \tag{5}$$

where $e' = \sqrt{(1 - e^2)}$ (Erdelyi, 1953). The contacting bodies' Young's moduli ($E_1$, $E_2$) and Poisson's ratios ($\nu_1$, $\nu_2$) appear within $E^*$: $1/E^* = (1 - \nu_1^2)/E_1 + (1 - \nu_2^2)/E_2$. The maximum contact pressure is $P_{max} = 3Q/2\pi ab$, and the mean pressure is $\overline{P} = Q/\pi ab$ (Johnson, 1985).

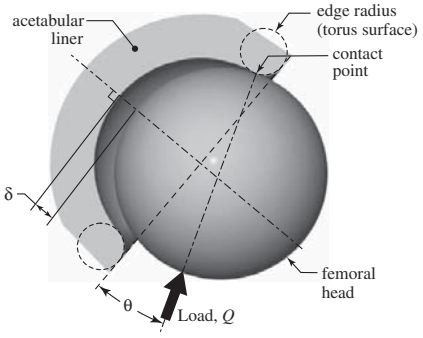


**Fig. 1.** Model of edge-loaded contact, with socket shown in cross section. View gives an anterior-posterior perspective with cup oriented at 50° abduction. In the experiments, the entire assembly was posed with the load vector $Q$ vertical and downward; otherwise, the relative positions were as shown.

### 2.2. Test specimens

To validate this study's hypotheses, three different material pairs were tested: ceramic-on-ceramic (CoC), ceramic-on-metal (CoM), and ceramic-on-plastic (CoP). The ceramic components were $Al_2O_3$ products (Biolox Forte, Ceramtec, Germany). Two CoC pairs, nominally ∅28 mm and ∅36 mm, were examined. The CoCr (ASTM F 1537) liner was a custom-made facsimile; to reduce cost, its concave ID was simplified from a sphere to a cylinder, though without affecting the desired form of the edge radius. This liner had a nominal 36 mm ID and a 4.0 mm edge radius polished to 0.05 μm $R_a$. There were also two plastic liners, nominally ∅28 and ∅36 mm. They were custom-made from crosslinked ultra-high molecular weight polyethylene (XLPE), and their 2.54 mm edge radii were polished to 0.2 μm $R_a$. All components are pictured in the on-line material. The relevant material properties are given in Table 1.

In the ceramic liners, the edge radius was observed to consist of multiple segments. The edge was measured by three means: 1) a touch-probe coordinate-measuring-machine (CMM) with resolution $<5$ μm (Contura, Zeiss, Germany), 2) an arc-encoder stylus with resolution $<0.5$ μm (Contracer, Mitutoyo, Japan), and 3) a laser sensor with resolution $<0.1$ μm (Nexiv, Nikon, Japan). The measurements revealed that the edge's profile was best represented as a series of arc segments (Fig. 2, dimensions in Table 2). Each segment, being a surface of revolution, was regarded as a partial torus surface. Both ceramic liners exhibited a distinct crest where the edge met the spherical surface; otherwise, the junctions between surface segments were tangent. In the CoCr and XLPE liners, the edge radii were closely controlled during manufacture to yield single arc segments. These specimens' key dimensions are in Table 3.

### 2.3. Contact tests

The liner was secured via a Morse taper with a titanium acetabular shell. The shell was securely assembled within a hemispherical cavity in a 481 kg/m$^3$ polyurethane (ASTM F-1839) test block. As an exception, the CoCr liner was clamped directly in the test fixtures.

The tests created quasi-static contact between the femoral head and specified points on each liner's edge. Fig. 3 shows the typical setup; the on-line material provides additional photos. The head was attached to the uniaxial test frame's actuator. A sine plate was attached to the test frame's load cell, and the plate oriented the liner (angle $\theta$, Fig. 1) such that the specified contact point had a vertical normal vector. The liner assembly was placed on the sine plate underneath the head. To align the head's pole to the nadir of the liner's edge, we used a repetitive process of making a contact mark between the head and edge, followed by shimming the test block to adjust the alignment. Alignment accurate to 20 μm was confirmed using an optical CMM (Nexiv, Nikon, Japan). The test procedure consisted of applying a vertical force to press the head into the liner's edge while creating a record of the contact patch using a so-called fingerprinting technique (Sanders and Brannon, 2011) illustrated in the on-line material. The contact patch was measured at 37–143× magnification using the optical CMM. Tests were conducted on multiple liner edge points; the test matrix is in Table 4. For the CoC pairs, *Configuration 1* gave contact on *R Minor 1* (Fig. 2) and *Configuration 2* gave contact on *R Minor 2*; another created contact directly upon the crest (Fig. 2).

**Table 1**
Material properties for Hertzian contact analysis.

| Material | $Al_2O_3$[a] | CoCr[b] | XLPE[c] |
|---|---|---|---|
| Young's modulus (MPa) | 380,000 | 241,000 | 1040 |
| Poisson's ratio | 0.26 | 0.30 | 0.41 |

[a] Mak and Jin (2002)
[b] Manufacturer's data. BioDur CCM Plus, Carpenter, Wyomissing, PA, USA
[c] Manufacturer's data: Ortho Development, Draper, UT, USA.

## 3. Results

Fig. 4 shows the recorded contact patches with one example from each material pair. The on-line material provides additional examples, with a series of images for each material pair. The dimensional results are in Fig. 5, and Table 5 summarizes the results considering the complete load ranges. Table 6 gives statistics for several tests involving multiple trials. Graphs for the remaining contact pairs are in the on-line material.

## 4. Discussion

The fingerprinting contact measurement technique was inspired by Hertz, who used "the thinnest possible layer of lampblack" to measure small contacts in glass (Hertz, 1882). Fig. 6 graphs some of Hertz' experimental results. Similar to our results, Hertz' measurements were generally greater than his predictions, perhaps caused by squeezing of the lampblack outside of the true contact patch. In our technique, it is likely that contact would squeeze some of the grease slightly beyond the contact border; furthermore, powder particles may adhere to the transfer film's edge. Both effects could exaggerate contact dimensions, resulting in increasing relative error with decreasing contact size. In contrast, with Hertzian theory's assumption that the contact patch is small, its predictions of the contact dimensions should increase in accuracy with decreasing contact size, and

**Table 2**
Key edge dimensions (in mm) of $Al_2O_3$ liner specimens (*R Minor/Major* headings per Fig. 2).

| nom. ID | *R Minor 1* | *R Major 1* | *R Minor 2* | *R Major 2* | *R Minor 3* | *R Major 3* |
|---|---|---|---|---|---|---|
| ∅28 | 17.364 | 30.665 | 7.715 | 21.346 | 2.290 | 16.416 |
| ∅36 | 11.822 | 29.442 | 2.260 | 20.174 | n.a. | n.a. |

**Table 3**
Key edge dimensions (in mm) of CoCr and XLPE liner specimens.

| Material | nom. ID | *R Major* | *R Minor* |
|---|---|---|---|
| CoCr | ∅36 | 21.920 | 4.013 |
| XLPE | ∅28 | 16.807 | 2.54 |
| | ∅36 | 20.811 | 2.54 |

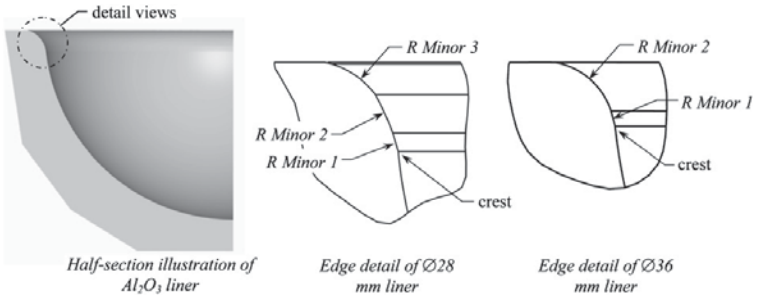


**Fig. 2.** Measurements revealed that the edge profile between the face and the ID of the $Al_2O_3$ liners was best described as a series of arc segments. Detail views illustrate the cross-sectional profiles of the ∅28 and ∅36 liners.

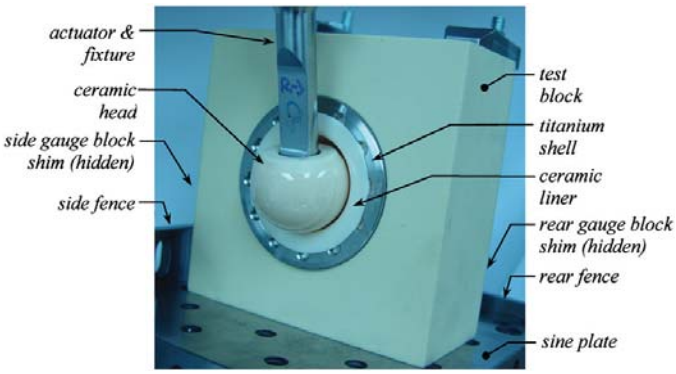


**Fig. 3.** Configuration of edge-load test on ceramic prostheses.

**Table 4**
Matrix of prosthesis edge loading tests. One specimen per pair. $\theta$ and $\delta$ per Fig. 1, $n$=number of trials performed.

| Pair | Size | Configuration 1 | | | Configuration 2 | | |
|---|---|---|---|---|---|---|---|
| | | $\theta$ (deg.) | $\delta$ (mm) | $n$ | $\theta$ (deg.) | $\delta$ (mm) | $n$ |
| CoC | 28 | 16.7° | 3.0 | 2 | 25 | 5.7 | 2 |
| CoC | 36 | 16.1° | 3.5 | 2 | 2 | 6.3 | 3 |
| CoM | 36 | 15° | n.a. | 1 | 30 | n.a. | 1 |
| CoP | 28 | 20° | 5.1 | 1–2 | – | – | – |
| CoP | 36 | 15° | 4.8 | 1–3 | – | – | – |

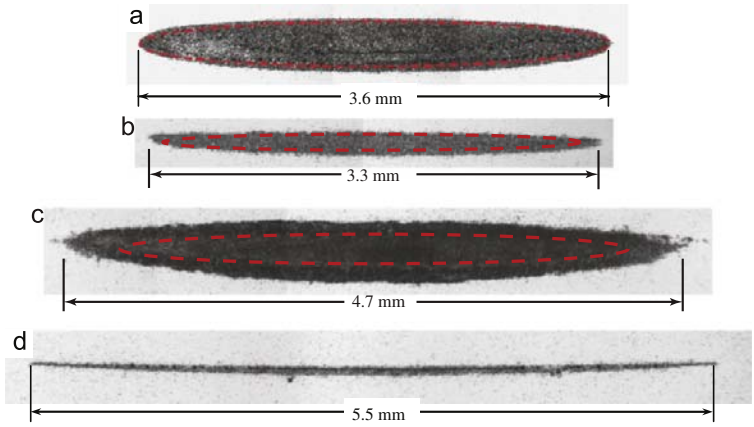


**Fig. 4.** Examples of recorded contact patches. Superimposed dashed red ellipses show Hertzian predictions. (a) CoC, ∅28, 1500 N, $\theta$=16.7°. (b) CoM, ∅36, 400 N, $\theta$=15°. (c) CoP, ∅28, 20 N, $\theta$=20°. (d) CoC, ∅36, 1000 N, contact on crest illustrated in Fig. 2.

vice versa. In Fig. 6, Hertz' data for load $<15$ kg shows an erratic error (percent difference), indicating that the measurement technique loses relative precision for small contact patches. The data for load $>15$ kg trends toward decreased error; this may indicate that with increasing contact size, decreasing measurement error overrides the diminution of the contact theory's accuracy. As described below, our results exhibited trends consistent with the sources of potential measurement error. Regarding repeatability of the results, the data ranges were larger for the CoP pairs than the CoC pairs (Table 6), probably because the rougher surface of the plastic parts made the contact patch borders less distinct. Based on the small ranges in the CoC tests, the CoM tests were performed using single trials.

Hertzian predictions were most accurate in the CoC pairs. Researchers have reported that $Al_2O_3$ maintains an elastic Hertzian response up to a mean contact pressure of ~5 GPa (maximum pressure ~7.5 GPa) (Guiberteau et al., 1994). In the present tests of the ∅36 pair, the maximum predicted $\overline{P}$ was 3.8 GPa, with $P_{max}$=5.7 GPa ($\theta$=25°, $Q$=2500 N); thus, based on the prior research, all the present CoC trials were within the

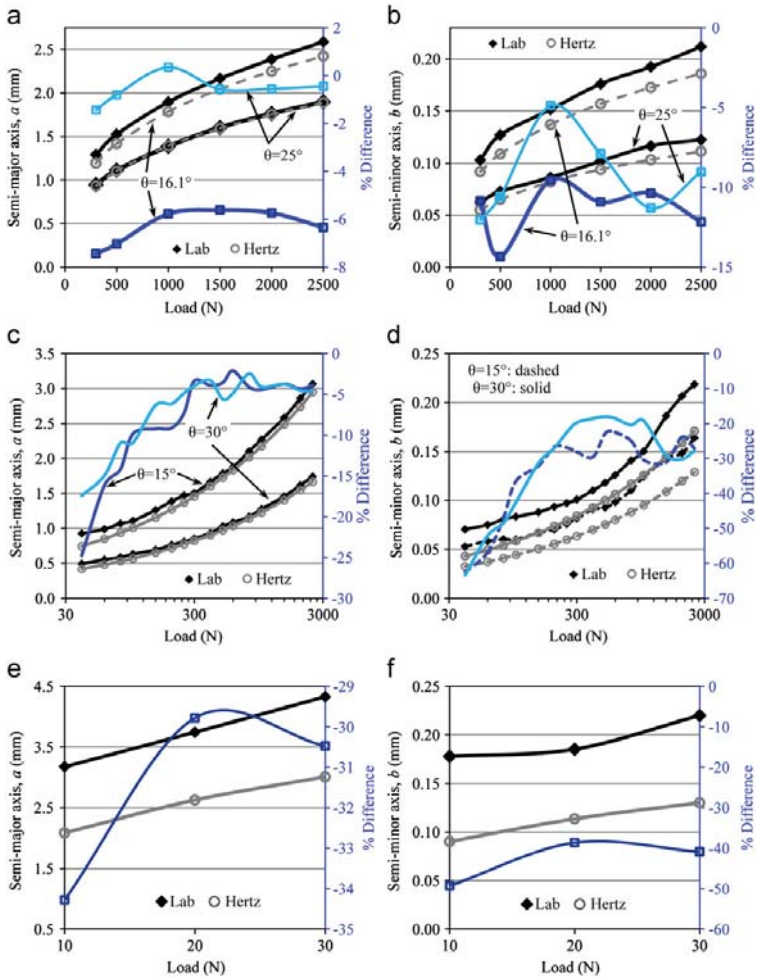


**Fig. 5.** Contact patch dimensions and % difference of Hertzian predictions compared to measurements. (a,b) CoC, ∅36. (c,d) MoM. (e,f) CoP, ∅36, θ=15°.

**Table 5**
Edge-loaded prostheses; difference between predicted and measured contact dimensions, summarized over the entire load range. (RMS=root-mean-square).

| Pair | $\theta$ | RMS difference | | mean % difference | |
|---|---|---|---|---|---|
| | | $a$ (μm) | $b$ (μm) | $a$ | $b$ |
| CoC ∅28 | 25.0° | 11.5 | 24.7 | 0.9% | −14.2% |
| | 16.7° | 15.1 | 28.4 | −0.3% | −15.7% |
| CoC ∅36 | 25.0° | 9.4 | 9.1 | −0.6% | −9.3% |
| | 16.1° | 124.7 | 18.7 | −6.3% | −11.4% |
| CoM ∅36 | 30° | 55.1 | 27.7 | −7.4% | −31.8% |
| | 15° | 105.6 | 22.5 | −7.7% | −33.1% |
| CoP ∅28 | 20° | 524.4 | 113.3 | −21.3% | −47.4% |
| CoP ∅36 | 15° | 1178.8 | 83.5 | −31.5% | −42.9% |

elastic range. The predictions were more accurate at $\theta=25°$ than at $\theta=16.1°$, which is expected because $\theta=25°$ gives reduced surface conformity and therefore better satisfaction of the theory's assumptions. The error in semi-minor $b$ (roughly, 10–15%) was greater than that in semi-major $a$ (roughly, 1–8%). This is explained by the tendency of the measurement technique to exaggerate smaller contact patch dimensions, which was also manifested by increasing error with decreasing $a$. The lowest-error results in $a$ ( $<2\%$ Dif., Fig. 5a, $\theta=25°$) compare favorably with Hertz' results ( $<4\%$ Dif., Fig. 6), in spite of our greater measurement complexity (opaque materials and a grease transfer film). An assessment of the theory's accuracy for CoC edge loading is difficult due to measurement error and the lack of an independent measurement standard. Yet, after slightly discounting the

**Table 6**
Statistics from several tests with multiple trials (semi-axis dimensions in μm).

| Pair | ∅28 CoC | | ∅36 CoC | | ∅28 CoP | | ∅36 CoP | |
|---|---|---|---|---|---|---|---|---|
| Orientation | 16.7° | | 25° | | 20° | | 15° | |
| Load | 1000 N | | 1500 N | | 10 N | | 10 N | |
| No. of trials | 2 | | 3 | | 2 | | 3 | |
| Semi-axis | $a$ | $b$ | $a$ | $b$ | $a$ | $b$ | $a$ | $b$ |
| Mean | 1577 | 180 | 1604 | 102 | 2255 | 220 | 3175 | 178 |
| Range | 6 | 1 | 9 | 4 | 36 | 15 | 63 | 29 |

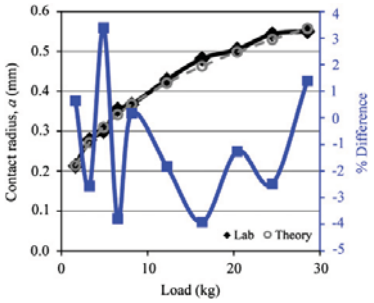


**Fig. 6.** Hertz' original experimental contact data, graphed from data in (Hertz (1882).

size-dependent error in $b$, Hertzian predictions conservatively have $<10\%$ error for CoC edge loading.

In the CoM pair, maintenance of elastic conditions may be judged approximately using a criterion for avoiding subsurface yield in circular contacts, $\overline{P}<1.1S_y$ (Fischer-Cripps, 2000), where $S_y$ is the metal's tensile yield strength (965 MPa, certification data). For example, at $\theta=15^\circ$ and 400 N, the predicted $\overline{P}$ was 1134 MPa; this fails the criterion, so subsurface yield likely occurred in the CoCr for $Q\geq 400$ N. Each trial was conducted at a fresh edge point, and no permanent indentations were observed. In spite of predicted plasticity, the CoM contact patches were elliptical, and both $a$ and $b$ followed the trends predicted by the Hertzian theory. The error in $a$ was consistently around $-5\%$ for $Q\geq 300$ N, indicating that $a$ was large with respect to a subsurface plastic zone. In contrast, the error in $b$ trended greater with $Q>400$ N, indicating that plasticity had a noticeable effect on this smaller dimension. In both $a$ and $b$, the error clearly trended greater for $Q<300$ N, probably due to the size-dependent measurement errors. To consider metal-on-metal (*MoM*) contact, we analyzed a $\varnothing 36$ mm CoCr head-liner contact at $\theta=15^\circ$. This virtual pair gave $\overline{P}>1.1S_y$ at $Q=490$ N; thus, in a *MoM* pair, a higher load is needed to induce subsurface plasticity than in a CoM pair. The propensity for subsurface yield means that Hertzian predictions have a limited range of accuracy, roughly $<400$ N in this study, in edge-loaded metal bearings. Measurement errors limited our ability to demonstrate the theory's applicability throughout this load range; yet, in $a$, the error was $<10\%$ for $Q>100$ N.

The error was greatest in the XLPE liners, which is attributed to the material's nonlinear elastic properties. As an example, the $\varnothing 36$ pair at $\theta=15^\circ$ and 10 N had a predicted $P_{max}$ of 25.3 MPa, a value that is beyond XLPE's small linear range ($<10$ MPa, manufacturer's data). The CoP pairs are an example for which edge-load contact cannot be accurately analyzed using the Hertzian theory. This conclusion may be extrapolated to metal-on-plastic (MoP) pairs, because CoP and MoP each act essentially as a rigid-compliant pair (Bartel et al., 1985).

The contact pressure caused by edge loading is much greater than that caused by concentric contact. For example, with the $\varnothing 36$ $Al_2O_3$ pair edge loaded to 1000 N ($\theta=16.1^\circ$), $P_{max}$ is 1950 MPa, but for concentric contact, it is 45 MPa. Similar dramatic differences were reported in a FEA of microseparation (Mak et al., 2002). Researchers reported contact pressures $>1$ GPa for head-liner contact in FEA of edge-loaded hard bearings (Elkins et al., 2011). Small elements are needed to yield highly accurate estimates of edge-loaded contact stresses by FEA. Elkins et al. reported that $\sim 20$ elements/mm$^3$ were needed to obtain convergence to the "gold standard" Hertzian analysis. Yet, this volumetric density implies an element edge length of 0.36 mm, which would be insufficient to accurately model the small contact patch minor axes (e.g. $<0.3$ mm) seen in the present study. Submodelling techniques have been used for FEA of small stress concentrations and contacts (Cormier et al., 1999), and these techniques may enable more accurate FEA of edge-loaded hip bearings. The present study's results and techniques may serve to experimentally validate such analyses.

The separation $\delta$ (Fig. 1) was 3.0–3.5 mm for angles $\theta\approx 16^\circ$, which is near the upper end of fluoroscopically measured values (Lombardi et al., 2000; Dennis et al., 2001; Komistek et al., 2002). Separation of $\sim 6$ mm for $\theta=25^\circ$ is beyond values measured *in-vivo*. The $\delta$ values were chosen partly to reflect *in-vivo* measurements (thus $\delta=2$, 3.0, and 3.5 mm), and partly to broaden the range of conditions (thus $\delta=6$, 6.5 mm) and better elucidate the applicability of the Hertzian theory. Little is currently known about the *in-vivo* contact loads experienced during subluxation; therefore, this study examined widely varying loads to reflect the likelihood that *in-vivo* contact loads span a broad range.

Researchers have subjected fine-grained $Al_2O_3$ to reciprocated sliding under a mean contact pressure of 950 MPa, which elicited severe intergranular fracture and grain pullout in 12,000 cycles (Cho et al., 1992); CoC hip stripe wear is characterized by a similar microstructural appearance (Walter et al., 2004). For further comparison, analysis of the $\varnothing 36$ CoC pair ($\theta=16.1^\circ$) shows that $\overline{P}=950$ MPa is attained at $Q\approx 400$ N. From these data, it appears that relatively low edge-load contact forces, occurring repeatedly during *in-vivo* subluxation, could be sufficient to cause CoC stripe wear. Notably, a 400 N spring force was employed to instigate edge loading in microseparation wear tests that produced CoC stripe wear (Nevelos et al., 2000).

The ceramic liners' crests (Fig. 2) have been observed previously (Walter et al., 2004). In this study, contact upon this crest occurred for a separation, $\delta=2.0$ mm, equal to the average observed in a group of treadmill-walking hip replacement patients (Komistek et al., 2002). The observed contact patch (Fig. 4d) had 15% less area than the patch at $\delta=3.0$ mm ($\theta=16.1^\circ$). This implies that crest loading induces particularly elevated contact stresses, which exposes yet another potential cause of stripe wear.

This study has provided extensive evidence that the accuracy of the Hertzian contact theory for predicting contact dimensions in edge loading depends on the bearing materials and the contact position. The theory is most applicable in CoC pairs (with error $<10\%$) because these maintain elastic response to high contact pressures. This finding is valuable because it implies that the Hertzian theory may be used to predict edge loading contact stresses (see, e.g. Fabrikant, 2005), thereby expediting development of materials and components that are more durable under adverse loads. The Hertzian theory should also be useful for edge-loaded CoM (and MoM) bearings, though for loads $<400$ N since, above that, subsurface plasticity is predicted. The theory is ill-suited to CoP (and MoP) bearings due to nonlinear material behavior.

## Conflict of interest statement

The authors declare that they have no conflicts of interest in publishing this article.

## Acknowledgments

This work was supported by Award #R21AR056374 from the NIAMS/NIH.

## Appendix A. Supplementary materials

Supplementary materials associated with this article can be found in the on-line version at doi:10.1016/j.jbiomech.2011.08.007.

## References

Bartel, D.L., Burstein, A.H., Toda, M.D., Edwards, D.L., 1985. The effect of conformity and plastic thickness on contact stresses in metal-backed plastic implants. Journal of Biomechanical Engineering 107, 193–199.

Bourne, R.B., Barrack, R., Rorabeck, C.H., Salehi, A., Good, V., 2005. Arthroplasty options for the young patient: oxinium on cross-linked polyethylene. Clinical Orthopaedics and Related Research 441, 159–167.

Callanan, M.C., Jarrett, B., Bragdon, C.R., Zurakowski, D., Rubash, H.E., Freiberg, A.A., Malchau, H., 2010. The John Charnley Award: risk factors for cup malpositioning: quality improvement through a joint registry at a tertiary hospital. Clinical Orthopaedics and Related Research 18, 18–28.

Cho, S.J., Moon, H., Hockey, B.J., Hsu, S.M., 1992. The transition from mild to severe wear in alumina during sliding. Acta Metallurgica et Materialia 40, 185–192.

Cormier, N.G., Smallwood, B.S., Sinclair, G.B., Meda, G., 1999. Aggressive submodelling of stress concentrations. International Journal for Numerical Methods in Engineering 46, 889–909.

Crowninshield, R.D., Maloney, W.J., Wentz, D.H., Humphrey, S.M., Blanchard, C.R., 2004. Biomechanics of large femoral heads: what they do and don't do. Clinical Orthopaedics and Related Research 429, 102–107.

Dennis, D., Komistek, R., Northcut, E., Ochoa, J., Ritchie, A., 2001. In-vivo determination of the hip joint separation and the forces generated due to impact loading conditions. Journal of Biomechanics 34, 623–629.

Elkins, J.M., O'Brien, M.K., Stroud, N.J., Pedersen, D.R., Callaghan, J.J., Brown, T.D., 2011. Hard-on-hard total hip impingement causes extreme contact stress concentrations. Clinical Orthopaedics and Related Research 469, 454–463.

Erdelyi, A., 1953. Higher Transcendental Functions. McGraw-Hill, New York.

Fabrikant, V.I., 2005. A new symbolism for solving the Hertz contact problem. Quarterly Journal of Mechanics and Applied Mathematics 58, 367–381.

Fischer-Cripps, A.C., 2000. Introduction to Contact Mechanics. Springer, New York.

Guiberteau, F., Padture, N.P., Lawn, B.R., 1994. Effect of grain size on Hertzian contact damage in alumina. Journal of the American Ceramic Society 77, 1825–1831.

Harris, T.A., 1991. Rolling Bearing Analysis. John Wiley & Sons, New York.

Hertz, H., 1882. On the contact of rigid elastic solids and on hardness. In: Schott, J.A. (Ed.), Miscellaneous papers by H. Hertz. MacMillan, London, pp. 164–183.

Irons, M.L., 2005. The curvature and geodesics of the torus. Retrieved January 20, 2008 Available from: 〈http://www.rdrop.com/~half/math/torus/index.xhtml〉.

Johnson, K.L., 1985. Contact Mechanics. Cambridge University Press, Cambridge.

Kluess, D., Martin, H., Mittelmeier, W., Schmitz, K.P., Bader, R., 2007. Influence of femoral head size on impingement, dislocation and stress distribution in total hip replacement. Medical Engineering and Physics 29, 465–471.

Komistek, R.D., Dennis, D.A., Ochoa, J.A., Haas, B.D., Hammill, C., 2002. In vivo comparison of hip separation after metal-on-metal or metal-on-polyethylene total hip arthroplasty. Journal of Bone and Joint Surgery American Volume 84, 1836–1841.

Lewinnek, G.E., Lewis, J.L., Tarr, R., Compere, C.L., Zimmerman, J.R., 1978. Dislocations after total hip-replacement arthroplasties. Journal of Bone and Joint Surgery American 60, 217–220.

Lombardi, A.V., Mallory, T.H., Dennis, D.A., Komistek, R.D., Fada, R.A., Northcut, E.J., 2000. An in vivo determination of total hip arthroplasty pistoning during activity. Journal of Arthroplasty 15, 702–709.

Mak, M.M., Besong, A.A., Jin, Z.M., Fisher, J., 2002. Effect of microseparation on contact mechanics in ceramic-on-ceramic hip joint replacements. Proceedings of the Institution of Mechanical Engineers. Part H: Journal of Engineering in Medicine 216, 403–408.

Mak, M.M., Jin, Z.M., 2002. Analysis of contact mechanics in ceramic-on-ceramic hip joint replacements. Proceedings of the Institution of Mechanical Engineers, Part H: Journal of Engineering in Medicine 216, 231–236.

Manaka, M., Clarke, I.C., Yamamoto, K., Shishido, T., Gustafson, A., Imakiire, A., 2004. Stripe wear rates in alumina THR — comparison of microseparation simulator study with retrieved implants. Journal of Biomedical Materials Research—Part B Applied Biomaterials 69, 149–157.

Mellon, S.J., Simpson, D.J., Kwon, Y.M., Murray, D.W., Gill, H.S., 2010. The influence of acetabular component orientation on stress during gait in metal-on-metal hip resurfacing. In: Proceedings of the 56th Annual Meeting of the Orthopaedic Research Society, New Orleans.

Nadzadi, M.E., Pedersen, D.R., Callaghan, J.J., Brown, T.D., 2002. Effects of acetabular component orientation on dislocation propensity for small-head-size total hip arthroplasty. Clinical Biomechanics 17, 32–40.

Nevelos, J., Ingham, E., Doyle, C., Streicher, R., Nevelos, A., Walter, W., Fisher, J., 2000. Microseparation of the centers of alumina—alumina artificial hip joints during simulator testing produces clinically relevant wear rates and patterns. Journal of Arthroplasty 15, 793–795.

Nikas, G.K., 2002. Fatigue life and traction modeling of continuously variable transmissions. Journal of Tribology 124, 689–698.

Sanders, A.P., Brannon, R.M., 2011. Determining a surrogate contact pair in a Hertzian contact problem. Journal of Tribology 133, 024502–024506.

Sariali, E., Stewart, T., Jin, Z., Fisher, J., 2010. Three-dimensional modeling of in vitro hip kinematics under micro-separation regime for ceramic on ceramic total hip prosthesis: an analysis of vibration and noise. Journal of Biomechanics 43, 326–333.

Scifert, C.F., Noble, P.C., Brown, T.D., Bartz, R.L., Kadakia, N., Sugano, N., Johnston, R.C., Pedersen, D.R., Callaghan, J.J., 2001. Experimental and computational simulation of total hip arthroplasty dislocation. Orthopedic Clinics of North America 32, 553–567.

Taylor, S., Manley, M.T., Sutton, K., 2007. The role of stripe wear in causing acoustic emissions from alumina ceramic-on-ceramic bearings. Journal of Arthroplasty 22, 47–51.

Walter, W.L., Insley, G.M., Walter, W.K., Tuke, M.A., 2004. Edge loading in third generation alumina ceramic-on-ceramic bearings: stripe wear. Journal of Arthroplasty 19, 402–413.

Yamamoto, T., Saito, M., Ueno, M., Hananouchi, T., Tokugawa, Y., Yonenobu, K., 2005. Wear analysis of retrieved ceramic-on-ceramic articulations in total hip arthroplasty: femoral head makes contact with the rim of the socket outside of the bearing surface. Journal of Biomedical Materials Research—Part B Applied Biomaterials 73, 301–307.

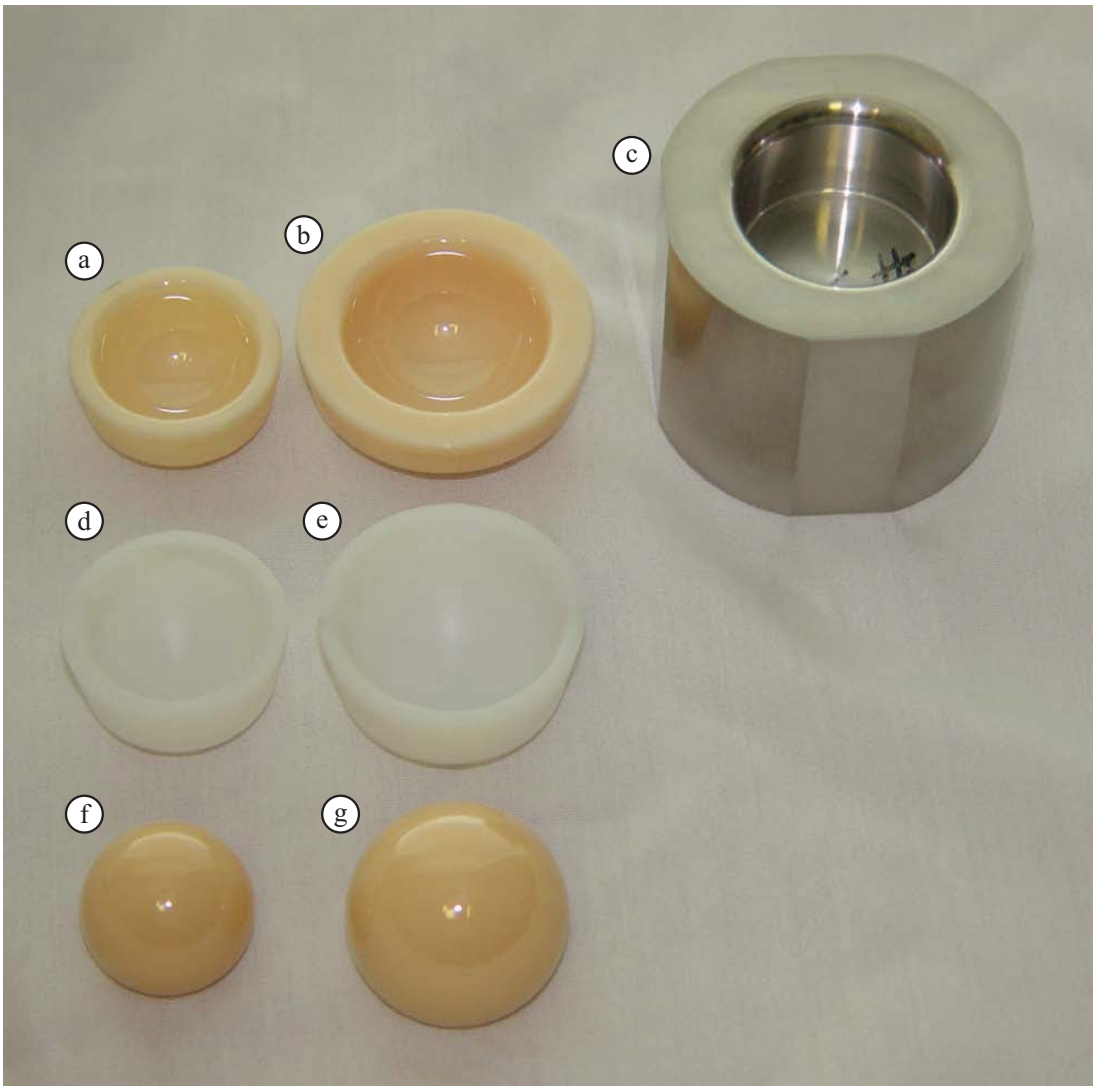


Figure S1: Components used in contact tests. a) Ø28 $Al_2O_3$ liner. b) Ø36 $Al_2O_3$ liner. c) Ø36 CoCr liner; this custom-made component implemented cylindrical inner and outer surfaces to reduce fabrication cost, but nonetheless had a torus-shaped edge mimicking that of a full-featured CoCr liner. d) Ø28 XLPE liner. e) Ø36 XLPE liner. f) Ø28 $Al_2O_3$ femoral head. b) Ø36 $Al_2O_3$ femoral head.

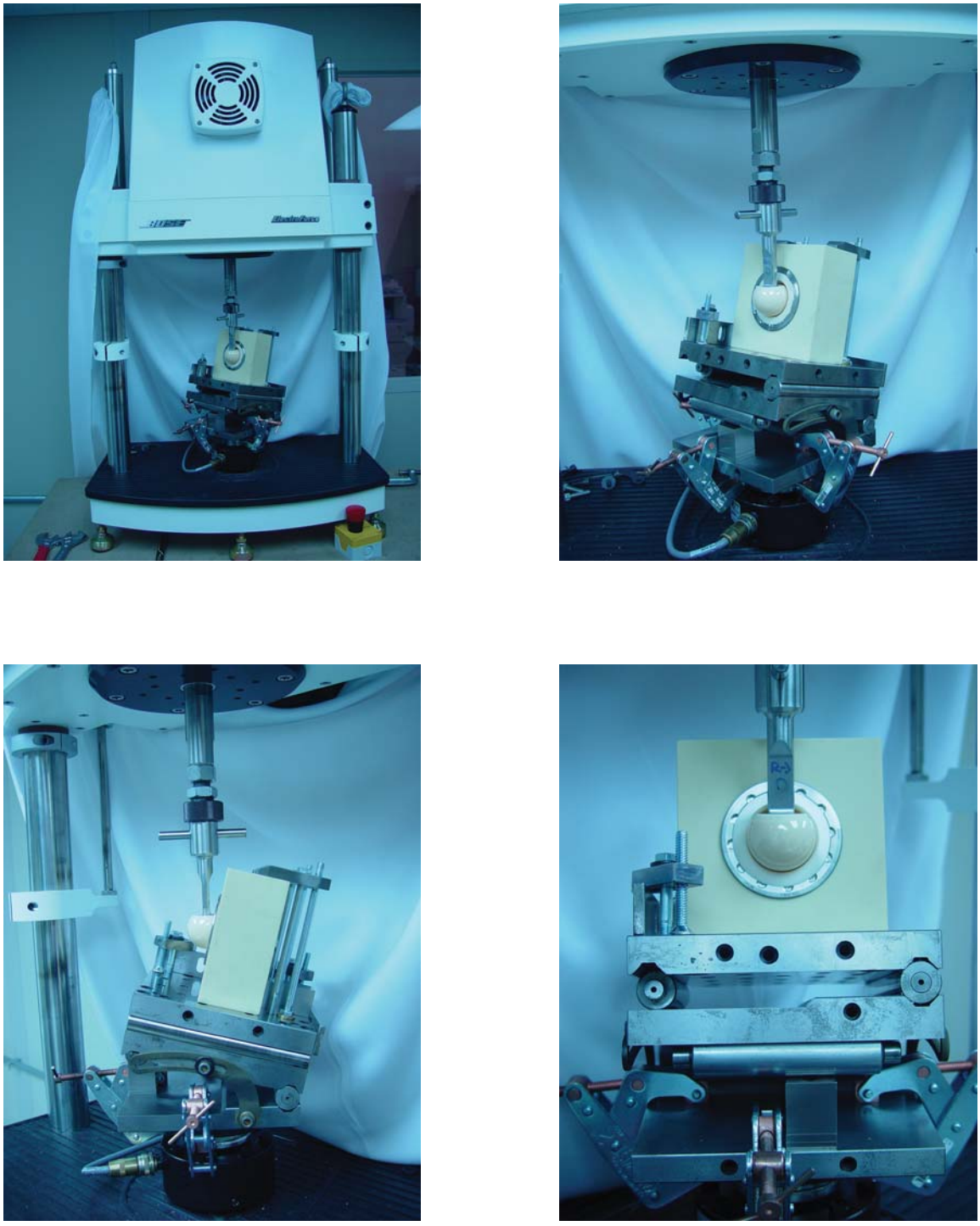

Figure S2: Photos of edge load contact test set-up, displaying components for ceramic-on-ceramic test.

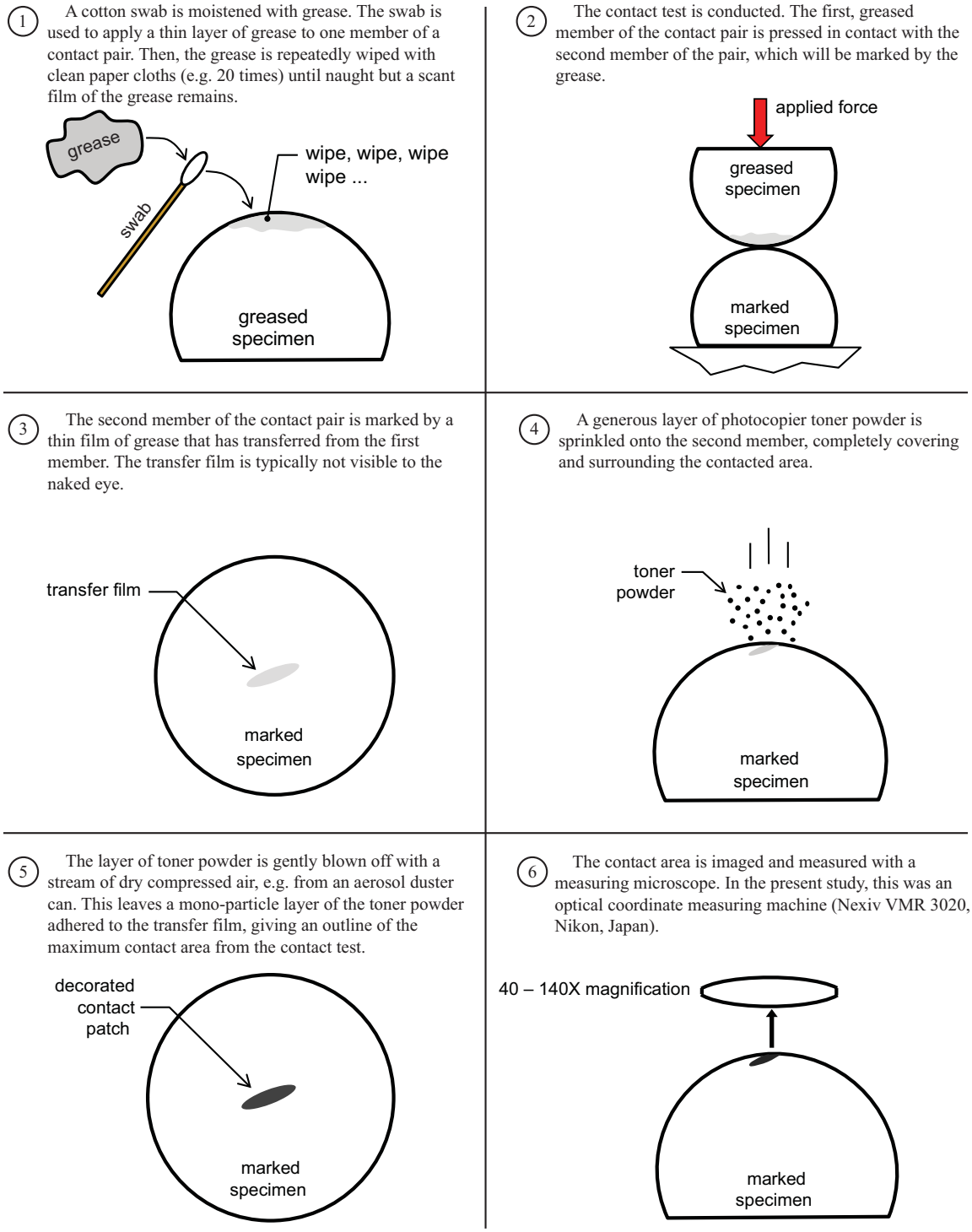


Figure S3: Outline of the “fingerprinting” technique used to record the contact area during a contact test

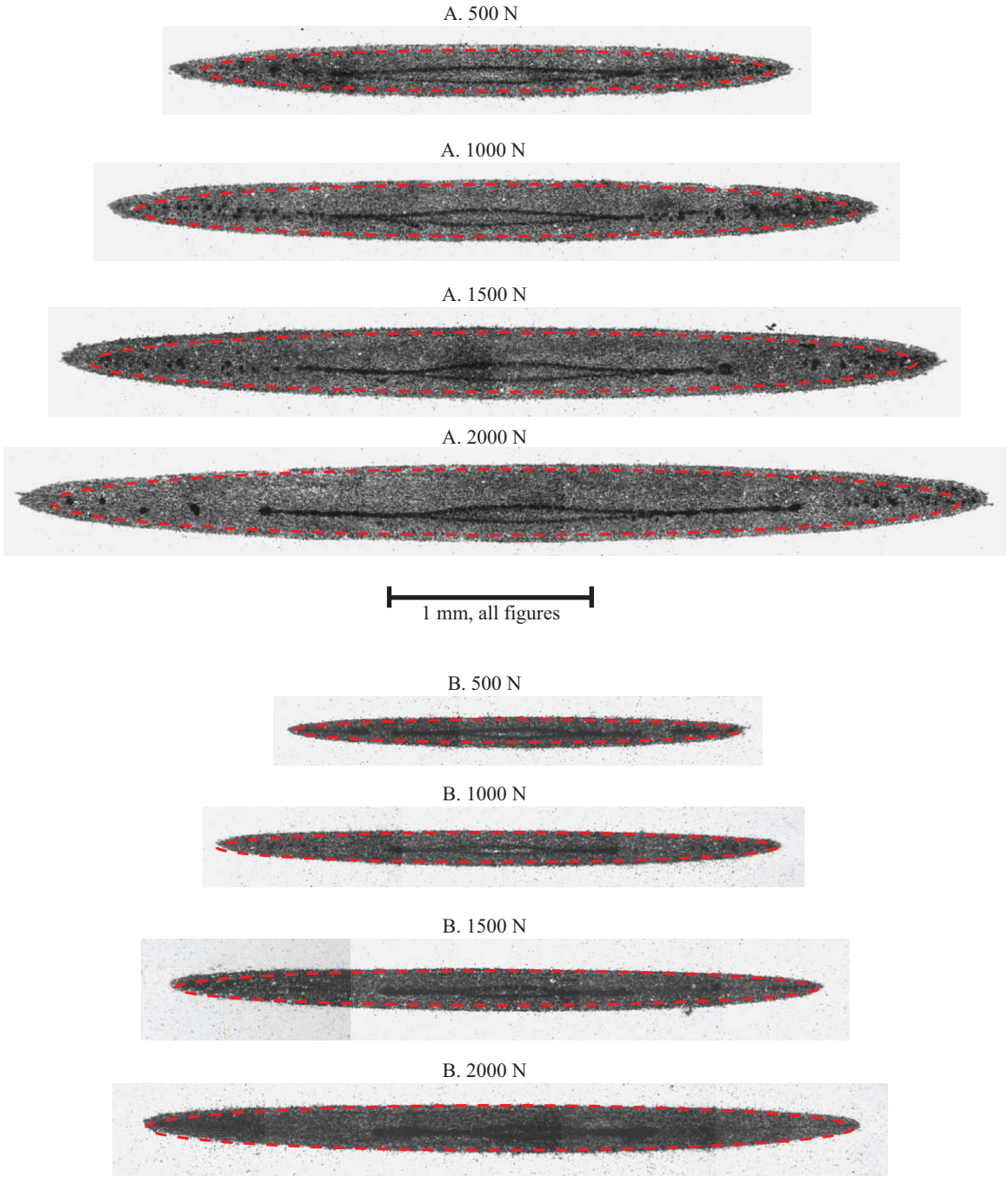


Figure S4: Contact patches recorded in two series of tests of the Ø36 mm CoC pair at increasing applied loads. The superimposed red, dashed ellipses show the contact perimeters predicted by Hertzian theory. Series A: Liner angle θ = 16.1°; Series B: θ = 25°.

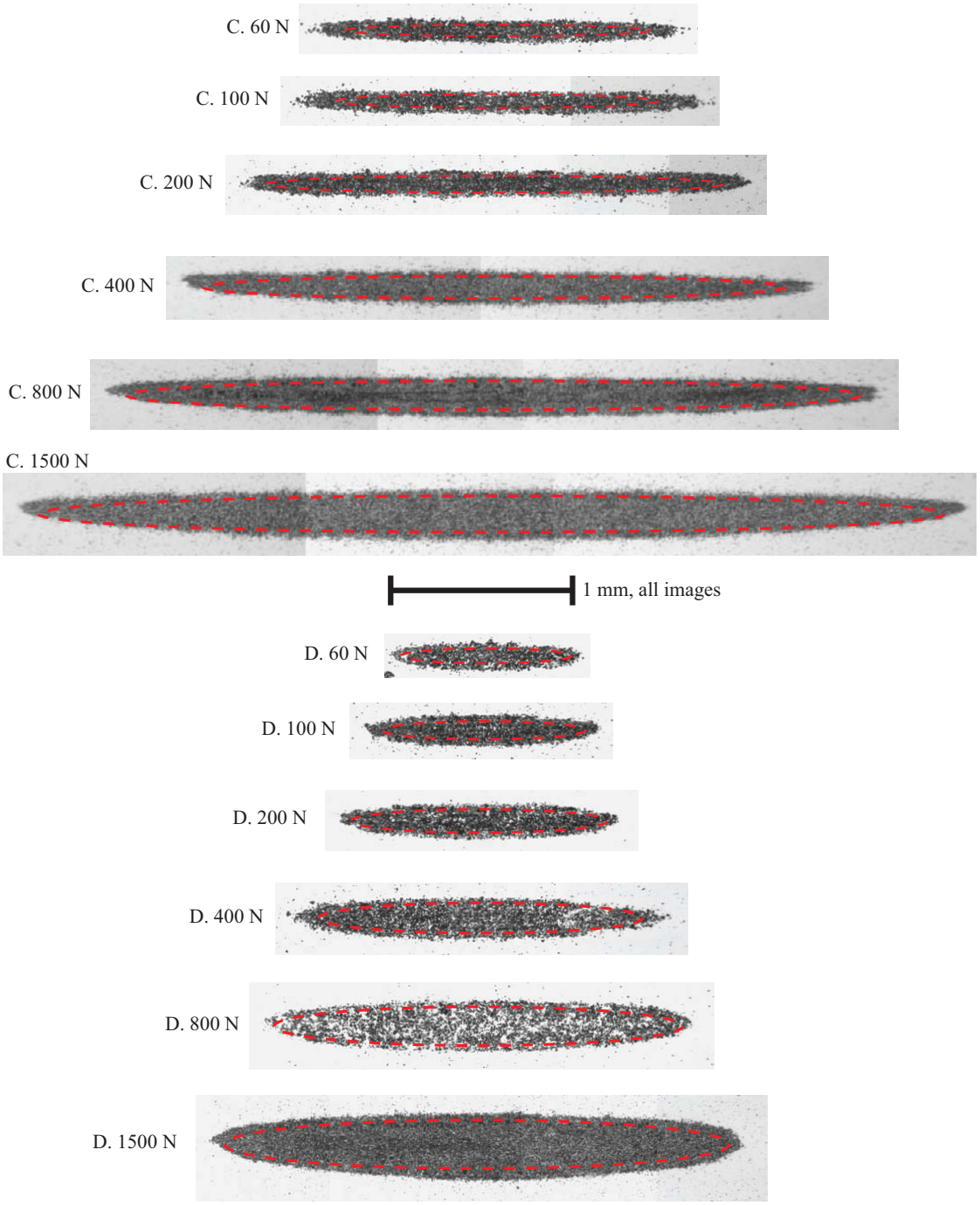


Figure S5: Contact patches recorded in two series of tests of the Ø36 mm CoM pair at increasing applied loads. The superimposed red, dashed ellipses show the contact perimeters predicted by Hertzian theory. Series C: Liner angle θ = 15°; Series D: θ = 30°.

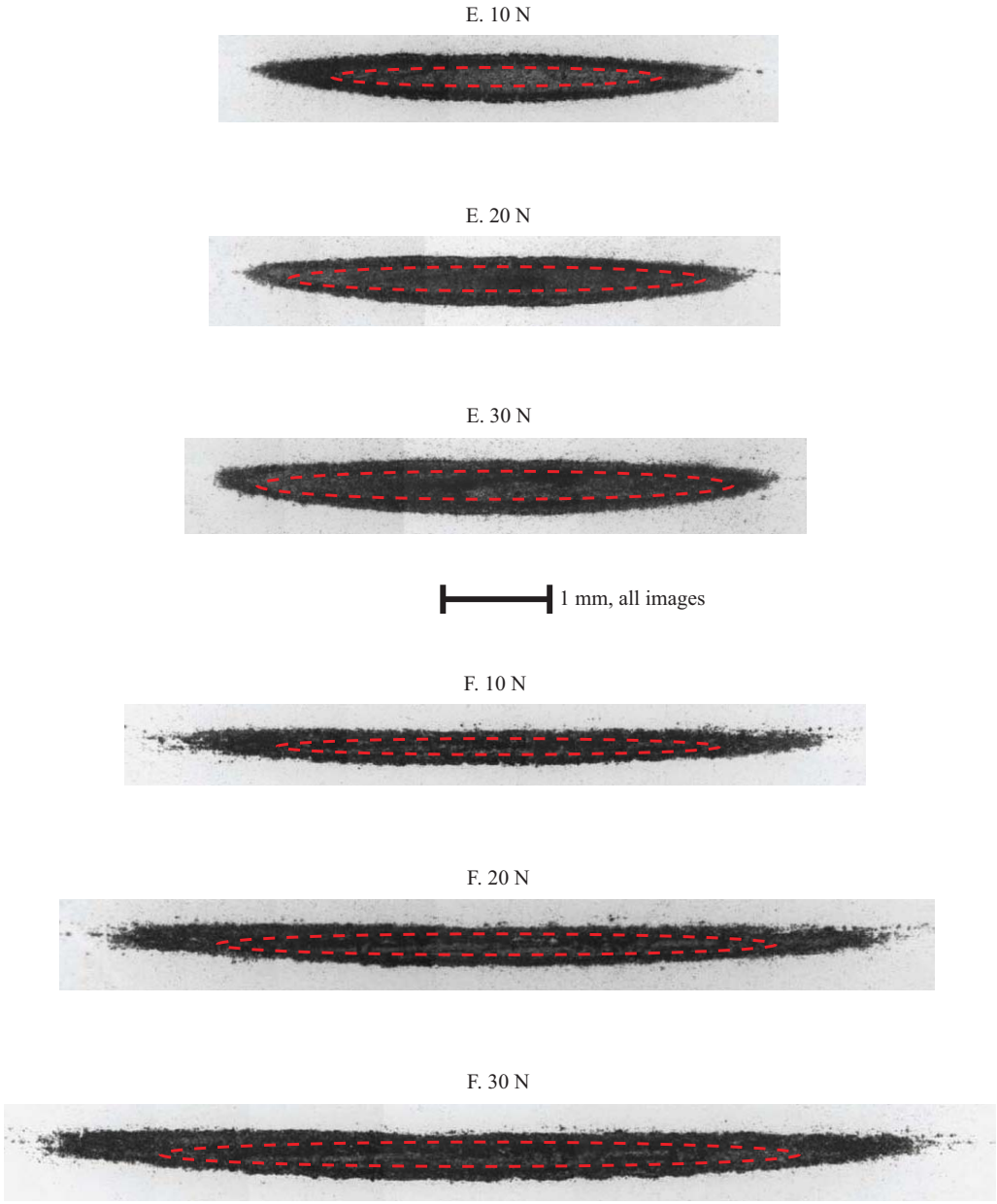


Figure S6: Contact patches recorded in two series of tests of the CoP pairs at increasing applied loads. The superimposed red, dashed ellipses show the contact perimeters predicted by Hertzian theory. Series E: Ø28 with liner angle $\theta = 20°$; Series F: Ø36, $\theta = 15°$.

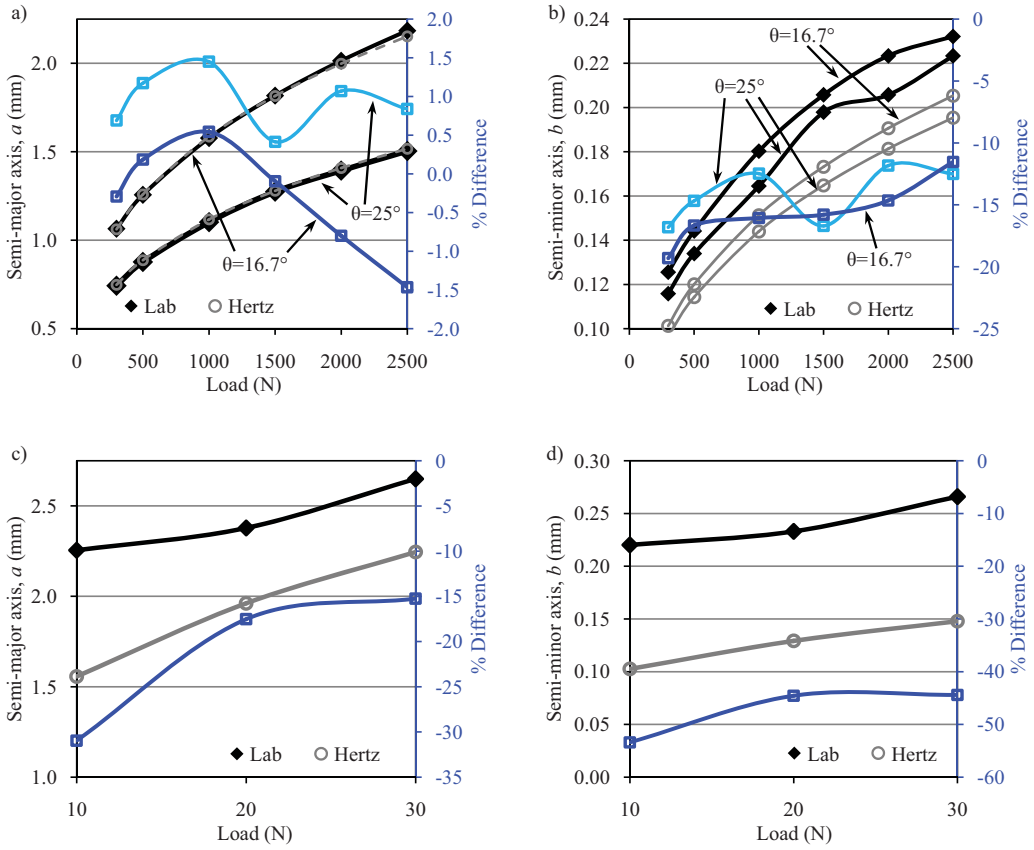


Figure S7: Contact patch dimensions and %difference of Hertzian predictions compared to measurements.

a) and b) CoC, ∅28. c) and d) CoP, ∅28, θ=20°.

Table S1: Summary statistics from ∅36 CoC pair at two loads, 3 trials each. Values in µm.

| Semi-axis | $Q$ = 300 N | | | $Q$ = 1500 N | | |
|---|---|---|---|---|---|---|
| | mean | range | std dev | mean | range | std dev |
| *a* | 946.1 | 19.0 | 9.6 | 1,603.6 | 9.2 | 5.0 |
| *b* | 62.4 | 0.9 | 0.5 | 101.9 | 3.7 | 1.9 |

CHAPTER 4

# CONTACT MECHANICS OF IMPACTING SLENDER RODS:

# MEASUREMENT AND ANALYSIS



Sanders, A., Tibbitts, I., Kakarla, D., Siskey, S., Ochoa, J., Ong, K., Brannon, R., 2011, "Contact Mechanics of Impacting Slender Rods: Measurement and Analysis," in *Dynamic Behavior of Materials, Volume 1, Proceedings of the 2011 Annual Conference on Experimental and Applied Mechanics*, Proulx, T., Ed. Springer, New York, pp. 229-236.

# Contact Mechanics of Impacting Slender Rods: Measurement and Analysis

Anthony Sanders[1], M.S., Ira Tibbitts[1], B.S., Deepika Kakarla[1], B.E., Stephanie Siskey[2], B.S., Jorge Ochoa[3], Ph.D., Kevin Ong[2], Ph.D., and Rebecca Brannon[1], Ph.D.
[1] University of Utah, Dept. of Mechanical Engineering, 2134 MEB, Salt Lake City, UT 84112
[2] Exponent, Inc., 3401 Market St., Suite 300, Philadelphia, PA, 19104
[3] Exponent, Inc., 15375 SE 30th Place, Suite 250, Bellevue, WA 98007

## ABSTRACT

To validate models of contact mechanics in low speed structural impact, slender rods with curved tips were impacted in a drop tower, and measurements of the contact and vibration were compared to analytical and finite element (FE) models. The contact area was recorded using a thin-film transfer technique, and the contact duration was measured using electrical continuity. Strain gages recorded the vibratory strain in one rod, and a laser Doppler vibrometer measured velocity. The experiment was modeled analytically using a quasi-static Hertzian contact law and a system of delay differential equations. The FE model used axisymmetric elements, a penalty contact algorithm, and explicit time integration. A small submodel taken from the initial global model economically refined the analysis in the small contact region. Measured contact areas were within 6% of both models' predictions, peak speeds within 2%, cyclic strains within 12 microstrain (RMS value), and contact durations within 2 μs. The accuracy of the predictions for this simple test, as well as the versatility of the diagnostic tools, validates the theoretical and computational models, corroborates instrument calibration, and establishes confidence that the same methods may be used in an experimental and computational study of the impact mechanics of artificial hip joints.

## 1. Introduction

The problem of analyzing the impact of slender rods has previously been addressed in several classical works [1-3]. Recent approaches have included substructure analysis [4] and modal analysis combined with a Hertzian contact law [5,6]. FEA has been applied to problems of a single impacted rod [7,8] and two impacting rods [9], with results that have shown close fidelity to analytical models. Considering experimental approaches, contact duration between impacting metallic spheres and rods has been measured using electrical continuity [10,11]. Strain gages have been used to measure the strain waves in impacted rods [1,12-15]. Recently, laser vibrometry has been employed to measure the transient velocity on the surface of a rod impacted by a sphere [6,8,12,13]. Notably, the problem of a sphere striking the end of a long rod was formulated using a system of delay differential equations [12,13]. Viewing the effectiveness of this approach, one aim of the present work is to extend this recently demonstrated approach to the case of two impacting rods, and to add experimental validation of the predicted contact mechanics.

To date, neither the contact area nor contact stress generated by such impacts has been adequately analyzed and experimentally validated. It is difficult to experimentally record a small, transient elastic contact area; even so, practical methods have been described [16,17], including a recent one of our own design that uses inexpensive materials: grease and photocopier powder [18]. Accordingly, the second aim of the present work is to measure the contact area generated between impacting spherically tipped rods. The results will validate the analytical use of a Hertzian contact law to describe the force-displacement relation at the impact site.

Hertzian theory can provide comprehensive contact mechanics predictions [19,20], but its accuracy depends upon assumptions that may be ill-suited to some impact problems. FEA also provides a means of examining impact-induced contact stress; however, sufficient mesh refinement in the case of small contacts may require small elements that entail high computational cost. In the submodelling technique in FEA, the results of a coarsely meshed global model are applied as boundary conditions to a submodel of a small area of interest that requires a refined mesh. Submodelling has been applied in FEA where a contact area of interest was a small portion of a larger model [21,22].

Hence, two approaches, analytical and FEA, are suited to simulating the two-rod impact problem on both the macro and micro-scales. Likewise, experimental techniques may validate the simulations' results on both scales. Therefore, this work aims to demonstrate both simulation approaches and to compare their predictions with experimental outcomes, at both scales.

## 2. Methods and materials

### *2.1. Analytical model*

The analysis begins with the schematic in Fig. 1. Rod 1 with speed $s_1$ travels axially and impacts stationary Rod 2. The rods are parallel, and the impact is centric. Dimensions $d_i$ give the diameters, $r_i$ the tip radii, and $L_i$ the lengths. The rods' coordinates, $x_1$ and $x_2$, are measured inward from the radiused tip, and the rods are modeled as homogeneous, linear elastic, and isotropic; accordingly, the material properties are the densities $\rho_i$, elastic modulii $E_i$, and Poisson's ratios $\nu_i$.

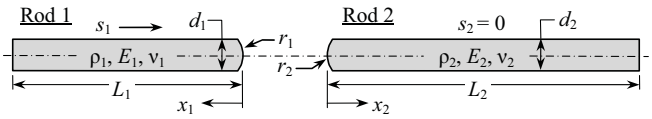


**Fig. 1** Schematic for the axial, centric impact of two slender rods

The governing equation of each rod is approximately the 1D wave equation [1]. In Rod 2, the general solution is [23]:

$$u_2(x_2,t) = f_2(t - x_2/c_2) + g_2(t + x_2/c_2) \tag{1}$$

Here, $u_2$ is the displacement and $c_2=\sqrt{E_2/\rho_2}$ is the longitudinal wave speed. This solution represents two waves: right-traveling unknown function $f_2(\ )$ and left-traveling unknown function $g_2(\ )$ [1]. A similar equation applies to Rod 1, although a reversal of the left/right description applies since $x_1$ is *positive leftward*. The stress-free boundary condition at $x_2=L_2$ implies the strain-free condition $\partial u_2/\partial x_2=0$, which yields $g'_2(t+L_2/c_2)=f'_2(t-L_2/c_2)$, where $(')$ denotes differentiation with respect to the entire argument. This expression holds at an offset instant $t_o=t-L_2/c_2$, which yields:

$$g'_2(t) = f'_2(t - 2L_2/c_2) \tag{2}$$

At the impacted end ($x_2=0$), the strain is related to the stress via Hooke's law: $\partial u_2/\partial x_2=F(t)/E_2A_2$, where $F(t)$ is the contact force during impact and $A_2$ is the cross-sectional area. Applied to Eq. (1), this yields:

$$f'_2(t) = g'_2(t) - c_2F(t)/E_2A_2 \tag{3}$$

This assumes that the contact force is uniformly distributed across the impacted end, which is inaccurate in the vicinity of the contact, but is nevertheless appropriate to model the wave motion far from the point of contact based on St. Venant's principle. In the contact region, the contact force is related to the displacement by a Hertzian contact law [13]: $F(t)= -K[\delta(t)]^{3/2}$, where $K$ is the Hertzian contact stiffness (addressed below), and $\delta(t)$ is the compression due to impact; the negative sign yields a compressive (negative) force and stress. The compression is the difference in rod displacements at the impacted ends: $\delta(t)= -u_1(0,t) -u_2(0,t)$, which treats the impacted ends' displacements as uniform over the cross-section of each rod.

In Rod 1, the strain rate at the free end ($x_1=L_1$) is zero: $\partial u_1/(\partial x_1\partial t)=[-f''_1(t-x_1/c_1)+ g''_1(t+x_1/c_1)]/c_1=0$. This holds at an offset instant $t_o=t-L_1/c_1$, which yields:

$$g''_1(t) = f''_1(t - 2L_1/c_1) \tag{4}$$

Evaluating the strain rate at the impacted end ($x_1=0$) yields: $\partial u_1/(\partial x_1\partial t)=[ -f''_1(t)+ g''_1(t)]/c_1= F'(t)/E_1A_1$. Thus:

$$f''_1(t) = g''_1(t) + \tfrac{3}{2}(c_1K/E_1A_1)\sqrt{\delta(t)}\,\dot{\delta}(t) \tag{5}$$

The rate of compression in Eqn. (5) is derived from the compression relation, and it is given by:

$$\dot{\delta}(t) = -f'_1(t) - g'_1(t) - f'_2(t) - g'_2(t) \tag{6}$$

The governing system of differential equations of the system is thus given by Eqns. (2)-(6). The initial conditions are:

$$f_1(0) = 0, \quad g_1(0) = 0, \quad f_2(0) = 0, \quad g_2(0) = 0, \quad f'_1(0) = 0, \quad g'_1(0) = -s_1 \tag{7}$$

The Hertzian stiffness is [24]:

$$K = \tfrac{4}{3}E^*\sqrt{R^*} \quad \text{with} \quad E^* = \left[(1-\nu_1^2)/E_1 + (1-\nu_2^2)/E_2\right]^{-1} \quad \text{and} \quad R^* = \sqrt{r_1r_2/(r_1+r_2)} \tag{8}$$

Various kinematic quantities may be determined using suitable derivatives of the wave equation for each rod. For instance, the speed and the strain at the midpoint of Rod 2 are:

$$\dot{u}_2(L_2/2,t) = f'_2(t - L_2/2c_2) + g'_2(t + L_2/2c_2) \qquad \varepsilon_2(L_2/2,t) = -\tfrac{1}{c_2}f'_2(t - L_2/2c_2) + \tfrac{1}{c_2}g'_2(t + L_2/2c_2) \tag{9}$$

The contact radius, $a$, and the peak contact pressure within that area, $P$, relate to the contact force as follows [24]:

$$a = \sqrt[3]{3FR^*/4E^*} \qquad P = 3F/2\pi a^2 \tag{10}$$

Solutions to the governing equations were computed using numerical integration using Simulink (Mathworks, Natick, MA). Integration was performed using the MATLAB function *ode45* [25]. The time delay was implemented using the *Transport Delay* function block. The model also computed kinematic quantities, e.g. Eq. (9).

### *2.2. Finite element model*

The 3D global model comprised the geometries of both rods. The meshes were generated using HyperMesh (Altair, Troy, MI) and consisted of hexahedral elements with a longitudinal edge length of 1.0 mm and an average cross-section edge length of 0.25 mm (Fig. 2). The material model was linear elastic to represent the steel from which the rods were made (Sec. 2.3 below). Contact constraints were implemented using a penalty algorithm.

The submodel comprised the first 14 mm (measured from the impact tips) of both rods. This cutoff length was where the subsurface stresses diminished to near-zero magnitudes at the time of peak contact force in the global results. Three mesh refinements were used to examine convergence. The element aspect ratios were approximately 1:1:1, and the average edge length was successively halved in the refinement steps: from 0.25 (*Coarse*), to 0.125 (*Mid*), to 0.0625 mm (*Fine*) (first 2 models, Fig. 2b and 2c). The Fine submodel was additionally simplified as a half-symmetry model. The physical configuration of the rods is detailed in Table 1. The impact speed, 2.197 m/s, was a value recorded during one of the experimental trials. The finite element solver Abaqus/Explicit (Abaqus v. 6.8, Simulia, Providence, RI) was used to perform the global and submodel analyses. The 8-node linear hexahedral element type with uniform strain and hourglass control (C3D8R; reduced integration element) was implemented for both rods.

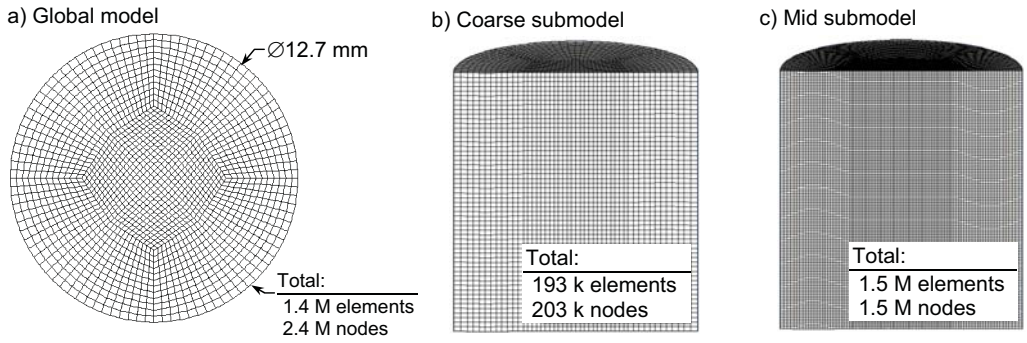


**Fig. 2** Cross sections of the FE meshes in each rod: a) Global 3D model, b) Coarse submodel, c) Mid submodel. Submodels were also cylindrical, but shown as halved to display element density

**Table 1** Physical configuration details of the finite element model

| Rod 1 length | Rod 1 $r_1$ | Rod 2 length | Rod 2 tip | Diameter | Density | Young's modulus | Poisson's ratio | Impact speed |
|---|---|---|---|---|---|---|---|---|
| 250.09 mm | 35 mm | 700.99 mm | flat | 12.70 mm | 7.803 g/cc | 204.3 GPa | 0.30 | 2.197 m/s |

### *2.3. Experimental techniques*

Both rods were made from a single lot of precision ground A2 steel drill rod. The spherical tip of Rod 1 was finished using a concave 35 mm radius cast iron lap charged with diamond particles. The flat tip of Rod 2 was lapped against a granite surface plate using fine grit silicon carbide sandpaper. (Due to the flat tip, $r_2 \to \infty$ in Eq. (8), so $R^*=r_1$.) There were three specimens of Rod 1 to allow repeat trials, and one of Rod 2. The rods were hardened and tempered to $R_c$ 60. The density was determined from the volume and the mass of one specimen; length was measured using a height gauge, diameter using a micrometer, and mass using an analytic balance. The isentropic elastic properties were measured using the impulse excitation method, ASTM

E 1876, using a Grindosonic MK5 instrument (Lemmens, Lueven, BLG). Further, the experiments were designed to maintain contact stresses within the material's linear elastic region; the criterion $P < 1.1S_y$, where $S_y$ is the uniaxial yield stress [26] was upheld by the experimental design.

The impact experiments were performed in a drop-tower test machine (Dynatup 8250, Instron, Massachusetts, USA) (schematic Fig. 3). The machine provides a motorized latch block that suspends a sled. Upon computer command, the sled may be released from the latch block into free fall guided by twin columns. To the sled was mounted a tubular fixture that suspends Rod 1; the rod was spaced off the tube's interior surface by 2 oiled o-rings. The rod's weight was suspended by a thin ring of tape whose diameter was slightly greater than the tube's ID; otherwise, Rod 1 was distally unconstrained. Rod 2 was suspended in a tubular fixture attached to the test machine base; this fixture also spaced its rod from the interior surface via oiled o-rings. Both fixtures provided approximately 6 cm of clearance behind the rods' distal ends, spaces into which the rods could slide freely after impact. Rod 2 was partly supported on its distal end by a plastic plug lightly press-fit into the tube; the plug could fall freely into the fixture's clearance space when Rod 2 was impacted. The position of the lower fixture was adjustable to permit manual alignment of the rods to achieve parallel, centric impact. The velocity of the sled was measured using an infrared sensor fixed to the drop tower that sensed passage of a flag mounted to the sled. The sensor was positioned to detect velocity at the impact position, and it was assumed that Rod 1's velocity was equal to the sled's velocity. In repeat trials, the impact speed varied slightly (±0.02 m/s) because the drop height was not precisely repeatable.

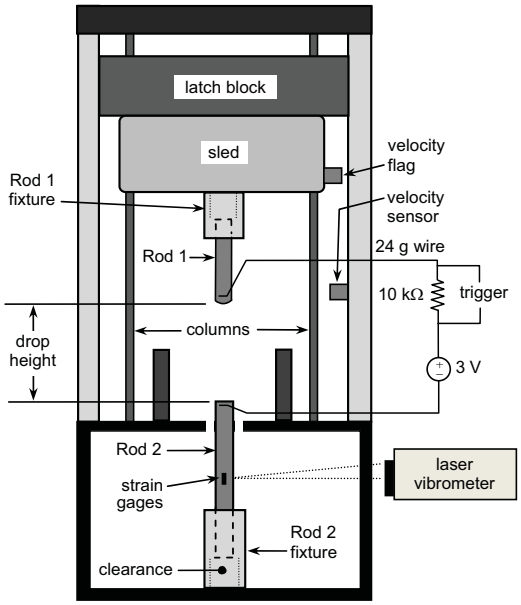


**Fig. 3** Schematic of drop tower impact test machine, with both rods, their fixtures, and trigger circuit; data acquisition and strain gage circuit not illustrated

Both rods were wired into an electrical circuit by taping to each a 24 gauge, multi-filament wire. The circuit charged Rod 1 to 3 V relative to Rod 2 using an electrical power supply. Continuity between the rods during impact created a voltage across a 10 kΩ resistor, and the voltage was used to trigger data acquisition and to measure the duration of impact.

The velocity of Rod 2 was measured at its midpoint using a 3D laser Doppler vibrometer (CLV-3D, Polytec, Germany). The vibrometer provided 3 separate, orthogonal velocity components, but only the component parallel to the rod's surface was recorded. Strain was measured at Rod 2's midpoint using two 1000Ω foil strain gages (WC-06-125AC-W/C, MicroMeasurements, Raleigh, NC, USA) oriented to measure axial strain and wired into opposing arms of a Wheatstone bridge. This circuit design doubled the bridge sensitivity compared to a circuit with only one active gage. The bridge was powered and its output signal was amplified using a high bandwidth signal conditioner (2310B, MicroMeasurements). Use of 1000Ω gages permitted maximal excitation of the bridge (15 V); so, the amplifier gain was set relatively low (~110), which

enhanced the amplifier's frequency response quality (-3 dB bandwidth of 230 kHz). The bridge and amplifier were calibrated using a shunt calibration procedure [27]. The three measurement signals were recorded at 443 kHz using a 16 bit analog-to-digital (A/D) converter (USB1604HS, Measurement Computing, Norton, MA, USA) controlled by a laptop computer. To enhance A/D accuracy, the input range of each A/D channel was programmed to limits just greater than the maximal signal value; thus, the ranges for velocity and strain were ±10 V, and ±0.5 V, respectively.

A record of the contact between the rods was made using a "fingerprinting" technique. The tip of Rod 2 was given a thin coat of bearing grease. The tip was wiped repeatedly (16 times), each time using a clean piece of paper towel, to leave a scant grease film. The tip of Rod 1 was cleaned with warm, soapy water and thoroughly rinsed and dried. During contact, a thin spot of grease transferred from Rod 2 onto Rod 1. After the test, the entire tip of Rod 1 was sprinkled with black photocopier toner powder. The powder was blown off with an aerosol duster can. A monoparticle layer of powder (the "fingerprint") remained adhered to the thin transfer layer of grease. This patch was then microscopically measured and photographed using an optical coordinate measuring machine ('CMM', Nexiv VMR 3020, Nikon, JPN). The CMM detected edge points by analyzing contrast levels in the digital image of the contact patch; 64 points were found at uniform spacing around the patch's perimeter, and these were used to compute the radius and circularity of a best-fit circle.

## 3. Results

The recorded velocity and strain at the midpoint of Rod 2 are graphed with the analytical and FEA predictions in Fig. 4. Also, the contact force from both models is superimposed with the contact trigger voltage. Non-scaled transducer voltage data from the experimental velocity and strain records (Fig. 4d) demonstrate the sufficiency of the A/D sampling rate.

Fig. 5 gives photos of the recorded contact patch on the tip of Rod 1, along with a contour plot of the contact pressure from the global FE model. The images show the circular contact patch that has been revealed by black toner powder adhering to the thin layer of grease transferred from the tip of Rod 2.

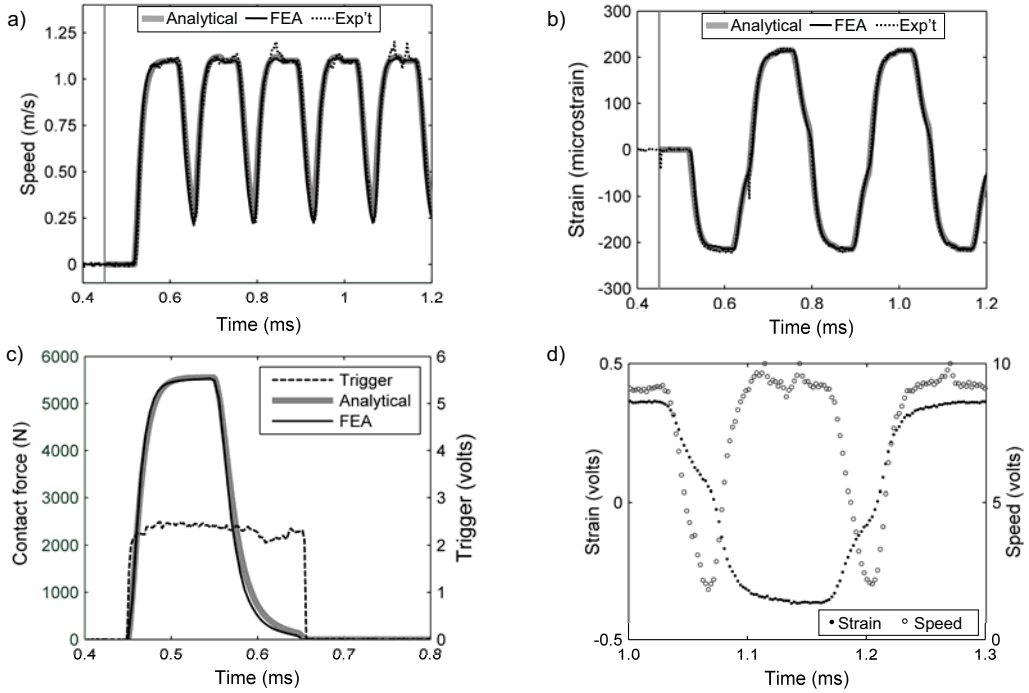


**Fig. 4** Global model results: a) Speed and b) Strain at midpoint of Rod 2, vertical line at trigger instant; c) Contact force and trigger signal; d) Samples of non-scaled voltage data points for speed and strain

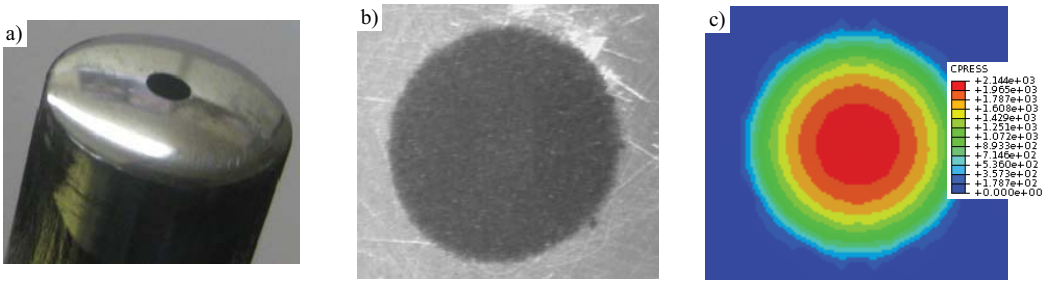


**Fig. 5** a) and b): Images of a typical contact patch, ~∅2.2 mm, recorded by the "fingerprinting" technique: a) from handheld camera, b) from optical CMM, original magnification 37×. c) Plot of contact pressure from global FEA, same scale as b)

Table 2 compares experimental to analytical model results in 2 trials of each Rod 1 specimen. The circularity (as defined by ASME Y14.5M) of the measured contact patch was 7-8% of the radius in Specimens 1 and 3, but 11-12% in Specimen 2, perhaps indicating that Specimen 2 had more form error in its spherical tip. The predicted contact radius was at most 5% less than measured. The peak speed at the midpoint of Rod 2, consisting of values ≥1.0 mm/s, was averaged over the first five plateaus in the record; the maximum difference was 2.2%. The root-mean-square (RMS) of the difference in strain was computed over the first five periods; the maximum RMS difference was 11.6 microstrain. The FEA model used the impact speed of Rod 1, Spec. 1, Trial 3. Table 3 shows the contact force and contact area for the global model and the three meshes in the submodel. The contact radius (from $r=\sqrt{(area/\pi)}$) of the Fine submodel was 1.14 mm (+2.8% vs. expt.). Fig. 6 compares the analytical and FEA results of the radial stress component, $\sigma_r$, as a function of radial coordinate. The stresses were extracted from the element integration points closest to the surface, and the analytical results were computed at identical points using formulas in [26].

**Table 2** Results from two trials of each Rod 1 specimen. 'Analytical' gives value and difference from experiment. 'RMS Δ' is the root-mean-square difference

| | | | Contact radius (mm) | | | Rod 2 midpoint | | |
|---|---|---|---|---|---|---|---|---|
| Rod 1 specimen | Trial # | Impact speed (m/s) | Experimental | | Analytical | Avg. peak speed (mm/s) | | RMS Δ strain (microstrain) |
| | | | Circularity | radius | radius | Exp't | Analytical | |
| 1 | 1 | 2.208 | 0.098 | 1.129 | 1.093 (-3.2%) | - | - | - |
| | 3 | 2.197 | 0.091 | 1.109 | 1.090 (-1.7%) | 1.114 | 1.105 (-0.8%) | 6.0 |
| 2 | 4 | 2.178 | 0.140 | 1.143 | 1.087 (-4.9%) | 1.105 | 1.095 (-0.9%) | 11.6 |
| | 5 | 1.848 | 0.117 | 1.059 | 1.029 (-2.8%) | 0.921 | 0.930 (+0.9%) | 3.4 |
| 3 | 2 | 2.166 | 0.090 | 1.120 | 1.085 (-3.2%) | 1.114 | 1.089 (-2.2%) | 7.4 |
| | 3 | 2.128 | 0.083 | 1.115 | 1.079 (-3.2%) | 1.078 | 1.070 (-0.7%) | 5.0 |
| Average Δ (absolute value) | | | | | 3.2% | - | 1.1% | 6.7 |

**Table 3** Contact force and area from the global model and three refinement levels of the submodel

| Model | Contact force (N) | Contact area ($mm^2$) |
|---|---|---|
| Global | 5,549 | 4.61 |
| Submodel-Coarse | 5,219 | 4.80 |
| Submodel-Medium | 5,368 | 4.44 |
| Submodel-Fine | 5,492 | 4.10 |
| Analytical / Experimental | 5,543 | 3.73 / 3.86 |
| Δ, Fine vs. Analytical / Exp't | -0.92% | 9.9% / 6.2% |

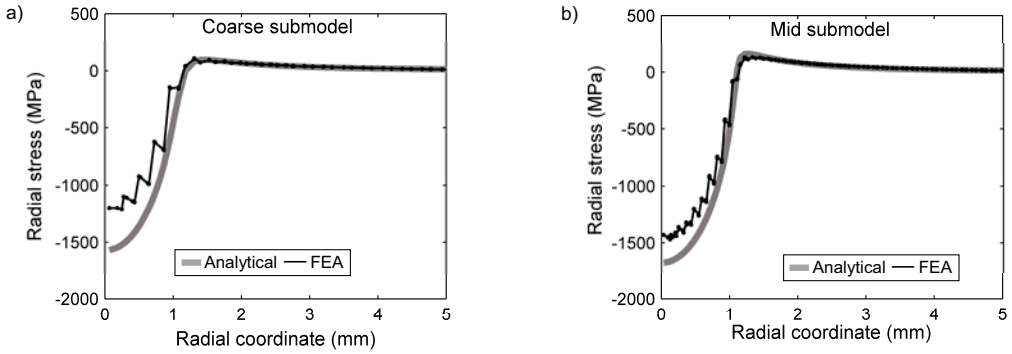


**Fig. 6** Comparison of analytical and FEA subsurface radial stress result, $\sigma_r$, from element integration points

## 4. Discussion and Conclusions

Both of the analysis models aimed to give high fidelity predictions of the global structural response. The analytical model predicted the peak Rod 2 midpoint speed within 0.7-2.2% error. Likewise, the model's strain prediction had an RMS error (over 5 periods of the vibration) of 3.4-11.6 microstrain (Table 2). Though not tabulated, the error of the model's contact duration prediction was only 1-2 μs, which is approximately the value of the sampling period. The FE model yielded similar fidelity, with the plots of its results nearly overlying those from the analytical model in Fig. 4. Similarly accurate predictions of global structural response, from both analytical and FE models, have been reported for the case of a ball striking a long rod [8,12,13], though without direct measurement of the contact duration and contact area.

The chief aim of submodelling was to provide a refined FEA focused on the contact mechanics. The peak contact radius during impact was ~1 mm, so the 0.25×0.25×1.0 mm elements in the global model were expected to yield relatively coarse resolution of the contact stress and area, since contact stress fields are quite localized [26]. The use of three submodel mesh refinements with successively halved element lengths has been previously recommended [21]. In the first submodel, the contact force differed by -330 N from the global model; the change occurred because mesh refinement reduced the stiffness of the contact surfaces while nodal displacements from the global model were applied to the submodel boundary. This effect diminished with subsequent mesh refinements, finally yielding a contact force <1% different from the analytical model and contact area 6.2% different from the experimental measurement. Ongoing work is expected to improve the FEA results in contact area and in the convergence of particular stress values; the existence of some non-convergent stress values in the half-symmetry Fine submodel has revealed that some nodes were minutely displaced from the symmetry plane.

The impact of slender rods provides a means for examining fundamental characteristics of the transient dynamics of impacting bodies. These include material property effects, speeds of wave propagation, and contact mechanics. A basic understanding of these dynamic phenomena, as they occur in the approximately 1D domain of slender rods, is an important pre-requisite to advanced impact analysis and testing involving more complicated structures. In contrast with the case of a ball–rod impact, the case of two impacting rods requires consideration of vibrations in both bodies, which may be more representative of complicated impact scenarios.

In our laboratory, this study has served as a means to verify and validate analysis and laboratory techniques for studying the transient dynamics of artificial hip joints. An artificial hip may experience small (e.g. 2 mm) separations of the ball from the socket [28], followed by rapid relocation that causes high and damaging contact stresses [29]. The hip study's objective is to identify peak contact force and stress during the rapid relocation phase, and these quantities cannot be directly measured. Therefore, they are being computed using an FE model of a corresponding dynamically actuated structure in an in-vitro relocation simulation. To validate the FE model, the structure's response to the inputs is measured using laser vibrometry and strain gages with high-bandwidth amplification, as used for the two-rod impact study. Thus, the present work has validated measurement and analysis techniques in a rudimentary test case, so that they may be applied confidently to a challenging biomedical problem. The engineering approach to impact problems in other fields may benefit similarly by preparatory testing and analysis of the low speed impact of slender rods.

## Acknowledgements

The authors are grateful to Jeff Kessler for laboratory assistance, in particular with the drop tower impact test machine.

## References

[1] Timoshenko, S.P., and Goodier, J.N., *Theory of Elasticity*, McGraw Hill, New York, 1970.
[2] Thomson, W.T., *Laplace Transformation*, Prentice Hall, Englewood Cliffs, 1960.
[3] Goldsmith, W., *Impact: The Theory and Physical Behaviour of Colliding Solids*, Edward Arnold, Ltd., London, 1960.
[4] Guo, A., and Batzer, S., "Substructure Analysis of a Flexible System Contact-Impact Event," Journal of Vibration and Acoustics, 126(1), 126-131, 2004.
[5] Marghitu, D.B., and Boghiu, D., "Spatial Impact of a Flexible Link Using a Nonlinear Contact Force," Atlanta, GA, USA, 90, 103-110, 1996
[6] Schiehlen, W., and Seifried, R., "Three Approaches for Elastodynamic Contact in Multibody Systems," Multibody System Dynamics, 12(1), 1-16, 2004.
[7] Trowbridge, D.A., et al., "Low Velocity Impact Analysis with Nastran," Computers and Structures, 40(4), 977-984, 1991.
[8] Seifried, R., and Hu, B., "Numerical and Experimental Investigation of Radial Impacts on a Half-Circular Plate," Multibody System Dynamics, 9(3), 265-81, 2003.
[9] Wei, H., and Yida, Z., "Finite Element Analysis on Collision between Two Moving Elastic Bodies at Low Velocities," Computers and Structures, 57(3), 379-82, 1995.
[10] Stoianovici, D., and Hurmuzlu, Y., "A Critical Study of the Applicability of Rigid-Body Collision Theory," Transactions of the ASME. Journal of Applied Mechanics, 63(2), 307-16, 1996.
[11] Bokor, A., and Leventhall, H.G., "The Measurement of Initial Impact Velocity and Contact Time," Journal of Physics D: Applied Physics, 4(1), 160-163, 1971.
[12] Hu, B., and Eberhard, P., "Simulation of Longitudinal Impact Waves Using Time Delayed Systems," Journal of Dynamic Systems, Measurement and Control, Transactions of the ASME, 126(3), 644-649, 2004.
[13] Hu, B., et al., "Comparison of Analytical and Experimental Results for Longitudinal Impacts on Elastic Rods," Journal of Vibration and Control, 9(1-2), 157-74, 2003.
[14] Sundin, K.G., and Ahrstrom, B.O., "Method for Investigation of Frictional Properties at Impact Loading," Journal of Sound and Vibration, 222(4), 669-77, 1999.
[15] Ueda, K., and Umeda, A., "Dynamic Response of Strain Gages up to 300 Khz," Experimental Mechanics, 38(2), 93-98, 1998.
[16] Hertz, H., "On the Contact of Rigid Elastic Solids and on Hardness", in *Miscellaneous Papers by H. Hertz*, MacMillan, London, 1882.
[17] Diaconescu, E.N., et al., "A New Experimental Technique to Measure Contact Pressure," Ponte Vedra Beach, FL, USA, 121-128, 2003
[18] Sanders, A.P., and Brannon, R.M., "Determining a Surrogate Contact Pair in a Hertzian Contact Problem," Journal of Tribology, accepted for publication
[19] Fabrikant, V.I., "A New Symbolism for Solving the Hertz Contact Problem," Quarterly Journal of Mechanics and Applied Mathematics, 58, 367-81, 2005.
[20] Sackfield, A., and Hills, D.A., "Some Useful Results in the Classical Hertz Contact Problem," Journal of Strain Analysis for Engineering Design, 18(2), 101-105, 1983.
[21] Cormier, N.G., et al., "Aggressive Submodelling of Stress Concentrations," International Journal for Numerical Methods in Engineering, 46, 889-909, 1999.
[22] Rajasekaran, R., and Nowell, D., "On the Finite Element Analysis of Contacting Bodies Using Submodelling," Journal of Strain Analysis for Engineering Design, 40, 95-106, 2005.
[23] Drumheller, D.S., *Introduction to Wave Propagation in Nonlinear Fluids and Solids*, Cambridge University Press, Cambridge, 1998.
[24] Johnson, K.L., *Contact Mechanics*, Cambridge University Press, Cambridge, 1985.
[25] Shampine, L.F., and Reichelt, M.W., "The Matlab Ode Suite," SIAM Journal on Scientific Computing, 18(1), 1, 1997.
[26] Fischer-Cripps, A.C., *Introduction to Contact Mechanics*, *Mechanical Engineering Series*, Springer-Verlag, New York, 2000.
[27] "Tech Note Tn-514: Shunt Calibration of Strain Gage Instrumentation," Vishay Micro-Measurements, 2007.
[28] Lombardi, A.V., et al., "An in Vivo Determination of Total Hip Arthroplasty Pistoning During Activity," J Arthroplasty, 15(6), 702-709, 2000.
[29] Mak, M.M., et al., "Effect of Microseparation on Contact Mechanics in Ceramic-on-Ceramic Hip Joint Replacements," Proc Inst Mech Eng [H], 216(6), 403-408, 2002.

# CHAPTER 5

# THIN HARD CREST ON THE EDGE OF CERAMIC ACETABULAR LINERS ACCELERATES WEAR IN EDGE LOADING

Reprinted with permission from Elsevier, Inc.:

Sanders, A.P., Dudhiya, P.J., and Brannon, R.M., 2012, "Thin Hard Crest on the Edge of Ceramic Acetabular Liners Accelerates Wear in Edge Loading," Journal of Arthroplasty, 27(1), pp. 150-152.

The Journal of Arthroplasty Vol. 27 No. 1 2012

Brief Communication

# Thin Hard Crest on the Edge of Ceramic Acetabular Liners Accelerates Wear in Edge Loading

Anthony P. Sanders, MS, Parth J. Dudhiya, BTech, and Rebecca M. Brannon, PhD

**Abstract:** Ceramic acetabular liners may exhibit a small, sharp crest—an artifact of discontinuous machining steps—at the junction between the concave spherical surface and the interior edge. On 3 ceramic liners, this crest was found to form a 9° to 11° deviation from tangency. Edge loading wear tests were conducted directly on this crest and on a smoother region of the edge. The crest elicited 2 to 15 times greater volumetric wear on the femoral head. The propensity of the crest to rapidly (<2000 wear cycles) cause elevated wear under low contact force (200 N) suggests that the crest artifact of prevailing machining protocols might be a root cause of stripe wear and squeaking in ceramic acetabular bearings. **Keywords:** total hip arthroplasty, edge loading, ceramic-on-ceramic, wear, surface profilometry.


The manufacturing process commonly used to machine the inner surfaces of hard acetabular liners suffers a possible shortcoming that may be a root cause of some clinically observed wear modes. The inner surfaces typically comprise a concave sphere (the *ID*) and a convex edge that forms a transition between the ID and the liner's face. Commonly, these surfaces are machined in separate, discontinuous steps, and it is difficult to merge these steps to create a smooth and tangent junction where the ID and edge meet. Consequently, the liner may exhibit a small but distinct artifact—a "crest"—where the ID and edge surfaces meet [1].

The femoral head may sublux (or "piston") out of the liner during common activities [2]. Such motion leads to edge loading, with the head bearing upon the liner's edge rather than the ID. In hip simulator wear tests, motion patterns including small subluxation to induce edge loading have elicited greater wear rates than ordinary motion patterns having only ideal, fully reduced head-liner contact [3]. The increased wear from edge loading has been explained as resulting from nonconforming contact that induces elevated contact stresses that increase surface damage [1]. Ceramic-on-ceramic hips may commence squeaking after several months of noise-free service [4]. Such squeaking has been linked to wear damage by retrieval analysis [4] and by laboratory wear tests [5].

Because edge loading in general causes elevated contact stresses, we hypothesized that edge loading on a distinct, sharp feature located upon the edge would have particularly damaging effects. This study reports the results of a wear test that isolated the damaging effects of the crest artifact by comparing the wear from small sliding across the crest with wear from small sliding across a smoother region of the liner's edge.

## Materials and Methods

Three ceramic liners were examined: a ∅36 mm alumina matrix composite (*AMC*, Biolox Delta), a ∅36 mm aluminum oxide ($Al_2O_3$, Biolox Forte), and a ∅28 mm $Al_2O_3$ (all: Ceramtec, Germany). On each, the crest was palpable by dragging a fingernail across the ID-edge junction or by lightly rubbing a femoral head across the same. Each liner's crest was measured with a stylus profilometer (SJ401; Mitutoyo, Kawasaki, Japan) by tracing a 2.5-mm long profile across the ID edge junction.

The wear test was designed to create edge loading with short distance sliding contact. The tests were conducted using custom fixtures in a fatigue test machine. The fixtures included a horizontal spring that pressed the equator of the femoral head into the liner's edge with a

*From the Department of Mechanical Engineering, University of Utah, Salt Lake City, Utah.*
Submitted May 26, 2011; accepted August 14, 2011.
The Conflict of Interest statement associated with this article can be found at doi:10.1016/j.arth.2011.08.004.
Reprint requests: Anthony P. Sanders, MS, Department of Mechanical Engineering, University of Utah, 50 S. Central Campus Dr., Salt Lake City, UT 84112.

0883-5403/2701-0024$36.00/0
doi:10.1016/j.arth.2011.08.012

200 N force. For a crest trial, the initial head liner contact point was directly on the crest, and for a smooth trial, the contact point was on a smooth portion of the edge ~1 mm above the crest. Each liner was paired with a head of the same size and material. The liner was reciprocated vertically (ie, along the test machine's axis) by ±0.5 mm at 1 Hz for 2000 cycles, whereas the head could pivot on a swing arm to maintain edge contact. The 2000 cycle end point was sufficient to elicit measurable roughening on the femoral head. The contact point was lubricated by a drip feed of 50% diluted bovine serum. The dimensions of the femoral head wear scar were measured using a stereomicroscope. The volumetric wear was quantified using an optical surface profilometer (NewView; Zygo Corp, Middlefield, Conn); further details are given in the following section.

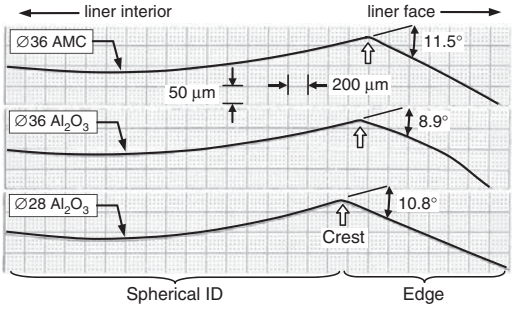


**Fig. 1.** Profilometer traces encompassing each liner's ID and edge, with the crest at the junction. The profile height is exaggerated by the differing horizontal and vertical scales; the stated angles are suitably scaled values.

**Table 1.** Femoral Head Wear Scar Measurements

| | Volume ($mm^3$) | | Height × Width (mm) | |
|---|---|---|---|---|
| Bearing | Smooth | Crest | Smooth | Crest |
| ∅36 AMC | $0.087 \times 10^{-3}$ | $1.362 \times 10^{-3}$ | 0.90 × 1.79 | 1.11 × 4.17 |
| ∅36 $Al_2O_3$ | $0.235 \times 10^{-3}$ | $0.527 \times 10^{-3}$ | 0.87 × 1.43 | 1.05 × 2.71 |
| ∅28 $Al_2O_3$ | $0.338 \times 10^{-3}$ | $5.080 \times 10^{-3}$ | 0.90 × 1.41 | 1.00 × 3.70 |

## Results

The stylus profilometer traces (Fig. 1) show the crest on each liner. The angle at the crest was measured graphically and scaled appropriately to quantify the crest's "sharpness." Table 1 provides the dimensional and volumetric wear results. Each trial produced a plainly visible wear scar on the femoral head. The optical surface profile scans of the smooth trial wear scars were 1.5 × 1.5 mm; 3.0 × 1.5 mm scans were used for the crest trial scars, yet even these wider scans left some of the scar width outside of the scanned area (cf. Table 1). Fig. 2 compares these measurements from the ∅28 $Al_2O_3$ wear scars. These 3-dimensional surface models come from subtracting the original scanned surface data from a sphere best fit to the unworn portion. In the resulting data, the unworn portion appears approximately as a plane, and the worn portion appears as surfaces in relief. The volumetric wear was numerically computed as the volume contained between the relief surfaces and the mean plane through the unworn portion.

## Discussion

If the ID-edge junction were ideally smooth and tangent (ie, without a crest), then head liner contact at the crest location would be more conforming than at the smooth location; hence, the test would be expected to cause lower contact stress and less wear at the crest location. Because the opposite occurred—the crest trials produced 2 to 15 times greater wear volume than the smooth trials—it appears that the crest itself was responsible for the increased wear.

The initial contact positions in the smooth and crest trials were associated with head-liner separations of 4.7 and 2.0 mm, respectively, for the ∅36 pairs. Although 4.7 mm is beyond the typical range of in vivo measured subluxations, 2.0 mm is within the reported range. Subluxation as small as 0.08 mm can instigate edge loading [6]. Because the crest is the first edge feature that a subluxing head would contact beyond the ID, in vivo subluxation in the range 0.08 to 2 mm would likely result in crest loading such as that examined in this study.

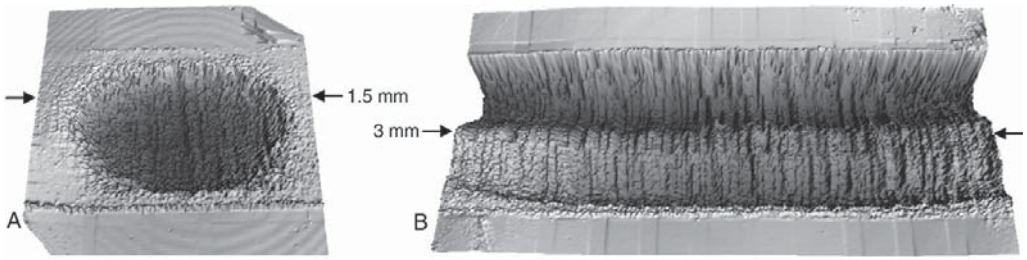


**Fig. 2.** Worn surfaces on ∅28 $Al_2O_3$ head: smooth trial (A) and crest trial (B). The spherical form has been removed, so the wear volume appears as the region in relief to a plane. The depth scale is magnified to emphasize the surface texture; actual peak depths are approximately 1.3 $\mu$m in (A) and 3.5 µm in (B).

Little is yet known about the magnitude of head-liner contact forces during subluxation events. Even so, the 200 N contact force used in this study appears to be low compared with that applied (500 N) in microlateralization simulator tests [7]. The onset of crest-incited wear in less than 2000 cycles in the present study has implications for longer term damage. Early postoperative generation of ceramic wear debris from crest loading damage could lead to third-body wear conditions at the head-ID interface. This may partly explain a 1- to 2-year postoperative onset of ceramic hip squeaking [4].

Because edge loading can occur even with minute subluxation, the liner's bearing surface should be regarded holistically as including all of the inner surfaces. To enhance wear resistance, manufacturers should implement smooth, tangent junctions between all adjoining geometric segments of this whole bearing surface. Surgeons should anticipate that edge loading may occur and should implement techniques such as proper joint tensioning and prosthesis alignment to minimize its occurrence and magnitude.

## Acknowledgments

This work was supported by Award #R21AR056374 from the National Institute of Arthritis and Musculoskeletal and Skin Diseases. The authors thank Jeff Kessler for laboratory assistance and Kirk Croxford for fixture machining.

## References

1. Walter WL, Insley GM, Walter WK, et al. Edge loading in third generation alumina ceramic-on-ceramic bearings: stripe wear. J Arthroplasty 2004;19:402.
2. Lombardi AV, Mallory TH, Dennis DA, et al. An in vivo determination of total hip arthroplasty pistoning during activity. J Arthroplasty 2000;15:702.
3. Stewart TD, Tipper JL, Insley G, et al. Long-term wear of ceramic matrix composite materials for hip prostheses under severe swing phase microseparation. J Biomed Mater Res B Appl Biomater 2003;66:567.
4. Restrepo C, Parvizi J, Kurtz SM, et al. The noisy ceramic hip: is component malpositioning the cause? J Arthroplasty 2008;23:643.
5. Taylor S, Manley MT, Sutton K. The role of stripe wear in causing acoustic emissions from alumina ceramic-on-ceramic bearings. J Arthroplasty 2007;22:47.
6. Mak MM, Besong AA, Jin ZM, et al. Effect of microseparation on contact mechanics in ceramic-on-ceramic hip joint replacements. Proc Inst Mech Eng [H] 2002;216:403.
7. Sariali E, Stewart T, Jin Z, et al. Three-dimensional modeling of in vitro hip kinematics under micro-separation regime for ceramic on ceramic total hip prosthesis: an analysis of vibration and noise. J Biomech 2010;43:326.

CHAPTER 6

# CONCOMITANT EVOLUTION OF WEAR AND SQUEAKING IN DUAL-SEVERITY, LUBRICATED WEAR TESTING OF CERAMIC-ON-CERAMIC HIP PROSTHESES

Reprinted with permission from Wiley Periodicals, Inc.:

Sanders, A., Tibbitts, I. and Brannon, R., 2012, "Concomitant Evolution of Wear and Squeaking in Dual-Severity Lubricated Wear Testing of Ceramic-on-Ceramic Hip Prostheses," Journal of Orthopaedic Research, 30(9), pp. 1377-1383.

# Concomitant Evolution of Wear and Squeaking in Dual-Severity, Lubricated Wear Testing of Ceramic-on-Ceramic Hip Prostheses

**Anthony Sanders,[1,2] Ira Tibbitts,[1] Rebecca Brannon[1]**

[1]Department of Mechanical Engineering, University of Utah, Salt Lake City, Utah 84112, [2]Ortho Development Corp., 12187 S. Business Park Dr., Draper, Utah 84020

*Received 1 December 2011; accepted 9 January 2012*
*Published online in Wiley Online Library (wileyonlinelibrary.com). DOI 10.1002/jor.22080*

**ABSTRACT:** Ceramic-on-ceramic (CoC) hip bearings were tested in short-term wear tests with a systematically varied contact force. Continuous vibration and intermittent surface roughness measurements were obtained to elucidate potential causes of in vivo hip joint squeaking. The three-phase test comprised alternating cycles of edge loading (EL) and concentric articulation (CA), always using ample serum lubricant. A 50,000-cycle wear trial in which the contact force during CA was distant from the head's wear patch yielded no squeaking and practically no liner roughening. In 10-cycle trials of an edge-worn head coupled with a pristine liner, the contact force was varied in magnitude and point of application; immediate, recurrent squeaking occurred only when the contact force exceeded a critical threshold value and was centered upon the head's wear patch. In a 27,000-cycle wear trial with the contact force applied near the margin of the head's wear patch, recurrent squeaking emerged progressively as the liner's inner surface was roughened via its articulation with the worn portion of the head. The results reveal key conditions that yield recurrent squeaking in vitro in various scenarios without resorting to implausible dry conditions. A fundamental theory explains that hip squeaking is induced by myriad stress waves emanating from asperity collisions; yet, the root cause is edge loading. © 2012 Orthopaedic Research Society. Published by Wiley Periodicals, Inc. J Orthop Res

**Keywords:** hip prosthesis; ceramic-on-ceramic; wear; noise; squeaking

Ceramic-on-ceramic (CoC) hip prosthesis bearings exhibit superior wear properties when the in vivo conditions are ideal, as when the bearings articulate concentrically.[1] However, some CoC bearings retrieved following in vivo use have exhibited a wear pattern called *stripe wear* for its elongate shape on the femoral head.[2] This pattern is caused by edge loading (EL), but not all such wear is stripe-shaped, and so a more apt term that relates to the root cause is *edge-loading wear*. Edge-loading wear has been produced in a few laboratories by modifying standard hip simulator cyclic motion profiles.[3,4] The modified profiles induce small separation and EL between the head and liner, mimicking the in vivo behavior of a lax joint.[5,6] Studies with these conditions have replicated clinically observed edge-loading wear after several million cycles. Yet, such studies have not produced the extensive wear on the bearing surface exhibited by some retrievals,[7,8] nor have they produced the squeaking noises experienced by some patients with CoC hips.[8] This contradicts hypotheses pointing to edge-loading wear as an important cause of squeaking.[9,10] The contradiction raises questions about the relationship of edge-loading wear to liner ID wear and squeaking and about the efficacy of current test methods.

Given the potential for head-liner separations to occur in vivo,[6] hip bearings have two distinct interfaces. The intended spherical interface between the head and liner has low contact stresses[11] and can be protected from wear by fluid film lubrication.[12] The second interface, between the head and the liner's edge, experiences more severe loading conditions. There, the low conformity of the bearing surfaces leads to extreme contact stresses[13–15] and poor lubrication conditions. Wear from this second interface has been implicated to contribute to CoC hip squeaking.[8,10,16] However, just one in vitro study to date has reproduced squeaking under lubricated, concentric articulation (CA) with an edge-worn head, and only under peak loading aligned with the wear patch.[9] Further experiments are needed to validate hypotheses about a link between wear at the severe interface and squeaking that can originate at the mild spherical interface under a variety of in vivo loading conditions.[17] Some in vitro studies have described squeaking as a discrete, binary variable[9,18]; this is a limiting simplification, and continuous diagnostics are needed to uncover the problem's root causes.

We regarded the CoC hip as a dual-interface, dual-severity bearing and examined the progressive effects of wear at both interfaces in a laboratory hip simulator. We hypothesized that wear would develop progressively, occurring first on the surfaces in the severe interface, and later emerging on the liner ID. We also hypothesized that squeaking would emerge progressively from articulation at the mild interface, dependent on the roughening of both bearing surfaces. Tests were performed on commercial $Al_2O_3$ bearings with ample lubrication in a custom-built, dual-severity wear apparatus that provided both EL and CA. To assess wear, the bearing surfaces' roughnesses were measured intermittently in multiple locations. To assess squeaking, component vibrations were continuously recorded. The observed concomitant progression of surface roughness and squeaking-related vibrations

Additional Supporting Information may be found in the online version of this article.

*Correspondence to*: Anthony Sanders (T: 801-553-9991; F: 801-619-8936; E-mail: tsanders@odev.com)

elucidates the fundamental causes of squeaking, and it supports theories that edge-loading wear induces, or is at least an integral part of, a chain of events that causes squeaking in vivo.

## METHODS AND MATERIALS

### Test Design

A schematic of the test design is shown in Figure 1. The femoral head is mounted by repeated impaction onto a 12/14 taper on a stainless steel swing arm that can pivot on fixed axis A-A. A liner oriented at a selectable, fixed abduction angle θ can be translated vertically (y-axis) by the test machine's actuator and rotated about the horizontal axis through its center (axis B-B) by a step motor. A spring parallel to B-B applies a force $S$ to the lower end of the swing arm. Further, the dual-severity articulation modes are detailed as follows:

Concentric articulation (CA, the mild condition, Fig. 1a) consists of liner reciprocation about axis B-B with the head fully reduced in the liner. A vertical actuator force on the liner and the spring force $S$ on the swing arm induce contact force $Q$ on the head and reaction force $R$ on swing arm axis A-A. $Q$ forms angle α with the vertical, and the vertical component of $R$ ($R_y$) is the axial force registered by the test machine's load cell.

Edge loading (EL, the severe condition, Fig. 1b) consists of subluxation and reduction motion where the head slides across the liner's edge. In subluxation, the liner is lowered distance $y$, and $S$ pulls the head across the liner's edge; simultaneously, the center-point of head-liner contact traverses angle τ on the head's surface. In reduction, the liner is raised $y$, forcing the head back into the liner. Repetition of EL causes edge-loading wear on the head, spanning τ as illustrated.

The adjustability of $Q$ (using $S$ and $R_y$) and θ is a key feature. Adjustment of these variables enabled examination of the hypothesis that CA can induce liner ID wear where the edge-worn portion of the head articulates with the ID of the liner; such wear is labeled as *liner ID wear* in Figure 1a. As detailed below, tests that varied θ and $Q$ (both its magnitude $|Q|$ and orientation α) revealed that ID wear depends on both θ and $Q$ and that squeaking can occur most readily after ID roughening surpasses a critical threshold.

### Custom Test Apparatus

A custom, adjustable apparatus was built to implement the dual-severity test design. Detailed schematics are provided in Supp. Figure S1. A few key details are labeled in Figure 2. The liner orientation is adjustable to simulate abduction angles of 45° or 60°. The liner is rotated using a NEMA-23 step motor (Powermax II, Pacific Scientific, Rockford, IL) equipped with a 10:1 reduction gearhead. The spring is connected to the swing arm 134 mm below the swing arm's pivot axis. The spring force is measured using an in-line load cell. The entire apparatus (except swing arm and head) is attached to the vertically oriented, bottom-mounted actuator of a servohydraulic test frame (MTS, Eden Prairie, MN). The swing arm is attached via an adapter to the test frame's top-mounted load cell. The test frame's controller synchronizes the motions of the actuator and the step motor to effect both articulation modes as directed by a custom program. During operation, the bearings were continuously lubricated with diluted bovine serum using a gravity-fed drip system, as detailed below.

### Measurement Protocols

Bearing surface textures were measured at intervals during the tests to quantify the progression of surface damage

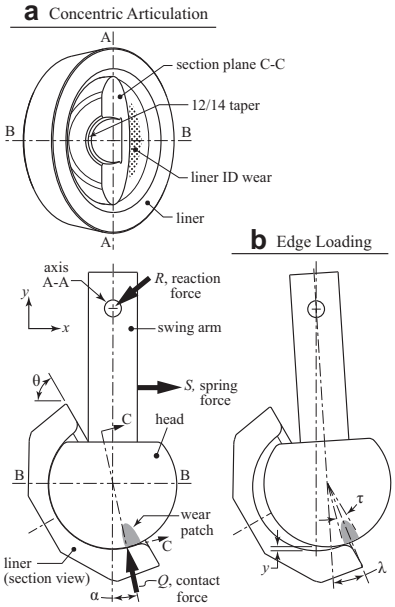


**Figure 1.** Schematic of dual-severity test design. a: Concentric articulation; top view hides swing arm and includes head section C-C to reveal liner ID wear. b: Edge loading.

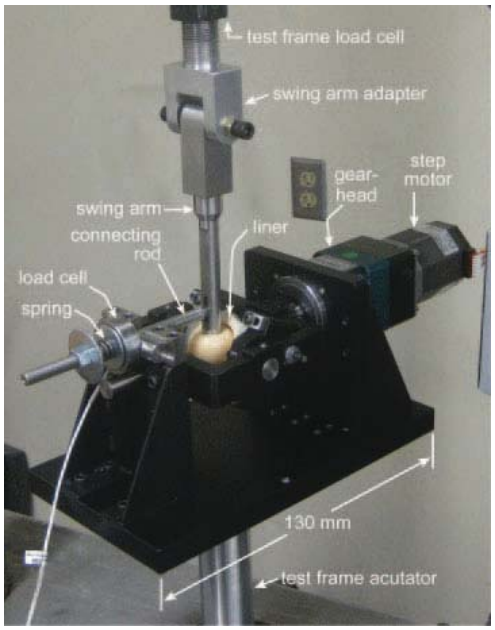


**Figure 2.** Dual-severity test apparatus.

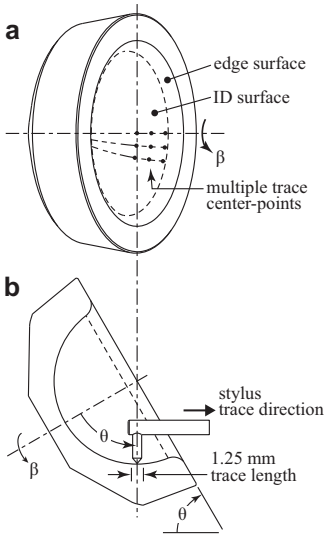


**Figure 3.** Liner ID surface texture measurement approach. a: Matrix of measurement locations. b: Sectioned liner and profilometer stylus.

(Fig. 3). The liner was removed from the apparatus and held within an adjustable angle vise. The 2 μm radius tip of a stylus profilometer (SJ-400, Mitutoyo, Japan) was positioned within the liner interior such that the stylus measured along a meridional arc segment symmetrically disposed about the nadir (the arc's lowest point). Measurements were taken at multiple ID locations; the liner was rotated to angles θ and β to position predefined measurement locations (Fig. 3a) beneath the stylus. All profilometer measurements had an evaluation length of 1.25 mm and a cutoff length of 0.25 mm. Edge-loading wear on the head was also quantified by measuring the length and width of the visually matte wear patch with a digital caliper.

Squeaking was quantified using vibration measurements. A laser Doppler vibrometer (CLV-3D, Polytec, Germany) was focused on a midpoint of the swing arm. The vibrometer's voltage output was streamed via a data acquisition board to computer memory at 50 kHz. Afterwards, the data were scaled to velocity values and divided into separate segments for each half-cycle of liner rotation. The power spectrum of each segment was computed using a fast-Fourier-transform (FFT) technique, and the power at particular frequencies was recorded. The frequencies were those that exhibited dramatically increased power concomitant with instances of audible squeaking. The tests were human-attended, and audible squeaking was noted as it occurred to further corroborate the signals that are interpreted as squeaking in the vibration data.

### Uniform Test Conditions

Throughout the study, the bearings were Ø36 mm alumina implants (Biolox Forte, Ceramtec, Germany). The lubricant was bovine serum acquired with a protein concentration of 30 g/L (Hyclone, Logan, UT) and further diluted with deionized water to 17.5 g/L. The lubricant was gravity-fed to the bearing couple at ~10 drops/min. The liner rotation (about axis B-B) had a peak-to-peak amplitude of 50° at 100°/s. The liner abduction angle (θ) was 60° except in certain trials of Test DS2 described below.

### Tests

Two bearing pairs were tested under varied conditions:

1. *Dual-Severity Test 1* (DS1): This test comprised the following 2 phases:
   a) The first 2500 cycles of this test alternated 1 cycle of EL with 5 cycles of CA. The spring was preloaded to *S=75* N. During EL, in the subluxation half-cycle, the liner was lowered by $y = 0.9$ mm in 0.3 s, and the head-liner contact center-point slid onto the liner's edge as illustrated in Figure 1b. In the reduction half-cycle, the liner was raised 0.9 mm in 0.5 s. During CA, the axial force was $R_y = 2750$ N.
   b) Next, the test alternated between 10 cycles of CA and 1 cycle of EL, to 50 k cycles of CA.
2. *Dual-Severity Test 2* (DS2): This test comprised 4 phases, detailed as follows:
   a) *Initial EL:* The head was first worn over 5000 cycles of EL. The spring preload was $S = 75$ N. For subluxation, the liner was lowered $y = 1.3$ mm in 0.5 s. During reduction, the liner was returned $y = 1.3$ mm in 0.9 s, while it was twice rotated ±15° as a means to lengthen the expected wear patch. Supp. Movie SI demonstrates this test activity.
   b) *Varied θ and Q* (VQ): Twelve 10-cycle trials of CA were performed with varied $\theta$ and $Q$. Changing $Q$ varied the contact pressure and the placement of the contact force with respect to the head's wear patch; changing $\theta$ altered the area of the head covered by the liner. Three contact force angles $\alpha$ were used: $\alpha = 0°$, 7.5°, and 15°; at 15°, $Q$ was directed into the center of the head's wear patch. Two force magnitudes, $|Q| = 500$ and 1000 N, were used at each $\alpha$. Trials were performed at $\theta$= 45° and 60°. Vibrations were measured.
   c) *Dual-Severity* (DS): 25 k cycles of CA were performed, alternating 250 cycles of CA with 10 cycles of EL. The test began with $|Q|$=400 N directed into the head's wear patch ($\alpha = 15°$). Squeaking arose early (3000 cycles of CA); so, $Q$ was changed to eliminate the squeaking: $\alpha$ was reduced to 8°, and $|Q|$ was increased to 1000 N. Vibrations were measured during CA.
   d) *Final CA:* 2500 cycles of CA were performed with no EL. Vibrations were measured.

## RESULTS

### Dual-Severity Test 1

Test DS1 produced an elongate wear patch on the head, little roughening of the liner, and no squeaking. The wear patch dimensions are graphed in Figure 4 along with the roughness at the patch's center. The patch was centered 14.5° from the pole (per Fig. 1b, $\lambda = 14.5°$). Photos showing the wear patch's growth are in Supp. Figure S2. The head's roughness across the pole was essentially unchanged. The liner was measured at nine positions on the ID, and all showed essentially no roughening—the greatest roughness was 8 nm $R_a$ (roughness average).

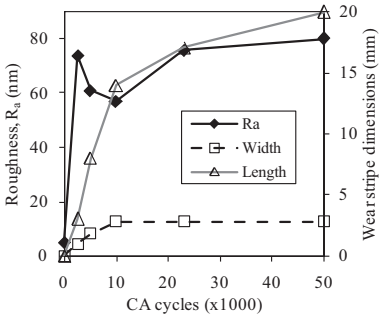


**Figure 4.** Test DS1: Femoral head's wear patch roughness, width, and length.

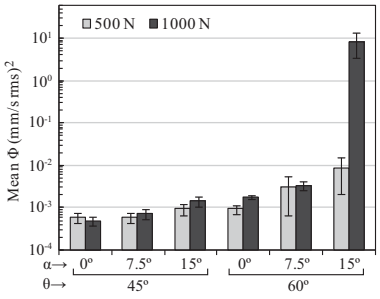


**Figure 6.** Mean squeaking power (Φ) from 10-cycle trials in VQ phase. Error bars are ±1 std. dev., except 60°/15° where they are ±½ std. dev.

### Dual-Severity Test 2

The *Initial EL* phase produced a 3 × 17 mm head wear patch, centered at $\lambda = 15^\circ$ from the pole. Its roughness, measured across its narrow dimension at the center, was 87 nm $R_a$. A photo of the wear patch is in Supp. Figure S3.

The VQ trials produced audible squeaking only for $\theta = 60^\circ$ and only when the contact force was directed into the head's wear patch ($\alpha = 15^\circ$), at the highest load ($|Q| = 1{,}000$ N). Figure 5 compares the vibration signals from three different half-cycles of CA, with constant $|Q|$ but varied $\theta$ and $\alpha$. To quantify the squeaking, the signal power surrounding distinct squeaking-related peak frequencies was isolated. At each such frequency, the power was summed from the FFT power spectrum over a span of 12 Hz centered on the peak frequency. Summing the power in all such frequencies yielded the *squeaking power*, denoted as $\Phi_i$, where $i$ is the count of CA half-cycles. $\Phi_i$ was computed for each half-cycle, rather than each cycle, because the bearings often made different sounds in opposite directions of liner rotation. Figure 6 compares the mean value of Φ across the 12 trials in this phase. Only for $\theta = 60^\circ$, with $\alpha = 7.5^\circ$ and $15^\circ$, was the power in the squeaking-related frequencies noticeably greater than the signal's noise level. Supp. Figure S4 graphs $\Phi_i$ for the 12 trials in this phase.

The *Dual-Severity* phase produced roughening of the liner ID and intermittent bouts of squeaking. The liner surface texture was measured at 18 locations given by the combinations of $\theta = 60$, 66, 70, 74, 78, and $82^\circ$ with $\beta = 0$, 25, and $-25^\circ$; Supp. Table S1 gives the complete results with four measures of roughness. Figure 7 compares the ID roughness at four locations having $\beta = 0^\circ$, along with the squeaking power ($\Phi_i$). $\Phi_i$ rapidly increased during the first 3,500 cycles with $|Q| = 400$ N and $\alpha = 15^\circ$. Squeaking that was audible from a distance >1 meter was generally associated with $\Phi > 1$ (mm/s rms)$^2$. When conditions were changed to $|Q| = 1{,}000$ N with $\alpha = 8^\circ$, squeaking ceased, and then $\Phi_i$ trended slowly greater until squeaking became quite common after about 21 k cycles. $\Phi_i$ often increased dramatically during a 250-cycle interval of CA, yielding the relatively vertical columns of data points in Figure 7. On some occasions, though, $\Phi_i$ decreased throughout a CA interval.

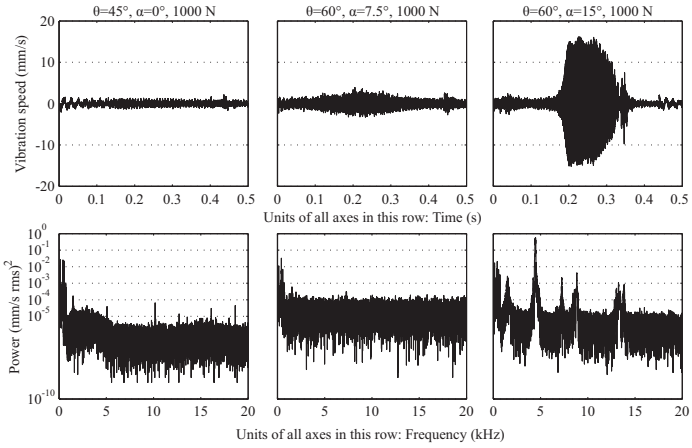


**Figure 5.** Vibrations during three VQ trials. Top row: Vibration signals; Bottom row: Respective power spectra. Left: Minimal vibration; Middle: Increased vibration without squeak; Right: Audible squeak.

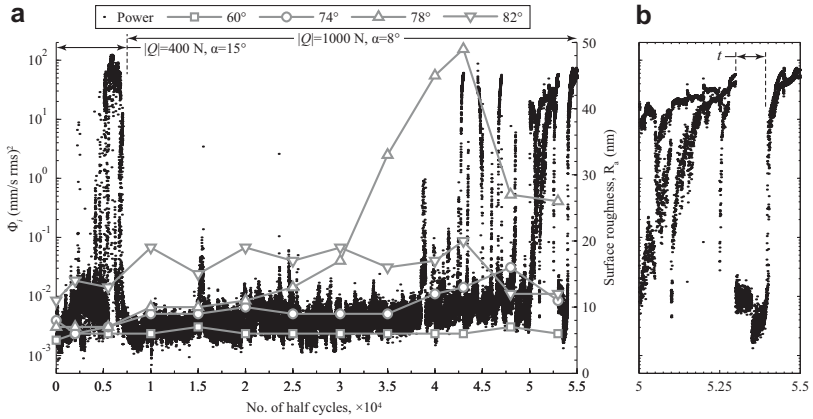


**Figure 7.** Squeaking power ($\Phi_i$) and liner surface roughness in Test DS2. a: DS and *Final CA* phases; line plots show liner ID roughness at four values of $\theta$, all with $\beta = 0^\circ$. b: Focus on *Final CA* phase; $t$ highlights an interval in which squeaking did not occur after temporary bearing removal.

The *Final CA* phase yielded audible squeaking with great regularity; Supp. Movie S2 demonstrates squeaking in this phase. An exception was during an ~500-cycle interval ($t$ in Fig. 7b) after the bearings had been temporarily removed for surface measurement. Figure 8 shows photos of the bearings' roughened areas after test completion.

## DISCUSSION

Our results demonstrate that squeaking in CoC hip bearings can emerge at different rates and in different ways, depending on the contact force $Q$ and the liner abduction angle $\theta$. In the short-cycle VQ trials, squeaking occurred only when $|Q|$ was maximum and α was aligned directly with the head's wear patch. Yet, the other VQ trials exhibited increasing vibration energy (Figs. 5 and 6) as $|Q|$ was increased and α was aligned closer to the wear patch. The minimal vibrations seen with $\theta = 45^\circ$ can be attributed to improved fluid film lubrication when the liner covered more of the head. In Test DS2, recurrent squeaking emerged in a short interval when $Q$ was aligned with the center of the head's wear patch, even though $|Q|$ was low, 400 N. The liner ID was roughened little during this interval. In the second interval of Test DS2, $Q$ was aligned more distant from the head's wear patch, and recurrent squeaking emerged much later, after the liner ID was substantially roughened. $Q$ was placed most distant from the wear patch ($\alpha = 1^\circ$) in Test DS1, and squeaking never emerged, even though $|Q|$ was much greater, 2,750 N.

The results from an intermediate scenario, i.e., the second phase of Test DS2 with $Q$ indirectly aligned with the head's wear patch, provide the best foundation for an explanation of squeaking emergence in vivo, where loading varies widely. In this theory, squeaking emerges as a chain of events induces increasing vibration energy in a component of the prosthesis system. The evolution of a squeaking CoC hip can be described using the relative time sequence below. (Italicized times follow labels in Figure 9; they are illustrative only and are scaled from the time span of months-to-years during which squeaking typically emerges in vivo.)

*0:00*: New, pristine bearing surfaces articulate concentrically, and fluid film lubrication prevents contact of asperities. Component vibration is minimal, and no noise is heard.

Interval *0:00–1:00*: Small head-liner separations result in EL with high contact stresses that elicit edge-loading wear on the head. Patient may perceive clicking, but not squeaking.

*1:00*: Asperities within the head's wear patch are large and granular; some penetrate the lubricant film. Asperity contact with the liner ID causes high magnitude micro-scale contact stress, even though macro-scale contact pressure is low. Asperity contacts radiate weak stress waves. Component vibrations increase modestly.

Interval *1:00–8:00*: Over a long time, numerous cycles of CA occur with occasional EL. The head wear patch grows. Asperity contacts with liner ID create contact fatigue damage.

*8:00*: High-stress asperity contacts may have caused plastic changes such as twinning in surface grains, leading to intergranular cracking.[19] A few grains have spalled from the liner; the voids experience energetic collisions with head asperities, sending out strong stress waves. Stress waves traverse intact grain boundaries but reflect from cracked boundaries. The liner becomes rougher. Component vibrations become stronger and more variable.

Interval *8:00–11:59*: Liner ID surpasses a contact fatigue threshold, and wear rapidly becomes severe, with extensive grain pullout and rapidly increasing roughness.[19] Occasional squeaks occur.

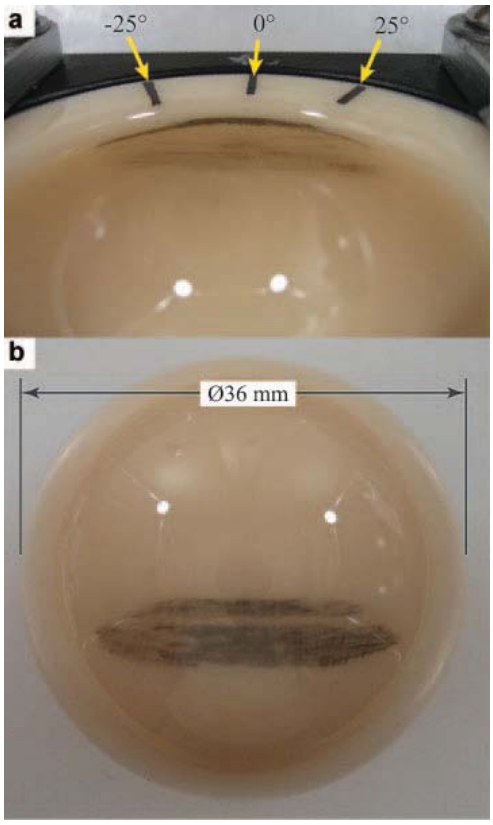


**Figure 8.** Worn areas of (a) liner and (b) head revealed by rubbing with graphite pencil. Labeled marks on the liner show the angles β where surface texture measurements were made.

*11:59*: Numerous large, granular asperities from both bearing surfaces penetrate the fluid film and collide during CA, inducing strong stress waves. Intergranular cracking continues, yet many colliding asperities are peaks of firmly anchored grains. Vibration energy reaches a critical level that induces component resonance. Patient suffers persistent squeaking.

This theory of squeaking evolution is supported by test observations and scientific reports. CA between pristine surfaces occurred in the VQ trials with $\alpha = 0^\circ$, and Figures 5 and 6 demonstrate the minimal vibration power. Test DS1 showed that edge-loading wear occurs much more rapidly than ID wear. Several reports show the granular microstructure of wear patches.[2,20] Figure 7 shows the trend of increasing vibration power concomitant with increasing surface roughness. Cho et al.[19] reported that in sliding wear, alumina exhibits a sharp mild-to-severe wear rate transition, after which its bearing surface displays intergranular fracture and grain pullout. In Test DS2, such a transition occurred between 20 k and 21.5 k cycles, and it greatly widened the visibly matte, roughened area of the liner ID. At 20 k cycles, the matte area spanned $-15^\circ < \beta < 15^\circ$, and by 21.5 k cycles, it spanned $-30^\circ < \beta < 30^\circ$. Figure 7 corroborates sudden increases in the rate of roughening. Figure 7 also demonstrates that powerful squeaking can emerge first on an infrequent basis and later become routine.

An unexpected outcome in Test DS2, that squeaking became continual after cessation of EL (*Final CA* phase), helps explain the relationship between asperities and vibrations. When asperities collide, some of the bearings' kinetic energy is transferred to the components in the form of minute stress waves that propagate throughout the components. The interaction of these waves with a component's surface causes minute elastic displacements detectable with the vibrometer. The intermittent EL cycles induced severe contact stresses that created a thin, freshly damaged layer in which grains were poorly bound to the matrix. In subsequent CA, such poorly adhered grains did not effectively transmit the energy of asperity collisions into stress waves (vibrations); instead, the loosely held grains gained kinetic energy as they were pulled from the surface, becoming mobile particles. But once EL was halted, the freshly damaged layer was quickly worn away. Then, during the *Final CA* phase, asperity collisions occurred between surface grains well-adhered to their respective substrates; so, the energy of these collisions could readily propagate across intact

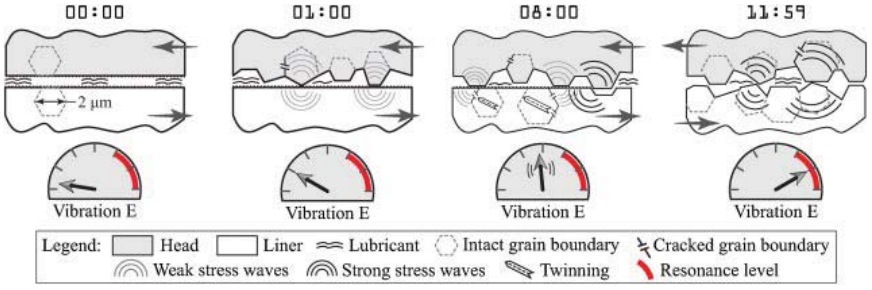


**Figure 9.** Diagram for the theory of the evolution of squeaking in CoC hip joints. Time labels and 'Vibration E(nergy)' meters are illustrative, to provide simple relative values.

grain boundaries as stress waves, which consistently raised the component vibration energy to a critical, resonance-inducing level. This phenomenon also occurred without EL, around interval *t* during *Final CA* (Fig. 7b).

Many authors have proposed that CoC squeaking in vivo is caused in part by reduced lubrication,[18,20–22] some even proposing dry contact. Several in vitro studies have tested CoC hips for squeaking with no lubrication, and most have reported better success producing squeaking with dry conditions than with lubrication.[9,18,23,24] Our study used only lubricated conditions, and the results corroborate the explanation by Laurent et al.[20] that the fluid film is 'disrupted' by increased surface roughness; that is, the fluid film is penetrated by large asperities. Interpreting 'disruption' in the more extreme sense of an absence of lubrication in vivo, leading to the implausible scenario of a dry CoC interface, is probably overreaching, and as our study shows, an unnecessary component of a theory of squeaking in vivo.

All known previous studies examining squeaking in vitro have used a liner with an unworn ID. One of these[9] produced squeaking in a scenario similar to the sole VQ trial that produced squeaking; namely, the contact force was aligned directly with the head's wear patch. Liners retrieved from squeaking CoC hips have displayed ID wear similar to that from Test DS2.[7,8]

Taken together, prior observations and our results suggest that in future research of CoC hip prostheses, particularly in multi-axis simulators with flexible and programmable inputs, wear testing protocols should include joint forces directed close to or aligned with a femoral head wear patch elicited via edge loading. An in vitro model of in vivo squeaking evolution should include the following: (1) Lubrication, (2) Edge loading, and (3) Concentric articulation wherein the contact force can cause wear asperities formed by edge loading to penetrate the fluid film. Since edge loading is the first step in a chain of events that leads to CoC wear and squeaking, future research should also be directed toward designs, materials, or techniques that will reduce its severe effects.

## ACKNOWLEDGMENTS

This work was supported by Award #R21AR056374 from the NIH/NIAMS.

## REFERENCES

1. Clarke IC, Good V, Williams P, et al. 2000. Ultra-low wear rates for rigid-on-rigid bearings in total hip replacements. Proc Inst Mech Eng H 214:331–347.
2. Walter WL, Insley GM, Walter WK, et al. 2004. Edge loading in third generation alumina ceramic-on-ceramic bearings: stripe wear. J Arthroplasty 19:402–413.
3. Nevelos J, Ingham E, Doyle C, et al. 2000. Microseparation of the centers of alumina-alumina artificial hip joints during simulator testing produces clinically relevant wear rates and patterns. J Arthroplasty 15:793–795.
4. Manaka M, Clarke IC, Yamamoto K, et al. 2004. Stripe wear rates in alumina THR - comparison of microseparation simulator study with retrieved implants. J Biomed Mater Res B Appl Biomater 69:149–157.
5. Dennis DA, Komistek RD, Northcut EJ, et al. 2001. In vivo determination of hip joint separation and the forces generated due to impact loading conditions. J Biomech 34:623–629.
6. Blumenfeld TJ, Glaser DA, Bargar WL, et al. 2011. In vivo assessment of total hip femoral head separation from the acetabular cup during 4 common daily activities. Orthopedics 34:e127–e132.
7. Walter WL, O'Toole GC, Walter WK, et al. 2007. Squeaking in ceramic-on-ceramic hips: the importance of acetabular component orientation. J Arthroplasty 22:496–503.
8. Restrepo C, Parvizi J, Kurtz SM, et al. 2008. The noisy ceramic hip: is component malpositioning the cause? J Arthroplasty 23:643–649.
9. Taylor S, Manley MT, Sutton K. 2007. The role of stripe wear in causing acoustic emissions from alumina ceramic-on-ceramic bearings. J Arthroplasty 22:47–51.
10. Keurentjes JC, Kuipers RM, Wever DJ, et al. 2008. High incidence of squeaking in THAs with alumina ceramic-on-ceramic bearings. Clin Orthop 466:1438–1443.
11. Mak MM, Jin ZM. 2002. Analysis of contact mechanics in ceramic-on-ceramic hip joint replacements. Proc Inst Mech Eng H 216:231–236.
12. Jin ZM, Dowson D, Fisher J. 1997. Analysis of fluid film lubrication in artificial hip joint replacements with surfaces of high elastic modulus. Proc Inst Mech Eng H 211:247–256.
13. Mak MM, Besong AA, Jin ZM, et al. 2002. Effect of microseparation on contact mechanics in ceramic-on-ceramic hip joint replacements. Proc Inst Mech Eng H 216:403–408.
14. Elkins JM, O'Brien MK, Stroud NJ, et al. 2011. Hard-on-hard total hip impingement causes extreme contact stress concentrations. Clin Orthop 469:454–463.
15. Sanders AP, Brannon RM. 2011. Assessment of the applicability of the hertzian contact theory to edge-loaded prosthetic hip bearings. J Biomech 44:2802–2808.
16. Walter WL, Waters TS, Gillies M, et al. 2008. Squeaking hips. J Bone Joint Surg Am 90:102–111.
17. Mai K, Verioti C, Ezzet KA, et al. 2010. Incidence of squeaking after ceramic-on-ceramic total hip arthroplasty. Clin Orthop 468:413–417.
18. Chevillotte C, Trousdale RT, Chen Q, et al. 2010. The 2009 Frank Stinchfield award: hip squeaking: a biomechanical study of ceramic-on-ceramic bearing surfaces. Clin Orthop 468:345–350.
19. Cho SJ, Moon H, Hockey BJ, et al. 1992. The transition from mild to severe wear in alumina during sliding. Acta Metallurgica et Materialia 40:185–192.
20. Laurent MP, Pourzal R, Fischer A, et al. 2011. In vivo wear of a squeaky alumina-on-alumina hip prosthesis: a case report. J Bone Joint Surg Am 93:e27.
21. Restrepo C, Post ZD, Kai B, et al. 2010. The effect of stem design on the prevalence of squeaking following ceramic-on-ceramic bearing total hip arthroplasty. J Bone Joint Surg Am 92:550–557.
22. Ranawat AS, Ranawat CS. 2007. The squeaking hip: a cause for concern-agrees. Orthopedics 30:743.
23. Hothan A, Huber G, Weiss C, et al. 2011. The influence of component design, bearing clearance and axial load on the squeaking characteristics of ceramic hip articulations. J Biomech 44:837–841.
24. Currier JH, Anderson DE, Van Citters DW. 2010. A proposed mechanism for squeaking of ceramic-on-ceramic hips. Wear 269:782–789.

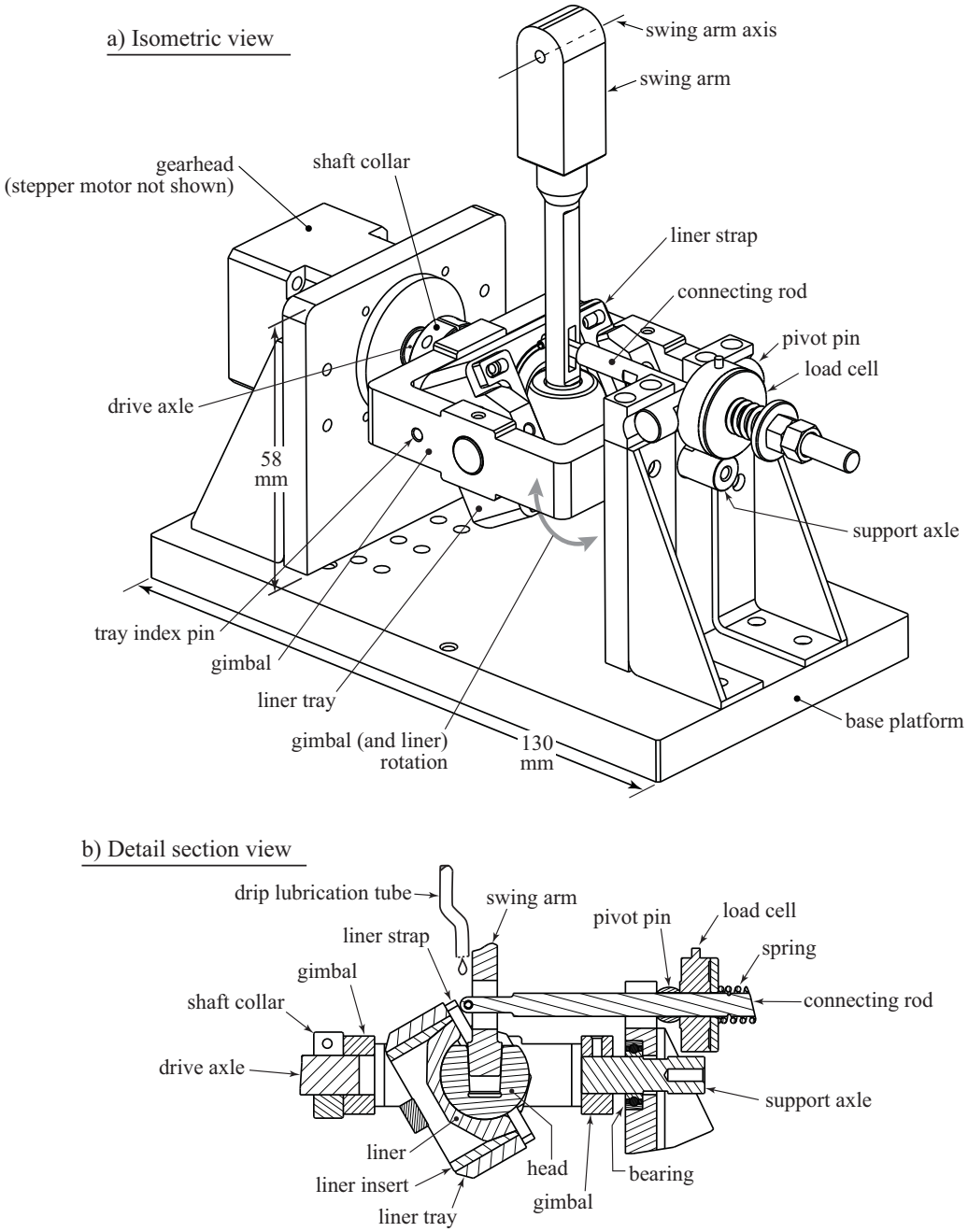


Supp. Figure S1: Schematic of Dual-Severity test apparatus. b) provides section view on longitudinal mid-plane to reveal details of holding the liner.

*Key details in a)*: Swing arm axis is axis A-A of the article's Figure 1. Drive axle and support axle form axis B-B of the article's Figure 1. Connecting rod applies spring force to swing arm. Base platform is attached to test frame actuator. Gimbal holds liner tray, in which liner is mounted. Tray index pin holds abduction angle.

*Key details in b)*: Gimbal is secured to drive axle via shaft collar. Liner straps hold liner and liner insert within liner tray. Drip lubrication tube drips fluid onto bearing from a reservoir (not shown).

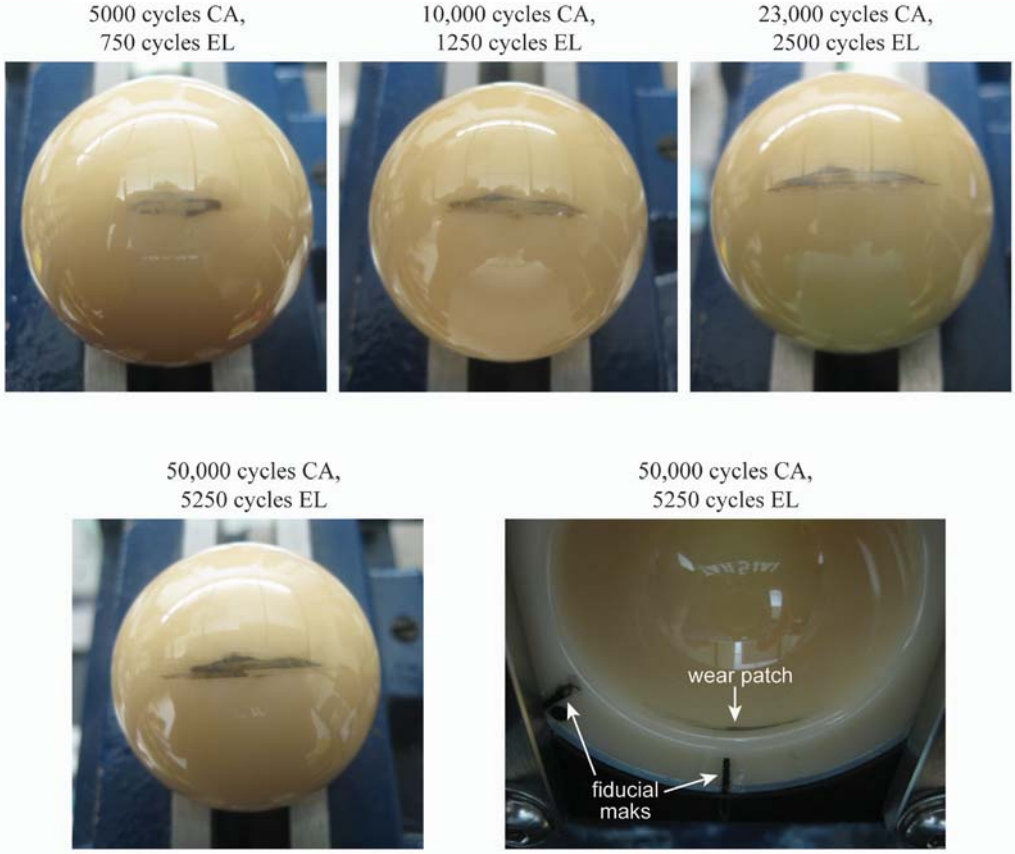


**Supp. Figure S2:** Test DS1: Photos of head and liner wear patches.

Supp Figure S3:  Femoral head after the Initial EL phase. Wear revealed by rubbing the head with a soft graphite pencil.

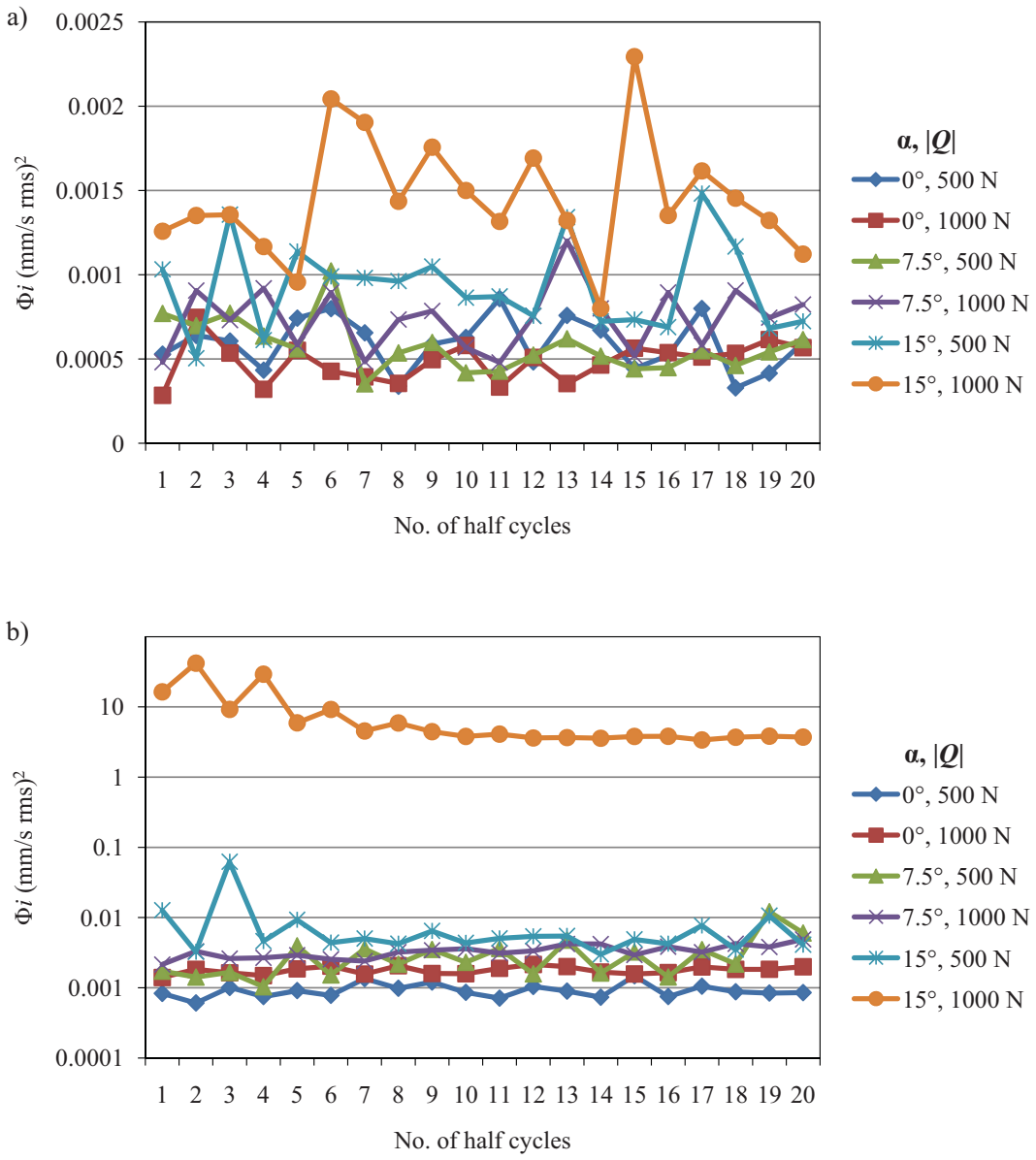


**Supp. Figure S4**: Power in squeaking frequencies ($\Phi_i$) during the Varied *Q* phase of Dual Severity Test 2. a) Liner abduction angle (θ) 45°. b) θ=60°.

**Supp. Table S1:** Liner ID surface texture measurements in Dual-Severity Test 2. Separate roughness measures defined as follows:

$R_a$: Average Roughness – Mean of the absolute deviations from the mean line
$R_t$: Total Roughness – Maximum peak-to-valley excursion
$R_p$: Peak Roughness – Average of the five greatest peaks above the mean line
$R_v$: Valley Roughness – Average of the five greatest valleys below the mean line

| | | **θ = 60°** | | | | **θ = 66°** | | | | **θ = 70°** | | | |
|---|---|---|---|---|---|---|---|---|---|---|---|---|---|
| | Cycles | $R_a$ | $R_t$ | $R_p$ | $R_v$ | $R_a$ | $R_t$ | $R_p$ | $R_v$ | $R_a$ | $R_t$ | $R_p$ | $R_v$ |
| **β = 0°** | 0 | 5 | 60 | 20 | 20 | 6 | 70 | 20 | 30 | 7 | 70 | 20 | 30 |
| | 1000 | 6 | 50 | 20 | 20 | 7 | 60 | 20 | 30 | 8 | 80 | 30 | 30 |
| | 2750 | 6 | 50 | 20 | 20 | 6 | 60 | 20 | 20 | 6 | 50 | 20 | 20 |
| | 5000 | 6 | 70 | 20 | 30 | 7 | 90 | 20 | 30 | 8 | 70 | 30 | 30 |
| | 7500 | 7 | 70 | 20 | 20 | 7 | 70 | 20 | 30 | 10 | 80 | 30 | 30 |
| | 10000 | 6 | 70 | 20 | 30 | 7 | 110 | 30 | 30 | 6 | 120 | 20 | 40 |
| | 12500 | 6 | 100 | 30 | 30 | 7 | 110 | 30 | 40 | 7 | 220 | 20 | 70 |
| | 15000 | 6 | 80 | 30 | 20 | 8 | 270 | 30 | 80 | 7 | 170 | 20 | 60 |
| | 17500 | 6 | 60 | 20 | 30 | 7 | 210 | 30 | 60 | 8 | 260 | 30 | 70 |
| | 20000 | 6 | 70 | 20 | 30 | 7 | 130 | 30 | 50 | 7 | 100 | 20 | 50 |
| | 21500 | 6 | 80 | 20 | 30 | 8 | 250 | 30 | 80 | 15 | 640 | 130 | 50 |
| | 24000 | 7 | 90 | 20 | 30 | 7 | 200 | 20 | 60 | 11 | 360 | 70 | 90 |
| | 26500 | 6 | 50 | 20 | 20 | 8 | 220 | 20 | 60 | 7 | 90 | 20 | 30 |
| **β = -25°** | 0 | 5 | 60 | 20 | 20 | 6 | 70 | 20 | 30 | 7 | 70 | 20 | 30 |
| | 1000 | 6 | 60 | 20 | 20 | 6 | 60 | 20 | 20 | 6 | 50 | 20 | 20 |
| | 2750 | 6 | 50 | 20 | 20 | 9 | 80 | 30 | 30 | 6 | 80 | 20 | 30 |
| | 5000 | 6 | 50 | 20 | 20 | 8 | 100 | 30 | 30 | 7 | 90 | 20 | 30 |
| | 7500 | 7 | 130 | 30 | 30 | 8 | 130 | 30 | 40 | 7 | 100 | 20 | 40 |
| | 10000 | 5 | 50 | 20 | 20 | 6 | 80 | 20 | 30 | 7 | 90 | 30 | 30 |
| | 12500 | 6 | 60 | 20 | 30 | 8 | 90 | 30 | 30 | 7 | 130 | 30 | 40 |
| | 15000 | 6 | 50 | 20 | 20 | 8 | 140 | 30 | 40 | 7 | 80 | 20 | 30 |
| | 17500 | 6 | 50 | 20 | 20 | 7 | 100 | 20 | 30 | 7 | 70 | 30 | 30 |
| | 20000 | 5 | 50 | 20 | 20 | 6 | 90 | 20 | 30 | 6 | 70 | 20 | 30 |
| | 21500 | 6 | 50 | 20 | 20 | 6 | 100 | 30 | 30 | 7 | 110 | 30 | 40 |
| | 24000 | 6 | 70 | 20 | 20 | 6 | 60 | 20 | 20 | 9 | 130 | 40 | 40 |
| | 26500 | 6 | 50 | 20 | 20 | 8 | 60 | 20 | 30 | 7 | 90 | 30 | 30 |
| **β = 25°** | 0 | 5 | 60 | 20 | 20 | 6 | 70 | 20 | 30 | 7 | 70 | 20 | 30 |
| | 1000 | 6 | 50 | 20 | 20 | 6 | 50 | 20 | 20 | 6 | 50 | 20 | 20 |
| | 2750 | 6 | 60 | 20 | 20 | 6 | 50 | 20 | 20 | 9 | 70 | 30 | 30 |
| | 5000 | 7 | 60 | 30 | 20 | 8 | 70 | 30 | 30 | 9 | 80 | 60 | 40 |
| | 7500 | 8 | 70 | 30 | 30 | 6 | 50 | 20 | 20 | 8 | 80 | 30 | 30 |
| | 10000 | 6 | 50 | 20 | 20 | 6 | 70 | 30 | 20 | 7 | 60 | 20 | 30 |
| | 12500 | 6 | 80 | 20 | 30 | 6 | 70 | 20 | 20 | 7 | 50 | 20 | 20 |
| | 15000 | 5 | 50 | 20 | 20 | 7 | 70 | 50 | 50 | 6 | 50 | 20 | 20 |
| | 17500 | 6 | 50 | 20 | 20 | 6 | 60 | 20 | 20 | 7 | 70 | 30 | 30 |
| | 20000 | 6 | 50 | 20 | 20 | 7 | 60 | 20 | 20 | 6 | 70 | 20 | 30 |
| | 21500 | 6 | 110 | 30 | 30 | 6 | 60 | 20 | 20 | 7 | 70 | 30 | 30 |
| | 24000 | 6 | 50 | 20 | 30 | 6 | 60 | 20 | 20 | 6 | 60 | 20 | 20 |
| | 26500 | 7 | 100 | 20 | 30 | 6 | 50 | 20 | 20 | 7 | 120 | 20 | 40 |

| | | θ = 74° | | | | θ = 78° | | | | θ = 82° | | | |
|---|---|---|---|---|---|---|---|---|---|---|---|---|---|
| | Cycles | $R_a$ | $R_t$ | $R_p$ | $R_v$ | $R_a$ | $R_t$ | $R_p$ | $R_v$ | $R_a$ | $R_t$ | $R_p$ | $R_v$ |
| β = 0° | 0 | 8 | 80 | 30 | 30 | 7 | 70 | 20 | 20 | 11 | 80 | 30 | 40 |
| | 1000 | 6 | 50 | 20 | 20 | 7 | 80 | 30 | 30 | 14 | 120 | 50 | 50 |
| | 2750 | 7 | 80 | 20 | 30 | 7 | 80 | 20 | 30 | 13 | 200 | 40 | 90 |
| | 5000 | 9 | 110 | 30 | 40 | 10 | 100 | 30 | 40 | 19 | 400 | 60 | 230 |
| | 7500 | 9 | 190 | 30 | 60 | 10 | 140 | 40 | 60 | 15 | 200 | 40 | 120 |
| | 10000 | 10 | 130 | 30 | 50 | 11 | 110 | 40 | 60 | 19 | 470 | 50 | 200 |
| | 12500 | 9 | 180 | 30 | 50 | 13 | 230 | 40 | 120 | 17 | 380 | 50 | 220 |
| | 15000 | 9 | 170 | 30 | 60 | 17 | 300 | 50 | 150 | 19 | 470 | 50 | 160 |
| | 17500 | 9 | 130 | 30 | 50 | 33 | 600 | 100 | 310 | 16 | 310 | 40 | 170 |
| | 20000 | 12 | 270 | 40 | 110 | 45 | 810 | 100 | 250 | 17 | 390 | 40 | 170 |
| | 21500 | 13 | 270 | 40 | 90 | 49 | 610 | 110 | 280 | 20 | 440 | 50 | 180 |
| | 24000 | 16 | 230 | 50 | 130 | 27 | 270 | 60 | 160 | 12 | 170 | 40 | 60 |
| | 26500 | 11 | 170 | 50 | 40 | 26 | 350 | 60 | 170 | 12 | 150 | 40 | 60 |
| β = -25° | 0 | 8 | 80 | 30 | 30 | 7 | 70 | 20 | 20 | 11 | 80 | 30 | 40 |
| | 1000 | 9 | 80 | 30 | 30 | 7 | 50 | 20 | 20 | 7 | 70 | 20 | 30 |
| | 2750 | 7 | 70 | 20 | 30 | 8 | 70 | 20 | 30 | 8 | 60 | 20 | 30 |
| | 5000 | 7 | 90 | 20 | 30 | 11 | 100 | 30 | 40 | 15 | 330 | 60 | 80 |
| | 7500 | 7 | 90 | 30 | 30 | 9 | 100 | 30 | 50 | 8 | 80 | 20 | 40 |
| | 10000 | 7 | 110 | 30 | 40 | 12 | 480 | 40 | 130 | 7 | 100 | 20 | 40 |
| | 12500 | 7 | 100 | 20 | 40 | 9 | 80 | 30 | 50 | 7 | 70 | 20 | 40 |
| | 15000 | 8 | 100 | 20 | 40 | 12 | 180 | 40 | 90 | 9 | 110 | 30 | 50 |
| | 17500 | 7 | 80 | 20 | 30 | 10 | 140 | 30 | 70 | 8 | 140 | 20 | 50 |
| | 20000 | 8 | 290 | 30 | 100 | 15 | 220 | 30 | 110 | 10 | 170 | 30 | 70 |
| | 21500 | 8 | 110 | 20 | 50 | 15 | 230 | 40 | 140 | 14 | 230 | 30 | 90 |
| | 24000 | 7 | 80 | 20 | 30 | 12 | 150 | 30 | 60 | 10 | 150 | 30 | 60 |
| | 26500 | 7 | 80 | 20 | 30 | 12 | 130 | 40 | 50 | 12 | 190 | 30 | 90 |
| β = 25° | 0 | 8 | 80 | 30 | 30 | 7 | 70 | 20 | 20 | 11 | 80 | 30 | 40 |
| | 1000 | 7 | 50 | 20 | 30 | 6 | 60 | 20 | 30 | 6 | 50 | 20 | 20 |
| | 2750 | 7 | 70 | 20 | 30 | 6 | 60 | 20 | 20 | 8 | 70 | 30 | 30 |
| | 5000 | 6 | 60 | 20 | 20 | 10 | 80 | 30 | 30 | 6 | 60 | 20 | 30 |
| | 7500 | 9 | 270 | 40 | 50 | 7 | 70 | 20 | 30 | 8 | 80 | 30 | 30 |
| | 10000 | 8 | 190 | 30 | 80 | 9 | 200 | 30 | 70 | 7 | 70 | 20 | 30 |
| | 12500 | 9 | 180 | 30 | 90 | 12 | 190 | 40 | 90 | 8 | 90 | 20 | 40 |
| | 15000 | 9 | 230 | 30 | 80 | 12 | 140 | 30 | 60 | 8 | 90 | 20 | 40 |
| | 17500 | 11 | 400 | 30 | 170 | 13 | 250 | 40 | 120 | 12 | 210 | 40 | 80 |
| | 20000 | 9 | 120 | 30 | 60 | 14 | 190 | 40 | 70 | 13 | 210 | 30 | 80 |
| | 21500 | 9 | 160 | 30 | 50 | 13 | 210 | 30 | 70 | 13 | 170 | 40 | 70 |
| | 24000 | 8 | 150 | 30 | 50 | 18 | 170 | 50 | 80 | 18 | 230 | 40 | 120 |
| | 26500 | 10 | 180 | 30 | 80 | 17 | 190 | 50 | 90 | 16 | 230 | 40 | 120 |

# CHAPTER 7

# A PROXY WEAR TEST FOR EDGE LOADING IN HIP PROSTHESES: USING HERTZIAN SURROGATE TEST SPECIMENS TO EVALUATE CERAMIC MATERIAL PAIRS

An article prepared for submission to the Journal of Orthopaedic Research

## 7.1 Abstract

This research has developed a novel test method for evaluating the wear resistance of ceramic materials under severe contact stresses simulating edge loading in prosthetic hip bearings. Simply shaped test specimens – a cylinder and a spheroid – were designed as surrogates for an edge-loaded, head/liner implant pair. Equivalency of the simpler specimens was assured in the sense that their theoretical contact dimensions and pressures were identical, according to Hertzian contact theory, to those of the head/liner pair. The surrogates were fabricated in three ceramic materials: $Al_2O_3$, zirconia-toughened alumina (ZTA), and $ZrO_2$. They were mated in three different material pairs and reciprocated under a 200 N normal contact force for 1,000-2,000 cycles, which created small (<1 $mm^2$) wear scars. The three material pairs were ranked by their wear resistance, quantified by the volume of abraded material measured using an interferometer. Similar tests were performed on edge-loaded hip implants in the same material pairs. The surrogates replicated the wear rankings of their full-scale implant counterparts and mimicked their friction force trends. The results show that a proxy test using simple test specimens can validly rank the wear performance of ceramic materials under severe, edge-loading contact stresses, while replicating the beginning stage of edge-loading wear. This simple wear test is therefore potentially useful for screening new, prospective materials early in their development, to produce optimized candidates for more complicated full-scale hip simulator wear tests.

### 7.1.1 Keywords

Prosthetic hip, ceramic, edge loading, wear, Hertzian contact theory, materials ranking

## 7.2 Introduction

This research has developed a novel test method useful in the field of orthopaedic implant materials that fulfills two previously unmet needs pertinent to materials employed for ceramic-on-ceramic (CoC) prosthetic hip joints.

First, the new test method accurately simulates the severe contact stresses caused by edge loading in prosthetic hip joints. Edge loading occurs when the prosthetic femoral head subluxes out of the acetabular cup/liner and bears upon the liner's interior edge rather than its spherical bearing surface. Fluoroscopic imaging has revealed that such subluxation can occur in a variety of human activities.[1,2] Edge loading induces high contact stresses[3] that can rapidly elicit wear on the femoral head, which may lead to further liner wear and to disturbing squeaking noises.[4,5] To overcome these negative effects, prosthesis developers need material and implant tests that accurately, yet economically, represent edge loading. The new test method described herein meets this need by using a simply shaped surrogate contact pair that represents, to second-order accuracy,[6] an edge-loaded head/liner contact pair.

Second, the new test method is suitable for use in the early stages of new material research and development. Heretofore, most prosthetic hip bearing test methods have been developed for full-scale implants, thus cost-limiting their utility to explore a broad spectrum of candidate materials. A standard simulator wear test involves only the mild contact stresses caused during concentric articulation.[7] An adaptation of this method has included edge loading and thus produced clinically relevant edge-loading wear on ceramic hips;[8] yet, that method applies only to full-scale implants. Pin-on-disk wear tests are potentially useful for early-stage materials research,[9,10] but those tests do not represent the geometry of edge-loaded hips, nor does continuous sliding of a sphere on a disk accurately represent

the relative motion of subluxation. Hence, the state of the art in testing for prosthetic hip bearings is deficient because it does not include sufficient means to evaluate new materials – early in their development – for the severe edge-loading conditions experienced in-vivo. The test method developed in this research resolves this deficit by providing an edge-loading wear test suited to simple shapes (namely, cylinders and spheroids) that can be made from basic form (e.g., cylinder, disk, plate) material specimens.

This article describes the novel test method and its validation via ranking wear tests performed on three contemporary ceramic materials. The surrogate pair's design is described, and contact analysis shows its second-order equivalence to a full-scale head/liner (H/L) pair under edge loading. Index, short-duration (e.g., 2,000 cycles) edge-loading wear tests were performed on H/L pairs in three different CoC combinations. Wear scars on the heads were measured optically, and the three material pairs were ranked in order of wear resistance. Analogous wear tests of three surrogate pairs yielded an equivalent wear ranking, along with similar trends in friction. This consistency in outcomes validates a novel, effective means to rapidly screen potential new hip bearing materials for their wear performance under severe edge-loading contact stresses.

## 7.3 Methods

### 7.3.1 Test specimens and surrogate pair design

The H/L edge-load wear tests consisted of short-stroke reciprocated sliding, centered at a point on the liner's inner edge. Two slightly different ceramic liners were involved, a commercial liner (CL) and a facsimile liner (FL). Figure 7.1a shows the test arrangement with a CL, and the magnified view illustrates the observation that the cross-sectional edge

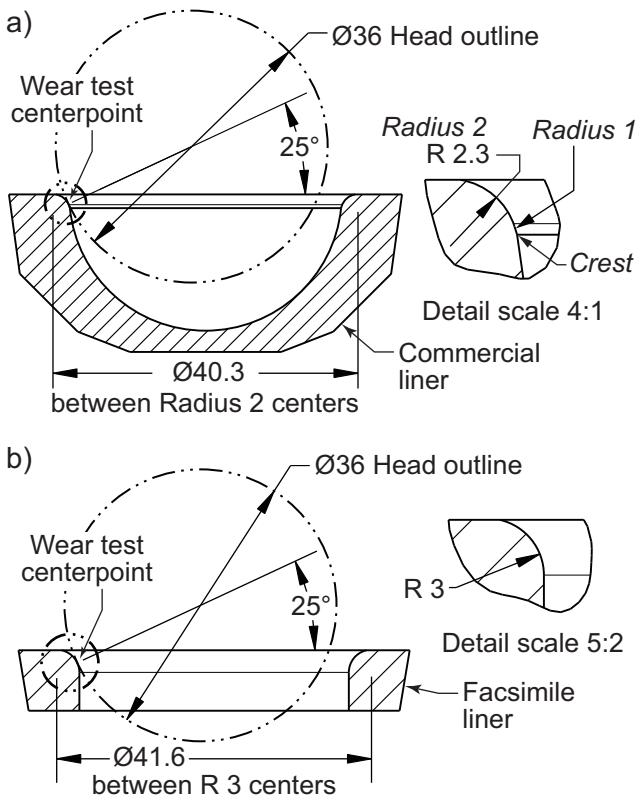


Figure 7.1. Section views of liner components showing wear test centerpoints and detail views of edges. a) Commercial liner (CL). b) Facsimile liner (FL). Dimensions in mm.

profile of a typical CL consists of multiple differently shaped segments (identified by figure labels *Radius 2*, *Radius 1*, and *Crest*).[11] To alleviate this complexity of form, a second liner – an FL with a crest-free edge of single, 3 mm radius (Figure 7.1b) – was made by re-grinding and polishing it from a CL. The FL was dimensionally verified with a touch-probe coordinate measuring machine (CMM), and was tested along with the CL. With these liner specimens, there were two H/L edge-load wear test series, one with heads paired against a CL and one with heads paired against an FL.

A third wear test series was performed using a mating pair composed of a cylinder and a spheroid (C/S pair) designed as surrogates for an edge-loaded, H/L pair. Figure 7.2 il-

lustrates the C/S pair's mating configuration, which simulated edge loading in the Head/FL pair. The following equations, previously detailed and validated for the design of Hertzian surrogate contact pairs,[6] were used to design the surrogate specimens (Table 7.1 and Figure 7.2 define the nomenclature):

$$r_1 = 1/\kappa_{2R} \qquad r_2 = \sqrt{1/(\kappa_{1R}\kappa_{2R})} \tag{1}$$

$$\kappa_{1R} = \tfrac{1}{2}(\Sigma_O - \Delta_O) \qquad \kappa_{2R} = \tfrac{1}{2}(\Sigma_O + \Delta_O - 2\rho_{2R}) \tag{2}$$

$$\Sigma_O = \kappa_{1O} + \kappa_{2O} + \rho_{1O} + \rho_{2O} \tag{3}$$

$$\Delta_O = \left[(\kappa_{1O} - \kappa_{2O})^2 + (\rho_{1O} - \rho_{2O})^2 + 2(\kappa_{1O} - \kappa_{2O})(\rho_{1O} - \rho_{2O})\cos(2\alpha)\right]^{\frac{1}{2}} \tag{4}$$

The curvatures, $\kappa_{1O}$ and $\kappa_{2O}$, were computed using dimensions of the FL and formulas for the curvatures of a torus.[12] Equations 1-4 were used iteratively with selected values of $\rho_{2R}$ to determine convenient (i.e. easily manufactured) dimensions of the surrogate cylinder and spheroid, which were as follows: $r_1$=5.148 mm, $r_2$=30.521 mm, and $r_3$=5.137 mm.

A Hertzian contact analysis was performed to verify that under identical normal contact forces, a head/FL pair and its surrogate C/S pair would experience contact areas and pressures at the wear test centerpoint that would be equal to second-order accuracy (with respect to distance from the initial contact point) according to Hertzian theory. Our prior research has described the analysis method and validated its accuracy in edge-loaded CoC hips,[11] and this work now includes the effect of sliding. The material properties were those of $Al_2O_3$ (Table 7.2) for all components. The values of $r_1$, $r_2$, and $r_3$ described the C/S pair, and the dimensions in Figure 7.1b described the Head/FL pair. Also, quasi-static contact tests were performed on $Al_2O_3$ Head/FL and C/S pairs to measure their contact patch di-

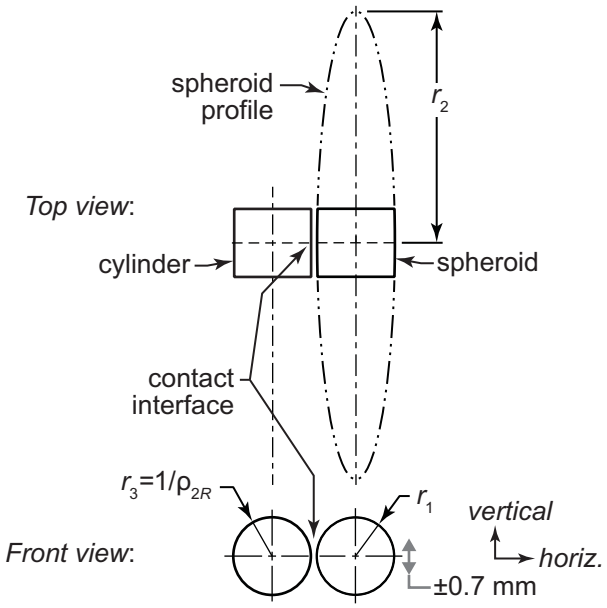


Figure 7.2. Surrogate cylinder and spheroid as arranged for wear test (with contact interface gap for clarity). *Top view*: Spheroid is broadly curved, so a dashed ellipse shows its profile. *Front view*: 2-headed gray arrow indicates reciprocation of spheroid relative to cylinder; *vertical* and *horiz*. labels denote directions in the wear test setup.

Table 7.1. Mathematical nomenclature

| | |
|---|---|
| $\kappa_{1O}$, $\kappa_{2O}$ | Principal curvatures on the liner's edge at wear test centerpoint, $\lvert\kappa_{1O}\rvert<\lvert\kappa_{2O}\rvert$ |
| $\rho_{1O}$, $\rho_{2O}$ | Principal curvatures of the femoral head. $\rho_{1O}=\rho_{2O}$ since the head is spherical. |
| $\alpha$ | Angle between planes of minimal principal curvature. $\alpha=0$ since the head is spherical. |
| $\Delta_O$, $\Sigma_O$ | Functions of the liner and head principal curvatures |
| $\kappa_{1R}$, $\kappa_{2R}$ | Principal curvatures on the surrogate spheroid at the wear test centerpoint |
| $\rho_{2R}$ | Curvature of the surrogate cylinder (= $1/r_3$) |
| $r_1$, $r_2$; $r_3$ | Minor, major radii of the surrogate spheroid; radius of the surrogate cylinder |
| p | P-value, from Student's t-test |

Table 7.2. Material properties. All values from manufacturers, except (*) from Ref. 23, and ZTA Poisson's ratio assumed identical to $Al_2O_3$.

| Material | Avg. grain size (μm) | Hardness, HV (GPa) | Density ($g/cm^3$) | Fracture toughness, $K_{IC}$ ($MPa\sqrt{m}$) | Young's modulus (MPa) | Poisson's ratio |
|---|---|---|---|---|---|---|
| [a] $Al_2O_3$ | 1.75 | 20 | 3.97 | 3.2 | 380,000* | 0.24* |
| [b] ZTA | 0.56 | 19 | 4.37 | 6.5 | 358,000 | 0.24 |
| [c] $ZrO_2$ | 0.5 | 13 | 6.01 | 7 | 207,000 | 0.31 |

[a] Biolox Forte, Ceramtec, Plochingen, Germany
[b] ZTA = zirconia-toughened alumina. Biolox Delta, Ceramtec, Plochingen, Germany
[c] Amzirox86, AstroMet, Cincinatti, OH, USA

mensions under a range of normal forces following our previously described procedure; the C/S tests were performed with the specimens arranged per Figure 7.2.

Table 7.2 describes the properties of the three ceramic materials used in the wear tests. The heads were implant products, except the $ZrO_2$ head, which was custom made. The CL was an implant product, and the FL was machined from a liner identical to the CL. The cylinders and spheroids were machined from head implants, except the $ZrO_2$ cylinder which was custom made. The dimensions of the cylinders were verified with micrometers. The dimensions of the spheroids were measured at 144X magnification using an optical CMM (Nexiv VMR 3020, Nikon, Japan) and fitting silhouetted edge points sampled at 10 μm increments with a best-fit ellipse, thus finding the spheroid's $r_1$ and $r_2$ dimensions. The surface texture of the $Al_2O_3$ and ZTA heads and the CL was that of the original implants; on all others, it was from the custom manufacturing. Areal surface textures were measured using a scanning white light interferometer (SWLI) (NewView 5032, Zygo, CT).

### 7.3.2 Wear test and measurement protocols

Figure 7.3 is a schematic for all H/L edge-load wear tests. The liner was secured by a taper fit with a titanium implant shell, and the shell was fastened within a supporting test block of rigid polyurethane foam. This assembly was fixed to the surface of a sine plate angled at 25°. The sine plate was mounted to the vertical actuator of a servohydraulic test frame. The femoral head was mounted to a swing-arm, and a horizontal spring mechanism pressed the head into contact with the liner's edge. The swing arm could pivot about a fixed axis to maintain contact between the head and the liner's edge when the actuator reciprocated the liner vertically. A gravity-powered drip system lubricated the contact interface. The FL was tested likewise, since it fit with the shell via the same taper fit. A similar setup was used to test the surrogate pairs, though naturally with different fixtures to fasten the cylinder to the swing arm and the spheroid to the actuator. As illustrated in Figure 7.2, the cylinder and spheroid were arranged with their major axes in parallel.

The various components and materials were combined for wear tests as shown by Figure 7.4 (which also introduces abbreviations for the three material pairs). Six trials were

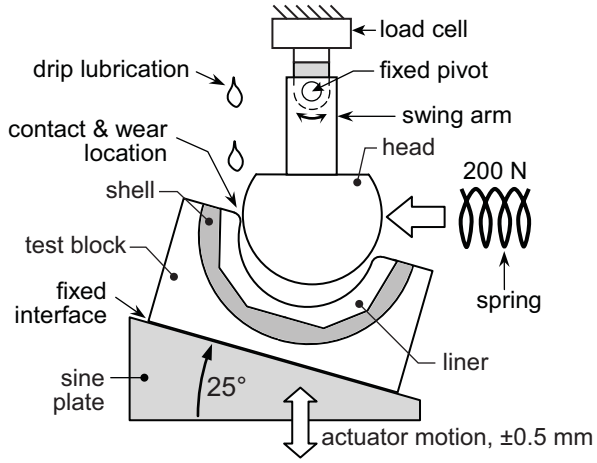


Figure 7.3. Schematic of implant H/L edge-load wear test.

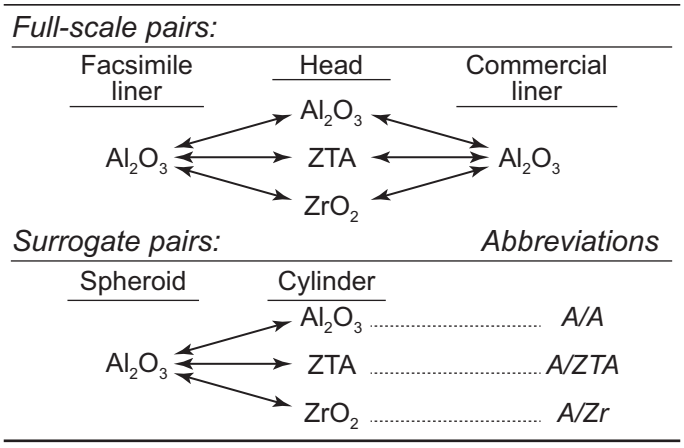


Figure 7.4. Test pairs. Abbreviations for material pairs apply to all tests.

performed for each pair; the resulting wear scars were small, so each specimen was tested several times by repositioning it to test fresh surface locations to help determine reproducibility of the results.

The test procedure for H/L pairs started with aligning the components to position the test centerpoint to be simultaneously on the head's equator and on the liner's midplane (liner section plane shown in Figures 7.1 and 7.3). The spring mechanism was pre-loaded to 200 N. A solution of bovine serum with 17.5 g/L protein content was drip fed via a needle valve to the contact interface at 10 drops/min. The liner was reciprocated vertically ±0.5 mm from the centerpoint at 1 Hz in a sinusoidal pattern, producing a calculated 0.86 mm long wear path on the head. The tests were run for the following durations: Head/CL tests: 2,000 cycles; Head/FL tests: 2,250 cycles; A/A and A/ZTA C/S tests: 1,000 cycles; A/Zr C/S tests: 2,000 cycles. As discussed later in the article, these test durations were selected via preliminary trials such that the different test series were halted once a small (~1 mm wide) wear scar visible had formed. The peak vertical loads registered by the test frame's load cell were recorded at regular intervals throughout each trial.

The surrogate C/S pairs were tested in a similar manner. The specimens were mated and articulated as diagrammed in Figure 7.2. The cylinder was mounted to the end of a swing arm (analogous to the head's swing arm fixture) and loaded by the spring mechanism to create a 200 N normal contact force between the cylinder and spheroid. The spheroid was reciprocated vertically (analogous to the liner motion) ±0.7 mm from the centerpoint, producing a calculated wear path length of 0.7 mm on each member. The test frequency was 1.23 Hz to equalize the average sliding speed with that of the Head/FL pair. The cylinder's wear path was shorter than the head's to accommodate limitations of the SWLI used to measure wear. The instrument's accuracy diminished with increasing surface slope, and since the cylinder (radius=5.1 mm) sloped more rapidly than the head (radius=16 mm), the cylinder's wear path was designed to be shorter than the head's. To normalize for the differing wear path lengths, the wear measurements were ranked according to the wear factor, defined as *Wear Volume* / (*Normal Force* × *Total Sliding Distance*).

The wear scars on the heads and cylinders were measured using the SWLI. The instrument provided a 0.72×0.54 mm field of view, a pixel size of 1.1 μm, a lateral resolution of 2.7 μm, and a vertical resolution of ~2 nm. The measured region included the wear scar and an ample portion of the surrounding unworn surface, and the region was automatically stitched together from multiple overlapping fields of view. The SWLI determined the volume lost to wear using a previously described algorithm.[13] All test specimens were cleaned with water and mild detergent, rinsed in a jet of water, and wiped with acetone prior to wear scar imaging and measurement.

## 7.4 Results

For the Hertzian contact analysis, Figure 7.5 shows that for the Head/FL and C/S pairs, the predicted dimensions of the elliptical contact patches were identical, by design. The contact pressures (not shown) were likewise theoretically identical to second-order accuracy with respect to distance from the contact point. For a normal contact force of 200 N as applied in the wear tests, the predicted maximum contact pressures for the three material pairs were as follows: A/A: 2,157 MPa; A/ZTA: 2,114 MPa; A/Zr: 1,729 MPa.

Figure 7.6 shows the surface textures of the heads and cylinders, and Table 7.3 gives their quantitative values. On all specimens, the surface roughness was <20 nm $R_a$ as specified by a standard for CoC hip bearings.[14] Nevertheless, the heads and liners were generally smoother than their surrogate counterparts in both $R_a$ and $R_p$ surface texture measures, and the differences were statistically significant ($p<0.04$), except in the comparison between the FL and the spheroid.

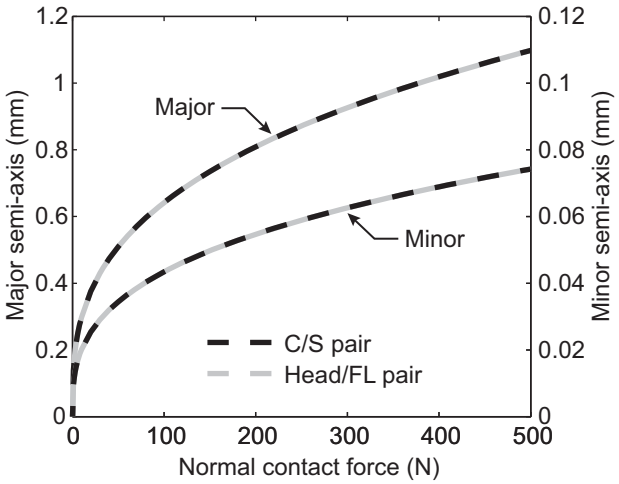


Figure 7.5. Hertzian contact analysis of surrogate C/S pair and Head/FL pair, showing dimensions of the predicted contact patches. Results directly overlie one another.

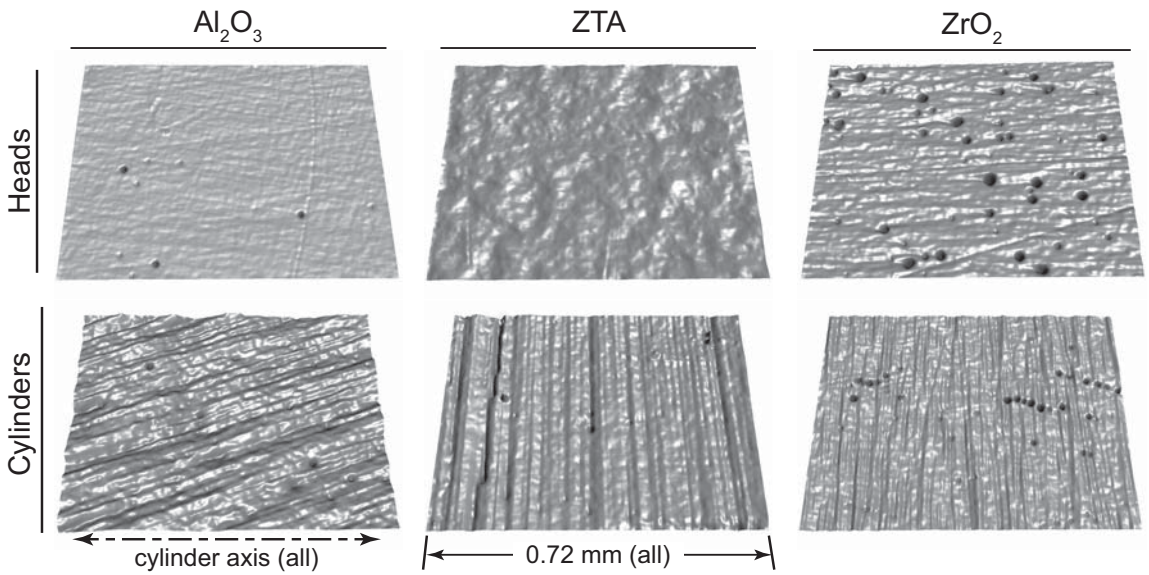


Figure 7.6. Surface textures. Height is magnified for emphasis; scale is equal in all images.

Table 7.3. Specimen areal surface textures measured by SWLI (mean of 7 measurements). Values in nm.

| | | Member 1 | | Member 2 | | |
|---|---|---|---|---|---|---|
| Material | Roughness | Full-scale *Head* | Surrogate *Cylinder* | Full-scale *CL* | Full-scale *FL* | Surrogate *Spheroid* |
| $Al_2O_3$ | $R_a$ | 1[a] | 11[b] | 8[a] | 11[b] | 13[b] |
| | $R_p$ | 7 | 48 | 32 | 52 | 46 |
| ZTA | $R_a$ | 4[a] | 6[b] | | | |
| | $R_p$ | 14 | 30 | | | |
| $ZrO_2$ | $R_a$ | 4[c] | 6[c] | | | |
| | $R_p$ | 20 | 28 | | | |

$R_a$ = Arithmetic mean deviation from the mean plane
$R_p$ = Mean of the highest peak in each of 25 equally sized sampling areas
Polishing sources: [a] Ceramtec, Plochingen, Germany (OEM polish), [b] D.K. Milovic Co., Livermore, CA
[c] AstroMet, Cincinnati, OH

Figure 7.7 compares the measured and theoretical contact patches from the quasi-static tests. The actual contact patches were measured with the optical CMM,[11] and the theoretical patches were computed using Hertzian contact theory with the specimens' measured dimensions. As-designed, the contact patches had theoretically identical (Figure 7.5 and Ref. 6) major and minor diameters (1.618 and 0.109 mm). The actual C/S contact patch was longer than its design mainly because the spheroid itself was elongated (measured $r_2$=36.741 mm) relative to the design ($r_2$=30.521 mm). Results (not shown) at 100 N and 300 N contact forces were similar to those at 200 N.

Figure 7.8 shows examples of the wear scars. In the optical micrographs, the darker regions correspond to roughening with loss of material or material pile-up. In each 3D SWLI surface model, the approximately planar regions exterior to the wear scar represent unworn surface, and depressed areas below the plane represent material lost due to wear. The planar appearance is achieved by subtracting a geometric model, determined by best-fit to the unworn portions, from the entire measurement data set, which permitted the wear to be computed as the volume between the plane and the depressed surfaces.[13] For the heads, the geometric model was a sphere. For the cylinder specimens, the model was

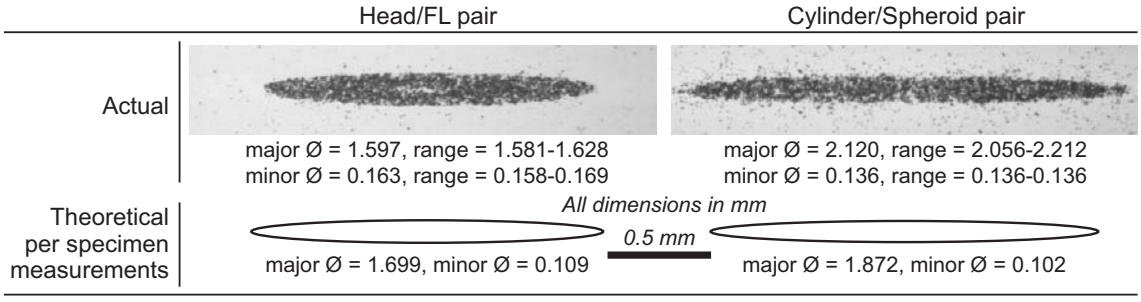


Figure 7.7. Actual and theoretical quasi-static contact patches. Actual: mean and range from 3 trials. A/A material pairs with normal load of 200 N. 0.5 mm scale bar applies to all.

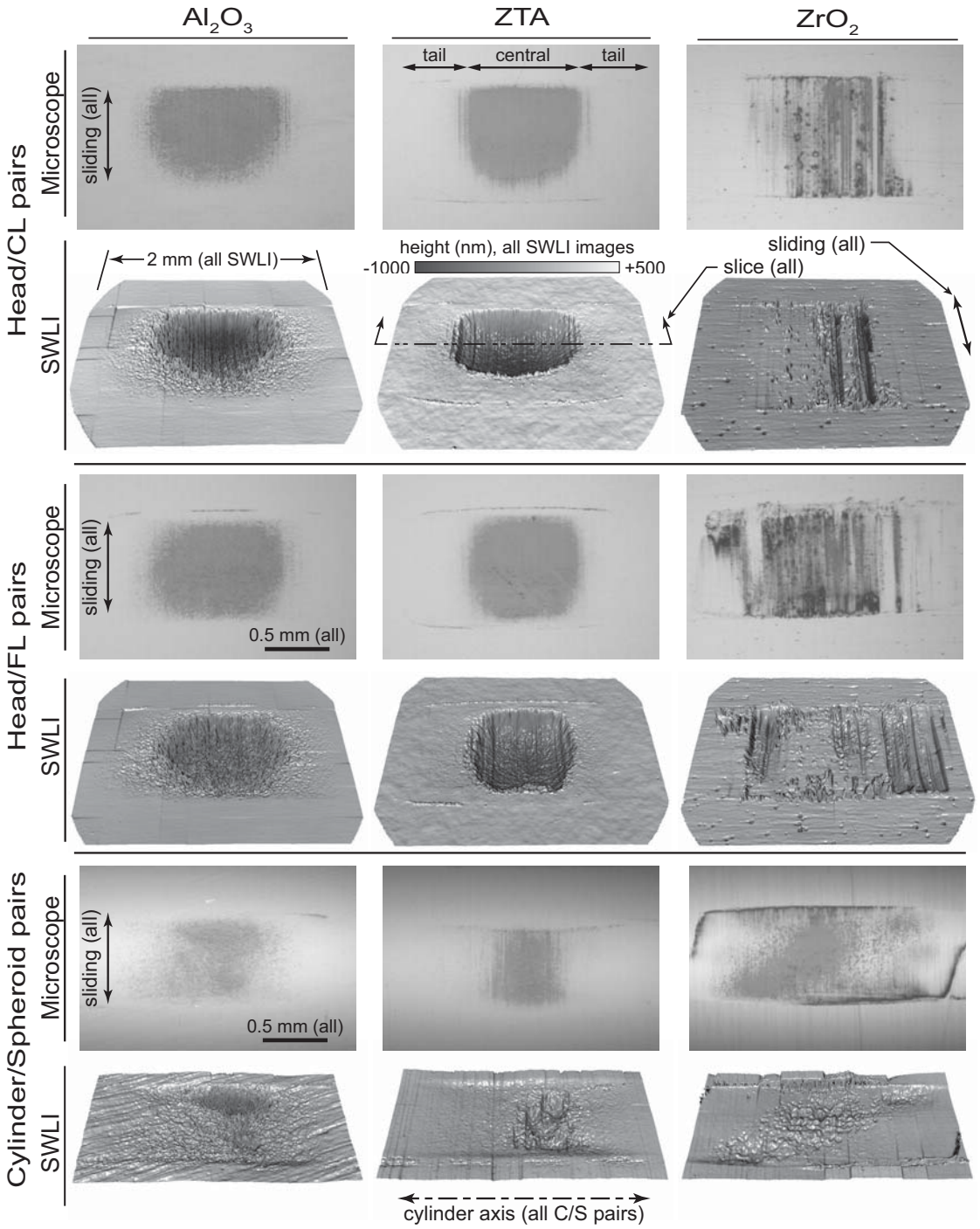


Figure 7.8. Wear scars imaged by optical microscope (viewed normal to surface) and SWLI (viewed obliquely to surface, height scale equal in all and magnified to emphasize texture).

a 4th-order polynomial, which gave a better fit than an analytical cylinder because some of the cylinder specimens' surfaces had small amplitude (e.g., 0.5 μm), long wavelength (e.g., 4 mm) waviness, which was an artifact from their finishing process. Figure 7.9 shows example wear scar depth profiles. The Head/CL pairs generally had the deepest wear scars, even though their tests ran for 250 cycles less than the Head/FL pairs.

On the $Al_2O_3$ and ZTA test specimens, the wear scars generally consisted of a ~1 mm wide central region along with tail regions to either side extending the scar to ~2 mm wide. In the central region, the polished surface was entirely denuded; the tail regions exhibited diminishing roughness and reduced grain pull-out with distance from the center. On the cylinders, the deepest worn portion was eccentrically located in some cases (e.g., C/S pair,

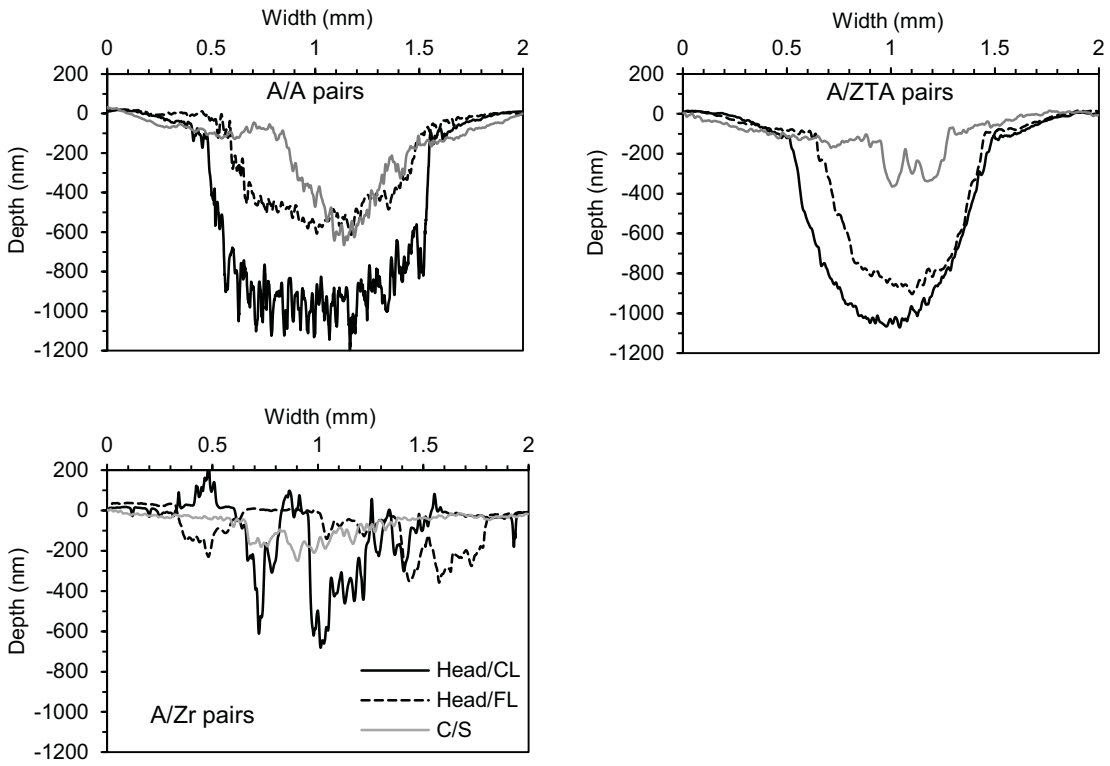


Figure 7.9. Wear scar depth examples; 2D slices through SWLI data as indicated in Figure 7.8. Legend in A/Zr graph applies to all.

ZTA, Figure 7.8), probably because the cylinder's minute surface waviness affected the contact pressure distribution. On the $ZrO_2$ heads, the scars were darkly discolored and generally had narrow grooves, parallel to the sliding direction, that were not uniformly centered within the scar. The $ZrO_2$ cylinders were less discolored, and they exhibited disperse roughened patches rather than grooves of wear.

Figure 7.10 displays the trends of the peak friction force (which occurred when sliding reversed directions) at each measurement interval. Figure 7.11 compares the calculated wear factors. Within each test series (e.g., Head/CL), the difference between A/A and A/ZTA pairs was not statistically significant (i.e., $p>0.05$), but the difference between each of these and the A/Zr pair was.

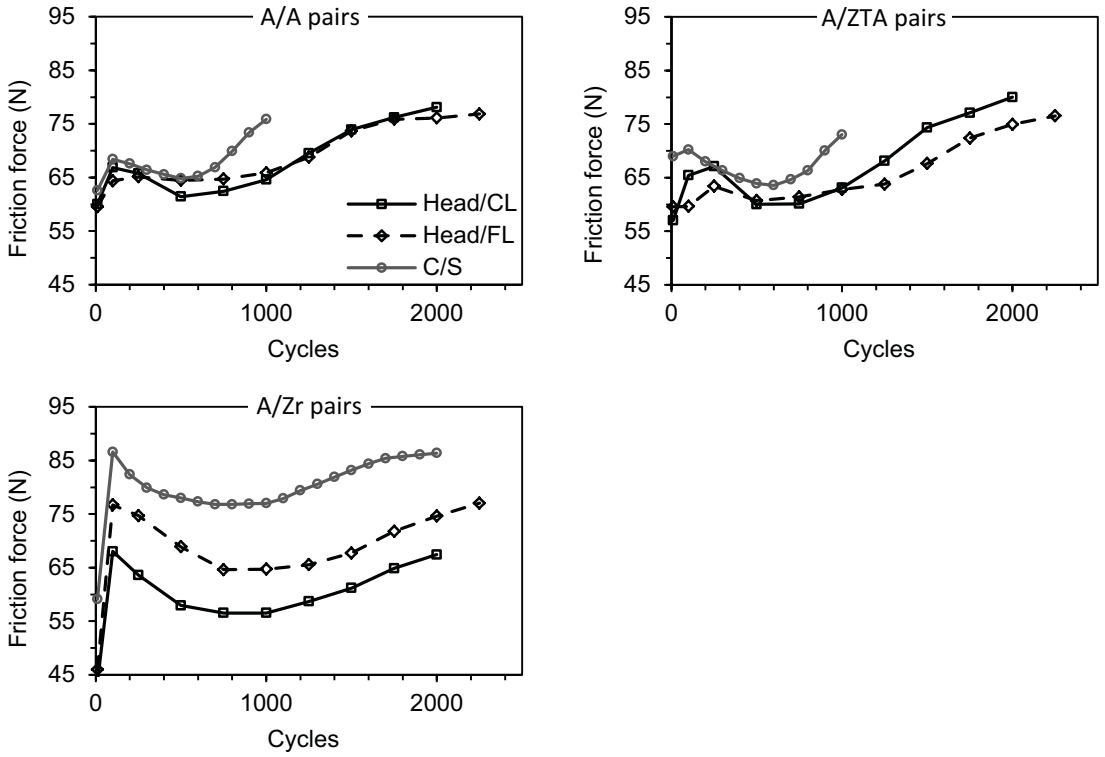


Figure 7.10. Average peak friction force, graphed by material pair, validating the assertion that the surrogate (C/S) specimens are able to mimic the trends of the full-scale component specimens. Legend in A/A graph applies to all.

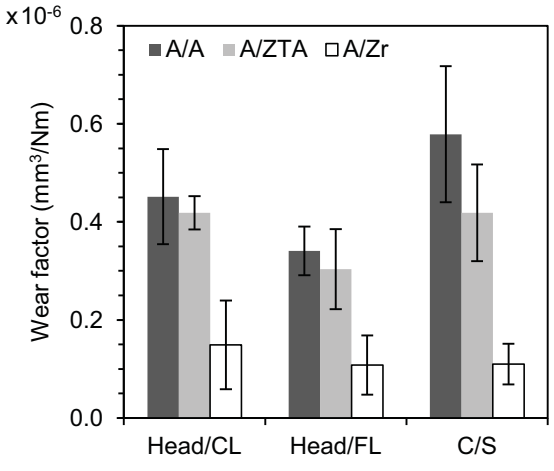


Figure 7.11. Wear factors (mean ± SD), further validating the assertion that surrogate (C/S) specimen testing predicts the same relative ranking as full-scale component testing.

## 7.5 Discussion

Three key results of this research endorse the utility of surrogate C/S pairs for ranking wear tests. First, by design, a surrogate C/S pair can replicate the Hertzian contact mechanics of a full-scale hip implant pair under edge loading conditions (Figures 7.5 and 7.7). Second, in wear tests simulating edge loading, the surrogates ranked in the same order as the full-scale pairs (Figure 7.11). Third, in each material pair, the surrogate pair replicated the trend of evolving friction force seen in the H/L pairs (Figure 7.10). Taken together, these results demonstrate that a specially designed cylinder-spheroid mating pair can replicate the wear phenomena of a full-scale hip implant in a wear test focused on the severe, but realistic, conditions of edge loading.

The main difference between the results of the C/S and H/L pairs was that the $Al_2O_3$ and ZTA cylinders wore more rapidly than their full-scale counterparts, the heads, producing the target wear scar size in half the number of wear cycles. This may be due mainly to the surrogate specimens' greater surface roughness (Figure 7.6 and Table 7.3) because asperity contacts, which induce microscale stresses that induce microstructural damage,[15] increase in severity with increasing roughness. The $Al_2O_3$ and ZTA surrogates' rougher surfaces could also indicate greater residual surface damage from their manufacture, which would have predisposed these specimens to earlier fragmentation. These differences made it difficult to precisely equalize the size of the wear scars, within a given material pair, across all specimen pairs (Figure 7.9); in future tests, this difficulty could likely be lessened by implementing further polishing control measures to produce equivalent surface textures. The Head/CL series had greater wear factors than the Head/FL series (Figure 7.11) for 2 reasons: 1) The edge radius of the CL (2.3 mm) was smaller than that of the FL (3 mm), so

the Head/CL pair had less conforming contact and hence, higher contact stress, and 2) The volumetric wear rate likely accelerated with increasing wear path roughness. Despite such differences among the three test series, the surrogate C/S pairs yielded the same ranking of mean wear factors as each H/L test series (Figure 7.11).

We developed this test method to examine ceramic materials' resistance to the initiation of severe wear – marked by profuse surface fragmentation and grain spalling such as that observed on some retrieved ceramic hip bearings[15] – under clinically relevant contact stresses. Prior research has shown that $Al_2O_3$ exhibits a sharp increase in wear rate once surface fragmentation emerges.[16] We deemed that such a transition marks a failed ceramic surface, and we empirically determined the different test durations so that all test series would be halted shortly after such failure. Hertzian contact pressure follows an ellipsoidal distribution with maximum pressure at the center of the contact patch. This generally caused the central region of each wear scar to fragment the most because it bore the greatest contact stress, leaving the tail regions of the wear scar with mainly abrasive wear. The time at which the surfaces began to fragment is probably indicated by the local plot minima in Figure 7.10. After this point, the friction force rose monotonically, though in the longer tests, the slope appeared to diminish. The C/S pairs mimicked the H/L pairs in this trend (though at a faster pace likely due to the C/S pairs' rougher surfaces), which gives important evidence that the C/S pair closely approximates the contact stress and fatigue effects that elicit severe wear in edge-loaded H/L pairs. Continuing the tests a short time beyond failure (indicated by the friction force minimum) yielded wear scars with enough volume to be measurable, yet not so large that fragmentation had spread across the scar's entire width. Also, the contact stresses in the present test were ~10X greater than those in a prior

pin-on-disk wear test of the same Al2O3, which did not produce profuse surface fragmentation and yielded a wear factor that was an order of magnitude lower.[9]

The difference between the wear factors of the A/A and A/ZTA material pairs was not statistically significant in any component pair. This differs from the results of a microseparation hip simulator wear test, in which ZTA heads exhibited significantly less wear than $Al_2O_3$ heads when both were paired with $Al_2O_3$ liners.[17] The differing result in the present research may be explained by the materials' differing microstructures and the different test durations. The present results show that this ZTA is not significantly different from this $Al_2O_3$ in resistance to severe wear initiation under edge loading. Nonetheless, the $Al_2O_3$ has larger grains and a rougher surface after severe wear than the ZTA (Figure 7.9). The rougher surface of worn $Al_2O_3$ likely exerts more profound wear and damage effects on its counterface than worn ZTA, analogous to the different effects of coarse and fine grades of sandpaper. The difference in effects would become more evident with increased sliding distance, and this probably explains the greater $Al_2O_3$ wear in the simulator tests, which ran for several million cycles and included concentric articulation.

The significantly lower wear factors of the A/Zr material pairs probably result from relatively lower contact stress. The $ZrO_2$ had the lowest elastic modulus, so the A/Zr pair had the lowest predicted contact pressure, 20% and 18% less than that predicted for the A/A and A/ZTA pairs, respectively. The lower contact pressure probably delayed the onset of surface fragmentation, as evidenced by the later appearance of local minima in the friction force plots of A/Zr pairs (Figure 7.10). The comparatively low wear factor of A/Zr in these results should be interpreted cautiously because prior hip simulator results, both with microseparation[18] and without,[19] have shown that A/Zr pairs perform poorer than A/A pairs.

Retrieved $ZrO_2$ heads have exhibited diminished surface hardness as a result of long-term phase transformation,[20] which could explain the relatively poor performance of A/Zr pairs in longer duration tests.

Severe-condition testing may be vital to continued advancement in CoC hip prostheses. For CoC implants, the fully-reduced, concentric articulation conditions of typical hip simulator wear tests are relatively benign because the bearings may be protected from wear by fluid film lubrication.[21] CoC implants tested as such to 20 million cycles have exhibited some grain pullout in the main bearing region, but not the distinct roughened areas observed on some retrieved implants.[15] With the inclusion of microseparation to mimic in-vivo subluxation, CoC hip simulator wear tests have yielded increased wear rates and edge-loading wear scars similar to those on retrieved implants.[22] Even so, those severe-condition tests were performed after the implants' commercial introduction, a point at which the details of the materials and designs have been firmly fixed by the manufacturer. Furthermore, the tests were performed over millions of cycles spanning months on complicated hip simulator equipment. Such practices may not be conducive to innovation and improvement due to the long lead times of full-scale implant manufacturing and the limited availability of such test equipment.

This research has focused on developing a severe-condition test method that can readily be applied quite early in the development of next-generation hip bearing systems. The cylinder and spheroid shapes of the surrogate mating pair can be manufactured from small material specimens such as those typically produced during the research phase of a candidate new material. From a cylindrical raw material blank, the cylinder may be finished by centerless grinding and lapping using widely available tooling. Making the spheroid

is slightly more complicated since it requires a custom form lap. The reciprocating wear test with these specimens requires custom fixtures; yet, the test was performed on a typical uniaxial test frame outfitted with a spring-loaded fixture to supply the normal contact force, so the test required only a single control channel, namely actuator displacement. Another notable advantage of the test method was its short test duration: all trials lasted less than one hour. The SWLI used to measure wear volume was perhaps the most specialized equipment. However, the wear scars may also be measured in two dimensions with widely available optical microscopes (with calibration).

The possibility of using simple shapes to more rapidly test potential new implant bearing materials under the most severe stress conditions they may experience during in-vivo service is a potential boon to the field. Using this approach, researchers will be able to rank and sort a greater number of material prototypes earlier in development, using more relevant test conditions than created with current simple wear test methods. Long-term wear testing will still remain essential for evaluating the multi-factorial failure modes of full-scale implant systems. The present research bridges the gap between the simplest material tests and complicated, long-term implant wear tests by providing a simple wear test, suited to early research and development, that reproduces the edge-loading contact stresses of full-scale hip implants.

## 7.6 Acknowledgements

This work was supported by Award #R21AR056374 from the NIH/NIAMS. The authors thank Frank Gorman, Margaret Harrington, Jeff Kessler, and Dr. Brian van Devener for valuable assistance.

## 7.7 References

1. Blumenfeld TJ, Glaser, DA, Bargar, WL, et al. 2011. In vivo assessment of total hip femoral head separation from the acetabular cup during 4 common daily activities. Orthopedics 34: e127-e132.

2. Dennis DA, Komistek, RD, Northcut, EJ, et al. 2001. "In vivo" determination of hip joint separation and the forces generated due to impact loading conditions. J. Biomech. 34: 623-629.

3. Mak MM, Besong, AA, Jin, ZM, Fisher, J. 2002. Effect of microseparation on contact mechanics in ceramic-on-ceramic hip joint replacements. Proc. Inst. Mech. Eng. H 216: 403-408.

4. Walter WL, O'Toole G, C, Walter, WK, et al. 2007. Squeaking in ceramic-on-ceramic hips: The importance of acetabular component orientation. J. Arthroplasty 22: 496-503.

5. Sanders A, Tibbitts, I, Brannon, R. 2012. Concomitant evolution of wear and squeaking in dual-severity, lubricated wear testing of ceramic-on-ceramic hip prostheses. J. Orthop. Res. 30: 1377-1383.

6. Sanders AP, Brannon, RM. 2011. Determining a surrogate contact pair in a Hertzian contact problem. J. Tribol. 133: 024502-024506.

7. 1999. ISO 14242-1: Implants for surgery - wear of total hip-joint prostheses. Part 1: Loading and displacement parameters for wear-testing machines and corresponding environmental conditions for test. International Organization for Standardization, Geneva, Switzerland.

8. Nevelos J, Ingham, E, Doyle, C, et al. 2000. Microseparation of the centers of alumina-alumina artificial hip joints during simulator testing produces clinically relevant wear rates and patterns. J. Arthroplasty 15: 793-795.

9. Saikko V, Keranen, J. 2002. Wear simulation of alumina-on-alumina prosthetic hip joints using a multidirectional motion pin-on-disk device. J. Am. Ceram. Soc. 85: 2785-2791.

10. Ma L, Rainforth, WM. 2012. The effect of lubrication on the friction and wear of Biolox®Delta. Acta Biomater. 8: 2348-2359.

11. Sanders AP, Brannon, RM. 2011. Assessment of the applicability of the Hertzian contact theory to edge-loaded prosthetic hip bearings. J. Biomech. 44: 2802-2808.

12. Irons ML. 2005. The curvature and geodesics of the torus. http://www.rdrop.com/~half/math/torus/index.xhtml. Accessed Jan. 20, 2008.

13. Lee CL, Sanders, A, Tikekar, NM, Chandran, KSR. 2008. Tribology of titanium boride-coated titanium balls against alumina ceramic: Wear, friction, and micromechanisms. Wear 265: 375-386.

14. 1996. ISO 7206-2: Implants for surgery - partial and total hip joint prostheses. Part 2: Articulating surfaces made of metallic, ceramic, and plastic materials. International Organization for Standardization, Geneva, Switzerland.

15. Shishido T, Clarke, IC, Williams, P, et al. 2003. Clinical and simulator wear study of alumina ceramic THR to 17 years and beyond. J. Biomed. Mater. Res. B Appl. Biomater. 67: 638-647.

16. Cho, SJ, Mooh, H, Hockey, BJ, Hsu, SM. 1992. The transition from mild to severe wear in alumina during sliding. Actal Metall. Mater. 40: 185-192.

17. Stewart TD, Tipper, JL, Insley, G, et al. 2003. Long-term wear of ceramic matrix composite materials for hip prostheses under severe swing phase microseparation. J. Biomed. Mater. Res. B Appl. Biomater. 66: 567-573.

18. Stewart TD, Tipper, JL, Insley, G, et al. 2003. Severe wear and fracture of zirconia heads against alumina inserts in hip simulator studies with microseparation. J. Arthroplasty 18: 726-734.

19. Clarke IC, Good, V, Williams, P, et al. 2000. Ultra-low wear rates for rigid-on-rigid bearings in total hip replacements. Proc. Inst. Mech. Eng. H 214: 331-347.

20. Catledge SA, Cook, M, Vohra, YK, et al. 2003. Surface crystalline phases and nanoindentation hardness of explanted zirconia femoral heads. J. Mater. Sci. – Mater. Med. 14: 863-867.

21. Jin ZM, Dowson, D, Fisher, J. 1997. Analysis of fluid film lubrication in artificial hip joint replacements with surfaces of high elastic modulus. Proc. Inst. Mech. Eng. H 211: 247-256.

22. Stewart T, Tipper, J, Streicher, R, et al. 2001. Long-term wear of hiped alumina on alumina bearings for THR under microseparation conditions. J. Mater. Sci. – Mater. Med. 12: 1053-1056.

23. Mak MM, Jin, ZM. 2002. Analysis of contact mechanics in ceramic-on-ceramic hip joint replacements. Proc. Inst. Mech. Eng. H 216: 231-236.

# CHAPTER 8

# FURTHER RESEARCH OPPORTUNITIES

## 8.1 Introduction

This chapter describes five opportunities for further research that will extend the beneficial outcomes of the research so far completed. In several cases, these are well-prepared projects, with test specimens and equipment already in place. The order of the following subsections ranks these suggested projects by their potential impacts and costs, with first position denoting the combination of highest impact and lowest cost.

## 8.2 Dual-severity surrogate test method

The DSS test method fulfills Quadrant 4 of the project plan (refer to Figure 1.1). It is a test method to subject simply shaped surrogate specimens to contact stresses and articulation that mimic edge loading and concentric articulation combined. These two modes of articulation elicit distinctly different contact stress magnitudes; combining them in one surrogate specimen test gives rise to the name "dual-severity surrogate (DSS)." The DSS test provides greater physiologic relevance than the surrogate edge-load test (Quadrant 3, Chapter 7), since the latter test does not involve the relatively mild conditions of concentric articulation. With increased physiologic relevance comes greater complexity (of equipment, measurements, etc.); yet, the DSS test uses surrogate specimens, so it retains the principal advantage of the surrogate edge-load test. Namely, the DSS test can be performed with simple shapes – cylinders and disks – so it is feasible to use in the early stages of new material development.

The DSS test's scheme is illustrated in Figure 8.1. In overview, Part 1 of the figure depicts test actions to simulate edge loading, and Part 2 depicts actions to simulate concentric articulation. In Part 1, the *center disk* (*a*) is pressed by force $F_1$ into contact with the *edge*

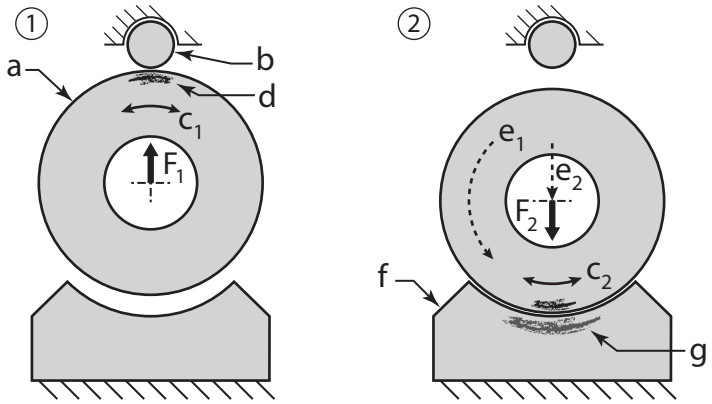


Figure 8.1. DSS test schematic

*cylinder* (*b*) while the center disk is rotated reciprocally ($c_1$). The center disk and edge cylinder are designed such that their contact interface mimics that of edge-loaded CoC bearings. The severe contact stress at this interface is expected to cause damage (*d*) to the center disk (although *d* is drawn on the disk's flat surface, it depicts damage on the cylindrical surface; likewise *g* in Part 2). In Part 2, the center disk is first rotated 180° ($e_1$) and lowered ($e_2$) to contact the concave surface of the *trough* (*f*). Then, the center disk is simultaneously pressed by force $F_2$ into the trough and rotated reciprocally ($c_2$). The center disk and trough are designed such that their contact interaction mimics that of concentrically loaded full-scale implants. It is expected that damage *d* on the center disk will eventually elicit damage *g* on the trough, as happened when the dual-severity test method was applied to full-scale components to investigate the causes of CoC squeaking (Chapter 5). A selected pattern of edge loading (Part 1) and concentric articulation (Part 2) actions will constitute a wear test that mimics, in a simplified way, a wear test of full-scale implants performed in a hip simulator with microseparation conditions [1].

The equipment to perform the DSS test has been designed and built. It is based on the platform used for the dual-severity test of components (DSC test) that investigated the causes of squeaking in CoC implants. Chapter 5 contains a drawing of the apparatus set up for the DSC test, and Figure 8.2 shows the apparatus as set up for a DSS test.

Figure 8.3 depicts the collection of DSS specimens already made and a strategy for using them in a study. Section 8.3 explains how the cylinder/cylinder (C/C) contact pairs in the DSS test can be designed and interpreted as surrogates for the edge-loading and concentric-loading contact pairs of full-scale implants. The surrogate specimens' materials are not identical to those of the full-scale specimen; the $Al_2O_3$ and ZTA materials are from different manufacturers. It was not possible to harvest the DSS specimens from existing ceramic implants as we did to make the surrogate edge-load specimens (Chapter 7). Here, because the raw materials are from different manufacturers and have different intrinsic properties, a ranking comparison would be prone to error. Therefore, the strategy for the proposed study is to perform both series of tests and to show that each reveals differences in the wear performances of the three material pairs. The tests may also reveal qualitative similarities between the DSS and DSC test series; for instance, in each, the material pair with the largest grain sizes may wear fastest. With the present specimens, the potential benefit of the DSS test method will be demonstrated by its ability to discern important differences in material wear performance in combined edge loading and concentric articulation. A future study with all material pairs identically matched could be undertaken with cooperation from a ceramic implant manufacturer. Table 8.1 identifies the components available for performing the proposed study.

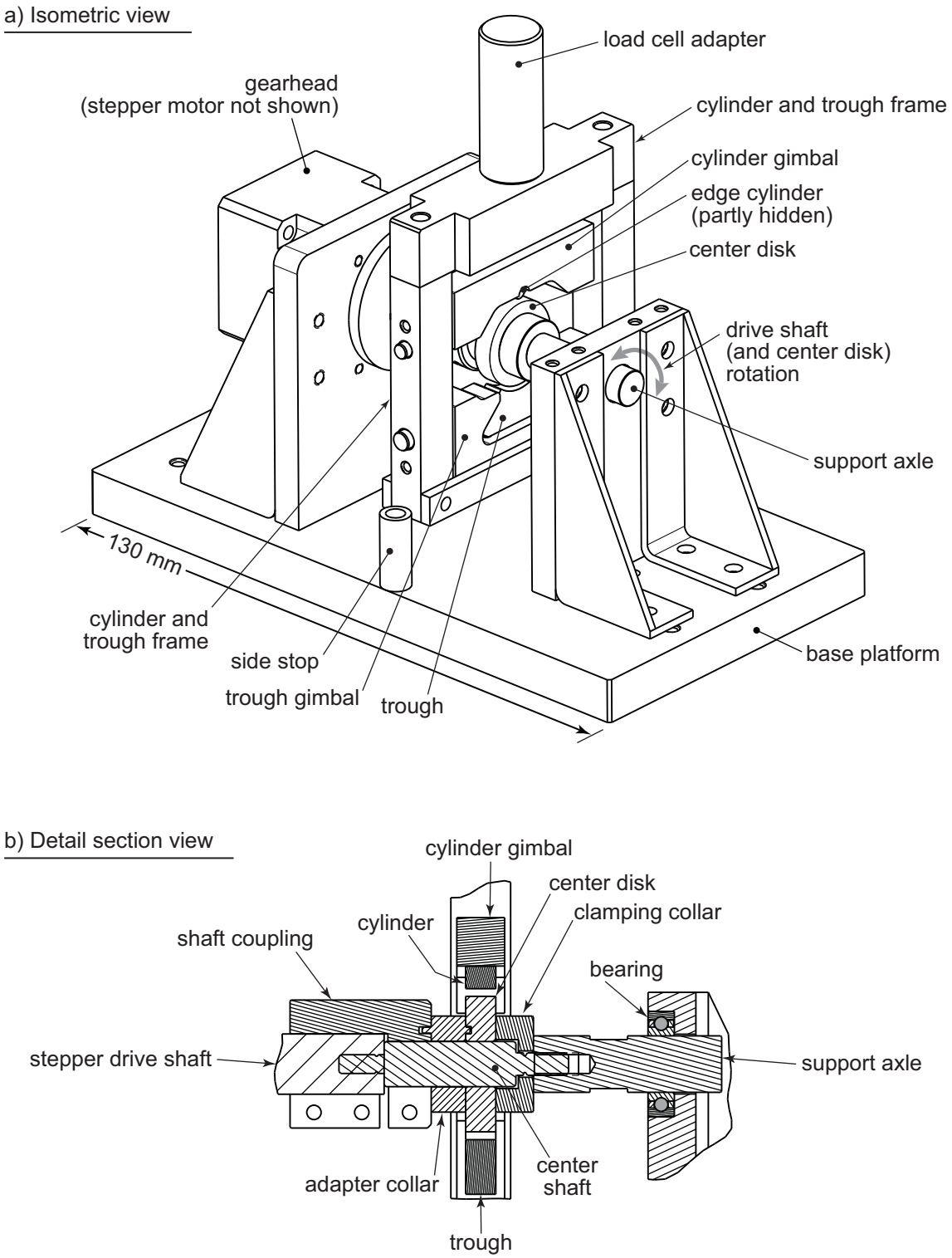


Figure 8.2. DSS test apparatus. a) Isometric view. b) Detail view of a vertical section plane through the center of the rig.

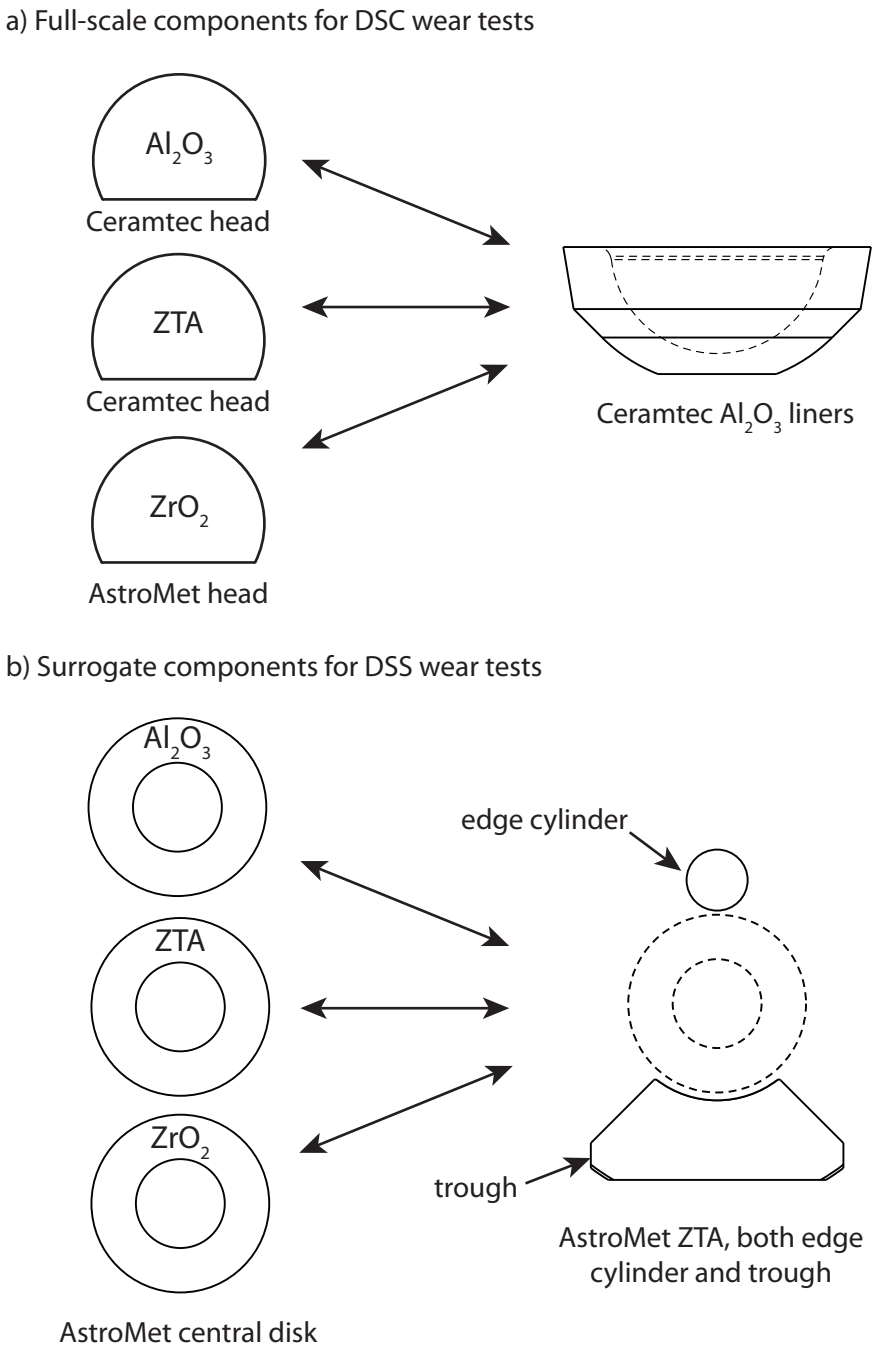


Figure 8.3. Component and material pairs for DSS and DSC test strategy. “AstroMet” and “Ceramtec” are the names of the two raw material manufacturers. a) Pairs for DSC test series; b) Pairs for DSS test series.

Table 8.1. Specimens available for DSS test

| Component | Material | Manufacturer | Quantity |
|---|---|---|---|
| Center disk | $Al_2O_3$, ZTA, $ZrO_2$ | AstroMet | 2 each |
| Trough | ZTA | AstroMet | 12 |
| Edge cylinder | ZTA | AstroMet | 6 |
| Head | $Al_2O_3$, ZTA | Ceramtec | 3 each |
| | $ZrO_2$ | AstroMet | 1 |
| Liner | $Al_2O_3$ | Ceramtec | 2 |

### 8.3 Simplify the surrogate edge-loading test

The cylinders in the cylinder-spheroid (C/S) surrogate pairs (Chapter 7) were purposely designed to be used in an alternative configuration where they would be paired against one another along their cylindrical surfaces (Figure 8.4). In this C/C pair, the contact patch will be rectangular, measuring as wide as the cylinders' length and with a height predictable using Hertzian contact theory [3]. Also, the contact pressure distribution will not vary along the length of the contact patch, although edge effects may arise at the ends of the cylinders, particularly if they are not identical in length. In comparison, the contact patch of the C/S pair is elliptical (Figure 8.4a), and the contact pressure distribution reaches its greatest magnitude at a cross-section through the center of contact [3]. The cylinders are designed such that the C/C pair's contact pressure distribution at any cross-section will be equivalent to the maximal cross-sectional pressure distribution of the C/S pair (Section B-B). This equivalence should make every cross-section of the C/C pair's contact interface a rendition of the worst-case cross-section of the C/S pair's interface. Thus, it is hypothesized that the entire contact patch of the C/C pair will wear at about the same rate as the central portion of the C/S pair's contact patch, which, as shown by Chapter 7, is the portion that wears fastest.

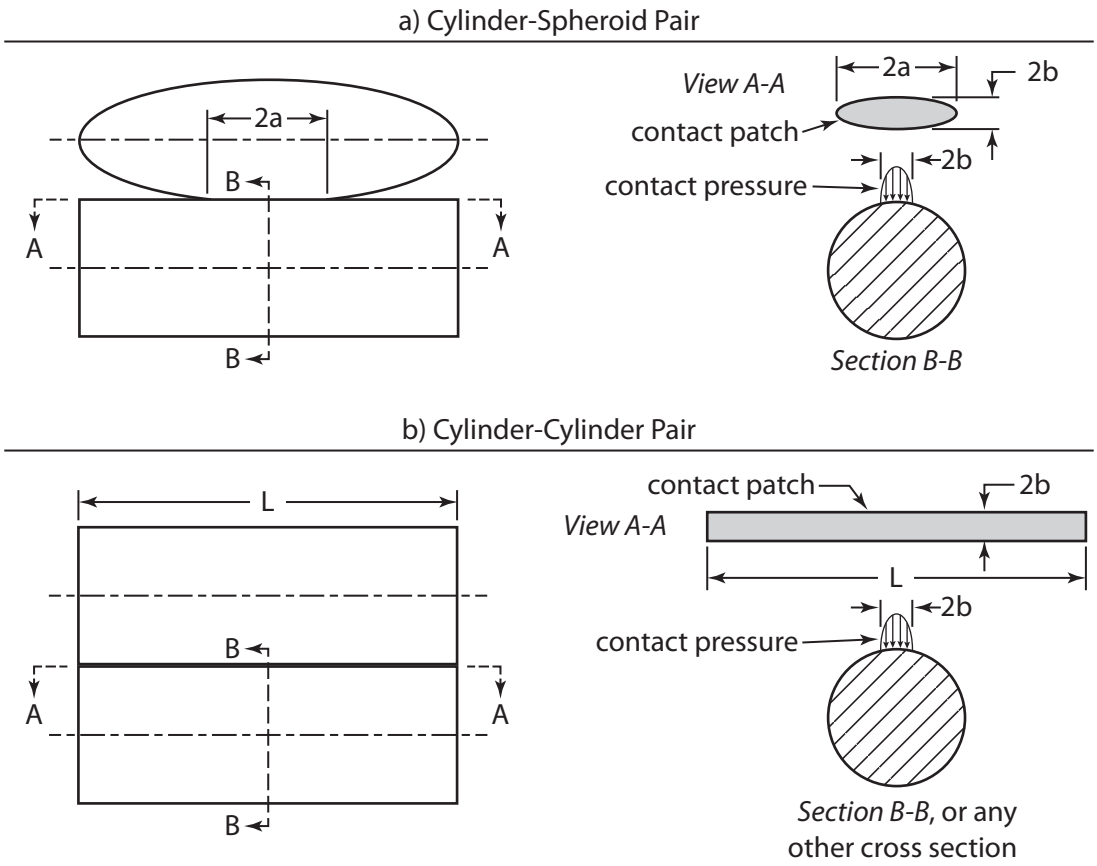


Figure 8.4. Alternative contact pairs. a) C/S pair, pressed together, with its elliptical contact patch and the contact pressure distribution on a cross-section through the center of contact. b) C/C pair, pressed together, with its rectangular contact patch; the contact pressure distribution is the same at any cross-section.

The chief aim in implementing the C/C pair as an alternative to the C/S pair would be to simplify manufacture of the surrogate specimens. A spheroid specimen is relatively difficult to produce because it requires the manufacture and use of a custom tool, a form lap. A cylinder specimen is simpler to produce because it is suited to through-feed centerless grinding and lapping, a process that uses widely available tooling. The design procedure for the C/C pair is similar to that for the C/S pair, but instead of using the Hertzian substitution design equations from Chapter 2, one uses Hertzian contact equations for a C/C pair [3]. The following example illustrates the design of a C/C pair that can serve as a sur-

rogate for edge-loading contact as illustrated in Figure 8.4. The minor semi-axis $b$ and the maximum contact pressure $P_0$ for the elliptical contact path of the edge-loaded head/liner pair are first determined using the techniques in Chapter 3. These values are then used with Hertzian contact formulas for C/C contact, Equations 8.1 and 8.2 [3]:

$$W = \tfrac{1}{2}\pi b P_0 \tag{8.1}$$

$$b = \sqrt{\frac{4 W r_1 r_2}{\pi E^* \left(r_1 + r_2\right)}} \tag{8.2}$$

Here, $W$ is the normal force per unit length, $r_1$ and $r_2$ are the radii of the two cylinders in the C/C pair, and $E^*$ has the meaning given in Chapter 3. The radius of one of the cylinders, say $r_1$, is assigned a chosen value. Then, solving Equations 8.1 and 8.2 simultaneously provides a design equation for $r_2$:

$$r_2 = \frac{b r_1 E^*}{2 P_0 r_1 - b E^*} \tag{8.3}$$

The process can be iterated to find convenient (i.e. easily manufactured) values for both $r_1$ and $r_2$. A similar process can be followed to design the radii of the components in the DSS test method (Section 8.2), except that for the convex-concave pair representing head/liner contact, $b$ is taken to be the radius of the sphere-sphere contact patch, which can be computed with Equation 8.4 [3]:

$$b = \sqrt[3]{\frac{3 Q r_1 r_2}{4 E^* \left(r_1 + r_2\right)}} \tag{8.4}$$

Here, $Q$ is the normal contact force.

With more easily produced specimens, a C/C surrogate edge-loading test would enable a greater number of early-stage design iterations than possible with C/S pairs, assuming a

fixed budget. Therefore, a project to compare C/S and C/C wear test results, to show that the wear on a cross-section of the C/C pair is very similar to that on the central section of the C/S pair, would be a logical step to advance the surrogate edge-loading test concept (Chapter 7).

### 8.4 Compare squeaking of different material pairs

It would be of great value to the arthroplasty field to have comparative data on the propensity of different contemporary CoC material pairs to wear and squeak. That comparison can be provided by performing further tests similar to those reported in Chapter 5, with new material pairs. To the author's knowledge, there is only one previously published article that reports a difference in the occurrence of squeaking with different material pairs; that study used a hip simulator machine, compared $Al_2O_3$-$Al_2O_3$ and $Al_2O_3$-$ZrO_2$ material pairs, and reported that the former did not squeak, but the latter did [2]. Additional studies, with other contemporary materials such as ZTA, should be performed to elucidate the problem of squeaking CoC hips. Our study into the squeaking phenomenon showed that squeaking is linked to roughening of the liner ID. Since Ceramtec ZTA has a more refined microstructure than Ceramtec $Al_2O_3$, the ZTA, once worn, may exhibit a smoother surface, even if it wears at the same rate as $Al_2O_3$. Thus, a preliminary hypothesis is that the ZTA material will exhibit a lower propensity to squeak than the $Al_2O_3$. There are sufficient specimens on hand to investigate this hypothesis, and the study would be a novel contribution to the field.

### 8.5 Perform surrogate wear tests to rank several materials

The intended use of the surrogate edge-loading test method is to screen candidate new materials for their wear performance under the severest contact stresses they are liable to experience in use as hip bearings. It is evident from numerous recent journal articles that there is broad interest in developing new materials for hard-hard bearing pairs for hip prostheses [4-13]. Currently, researchers use either pin-on-disk or hip simulator wear tests to evaluate the performance of candidate new materials. The former test method is simplistic, and the latter is too expensive and time consuming to use in an iterative development project. It would be valuable to the field to employ the surrogate edge-loading test method to rank the wear performance of several contemporary materials, especially including the most recently marketed type, ZTA, and types which to date have only been evaluated in research contexts. The value would be two-fold. First, the research would publicize the utility of the surrogate edge-loading test as an early-stage material screening test. Second, the results would elucidate which of several recently commenced research paths would be most fruitful to pursue for next-generation hard hip bearing materials that could overcome the current limitations, such as edge-loading wear and squeaking. Table 8.2 lists key details about several materials recently introduced or studied, all of which are candidates for inclusion in a broad study as proposed.

### 8.6 Apply Hertzian substitution theory to knee implant testing

Surrogate specimen test methods could be beneficial to the design and evaluation of prosthetic knee implants and their materials. Figure 8.5a shows a typical pair of knee implants; contact between the femur and tibia components occurs in the encircled region and

Table 8.2. Recently introduced or researched materials for hard hip bearings

| Material | Year | References | Notes |
|---|---|---|---|
| ZTA | 2004 | [4,5] | Commercialized |
| $Si_3N_4$ | 2008 | [6] | Hip simulator wear tests against $Si_3N_4$ and CoCr |
| Polycrystalline diamond | 2000 | [14,15] | High pressure sintering process |
| Amorphous diamond | 2003 | [7-10] | Vapor deposition process |
| Chromium nitride coating | 2003 | [11-13] | Vapor deposition on CoCr substrate |

involves the *condyle* portions of each member. Due to the condyles' shapes, the contact patch that arises when they are pressed together can be approximately elliptical. This is illustrated by Figure 8.5b, which shows contours of contact pressure on the tibia component from a finite-element analysis of knee implant loading [16]. The elliptical shape of the contact patches suggests that the geometry of the contacting condyles can be approximated by the Hertzian description of contacting surfaces (Chapter 2). This in turn implies that the surrogate specimen testing approach developed during this research will be applicable to condyle contact. Representing condyle contact with simpler surrogate specimens could be a boon to knee implant research and development in much the same way as to hip implants.

A specific and useful application of the surrogate specimen approach to knee prostheses would be wear and fatigue testing of UHMWPE for tibia components. There is a need to use crosslinked UHMWPE for these implants, to reduce wear. However, because crosslinked UHMWPE exhibits reduced fatigue strength relative to non-crosslinked [17-19], there has been concern about using crosslinked material in knee tibias [20,21], in part because these implants have a history of suffering high rates of surface pitting and

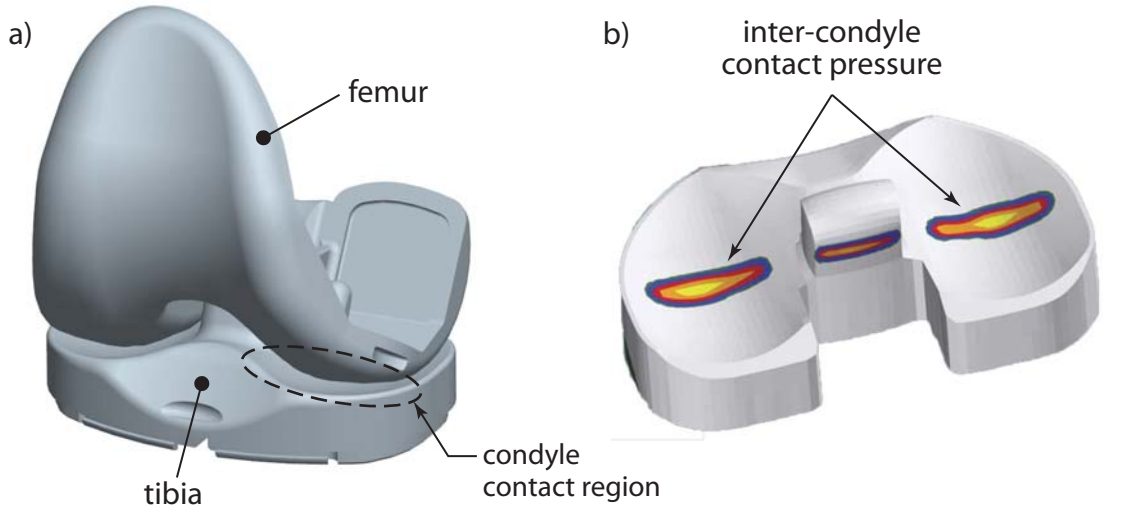


Figure 8.5. Knee prostheses and condyle contact. a) CAD model image of typical femur and tibia components, with the inter-condyle contact region highlighted. b) Contours of inter-condyle contact pressure on the tibia component are approximately elliptical (adapted from [16], used with permission).

delamination failure when made of purportedly improved formulations of UHMWPE [22-24]. Therefore, there is a need for realistic wear testing of crosslinked UHMWPE, in particular to ascertain its resistance to pitting and delamination. Hertzian surrogate specimens could be used to perform such testing in a novel, efficient way, and Figure 8.6 shows a specific and recommended test configuration. The OrthoPOD wear test machine (AMTI, Watertown, MA) shown is a product marketed for pin-on-disk wear testing of orthopaedic implant materials, and many orthopaedic test laboratories possess this machine. It accommodates six specimen pairs, the wear paths of which are programmable but limited to 2D, horizontal sliding. Previously, it was not possible to wear test a condyle contact pair in an OrthoPOD machine, because the concave shape of the tibia condyle would necessitate that the opposing femur condyle translate in the vertical axis (in addition to the horizontal plane), which an OrthoPOD does not permit. The surrogate specimen approach overcomes

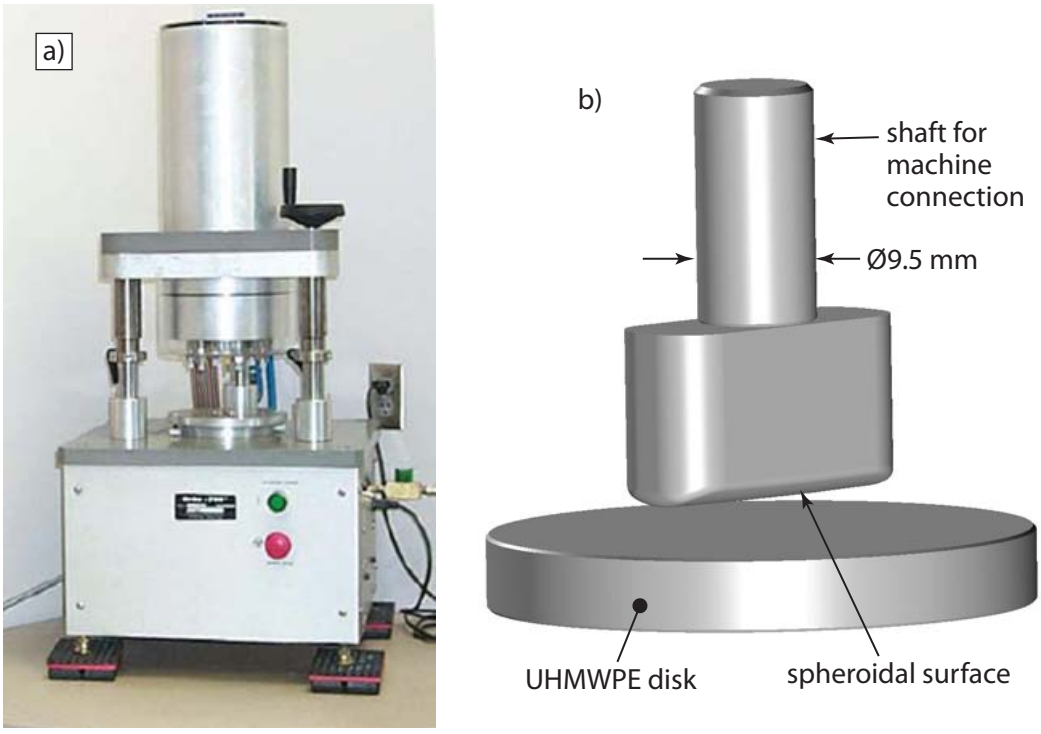


Figure 8.6. Surrogate testing for knee implants. a) OrthoPOD pin-on-disk wear test machine. b) CAD model of specimens designed as surrogates for a knee condyle contact pair (gap added for clarity); the spheroidal surface is the undersurface of the upper specimen.

this limitation. The illustrated specimens are a surrogate pair that simulates a condyle pair, and they are designed to be tested in an OrthoPOD machine. Because the relative motion between spheroid and disk is entirely planar, and thus within the machine's capabilities, this pair makes it possible to wear test a flat UHMWPE disk, under contact stresses simulating those of a condyle pair, in a pin-on-disk machine. The dual advantages of using surrogate specimens in this application – the accurate simulation of condyle contact and the implementation in available test equipment – will make the surrogate specimen approach a valuable and productive method for early-stage wear testing of knee prosthesis designs and materials.

## 8.7 References

[1] Nevelos, J., Ingham, E., Doyle, C., Streicher, R., Nevelos, A., Walter, W., and Fisher, J., 2000, "Microseparation of the Centers of Alumina-Alumina Artificial Hip Joints During Simulator Testing Produces Clinically Relevant Wear Rates and Patterns," J Arthroplasty, 15(6), pp. 793-5.

[2] Stewart, T. D., Tipper, J. L., Insley, G., Streicher, R. M., Ingham, E., and Fisher, J., 2003, "Severe Wear and Fracture of Zirconia Heads against Alumina Inserts in Hip Simulator Studies with Microseparation," J Arthroplasty, 18(6), pp. 726-34.

[3] Johnson, K. L., 1985, *Contact Mechanics*, Cambridge Univ. Press, Cambridge.

[4] Stewart, T. D., Tipper, J. L., Insley, G., Streicher, R. M., Ingham, E., and Fisher, J., 2003, "Long-Term Wear of Ceramic Matrix Composite Materials for Hip Prostheses under Severe Swing Phase Microseparation," J Biomed. Mater Res B Appl Biomater, 66(2), pp. 567-573.

[5] Lombardi, A. V., Jr., Berend, K. R., Seng, B. E., Clarke, I. C., and Adams, J. B., 2010, "Delta Ceramic-on-Alumina Ceramic Articulation in Primary THA: Prospective, Randomized FDA-Ide Study and Retrieval Analysis," Clin Orthop, 468(2), pp. 367-74.

[6] Bal, B. S., Khandkar, A., Lakshminarayanan, R., I., C., Hoffman, A. A., and Rahaman, M. N., 2008, "Testing of Silicon Nitride Ceramic Bearings for Total Hip Arthroplasty," J Biomed Mater Res B Appl Biomater, 87B(2), pp. 447-454.

[7] Lappalainen, R., Anttila, A., and Heinonen, H., 1998, "Diamond Coated Total Hip Replacements," Clin Orthop, 352, pp. 118-27.

[8] Santavirta, S. S., Lappalainen, R., Pekko, P., Anttila, A., and Konttinen, Y. T., 1999, "The Counterface, Surface Smoothness, Tolerances, and Coatings in Total Joint Prostheses," Clin Orthop, 369, pp. 92-102.

[9] Lappalainen, R., Selenius, M., Anttila, A., Konttinen, Y. T., and Santavirta, S. S., 2003, "Reduction of Wear in Total Hip Replacement Prostheses by Amorphous Diamond Coatings," J Biomed. Mater Res B Appl Biomater, 66(1), pp. 410-3.

[10] Santavirta, S., 2003, "Compatibility of the Totally Replaced Hip. Reduction of Wear by Amorphous Diamond Coating," Acta Orthop Scand Suppl, 74(310), pp. 1-19.

[11] Williams, S., Tipper, J. L., Ingham, E., Stone, M. H., and Fisher, J., 2003, "In Vitro Analysis of the Wear, Wear Debris and Biological Activity of Surface-Engineered Coatings for Use in Metal-on-Metal Total Hip Replacements," Proc Inst Mech Eng H, 217(3), pp. 155-163.

[12] Williams, S., Isaac, G., Hatto, P., Stone, M. H., Ingham, E., and Fisher, J., 2004, "Comparative Wear under Different Conditions of Surface-Engineered Metal-on-Metal Bearings for Total Hip Arthroplasty," J Arthroplasty, 19(8), pp. 112-117.

[13] Leslie, I. J., Williams, S., Brown, C., Anderson, J., Isaac, G., Hatto, P., Ingham, E., and Fisher, J., 2009, "Surface Engineering: A Low Wearing Solution for Metal-on-Metal Hip Surface Replacements," J Biomed. Mater Res B Appl Biomater, 4, pp. 4.

[14] Taylor, J. K., and Pope, B. J., 2000, "The Development of Diamond as a Bearing for Total Hip Arthroplasty," 67th Annual Meeting of the American Academy of Orthopaedic Surgeons, Orlando, Florida.

[15] Pope, B. J., and Taylor, J., 2007, "The Development of Diamond as a Bearing for Arthroplasty Applications," BoneZone, 4(4), pp. 32-35.

[16] Morra, E. A., and Greenwald, A. S., 2005, "Polymer Insert Stress in Total Knee Designs During High-Flexion Activities: A Finite Element Study," J Bone Joint Surg Am, 87(suppl_2), pp. 120-124.

[17] Baker, D. A., Hastings, R. S., and Pruitt, L., 1999, "Study of Fatigue Resistance of Chemical and Radiation Crosslinked Medical Grade Ultrahigh Molecular Weight Polyethylene," J Biomed Mater Res, 46(4), pp. 573-81.

[18] Gencur, S. J., Rimnac, C. M., and Kurtz, S. M., 2006, "Fatigue Crack Propagation Resistance of Virgin and Highly Crosslinked, Thermally Treated Ultra-High Molecular Weight Polyethylene," Biomaterials, 27(8), pp. 1550-1557.

[19] Atwood, S. A., Van Citters, D. W., Patten, E. W., Furmanski, J., Ries, M. D., and Pruitt, L. A., 2011, "Tradeoffs Amongst Fatigue, Wear, and Oxidation Resistance of Cross-Linked Ultra-High Molecular Weight Polyethylene," J Mech Behav Biomed Mater, 4(7), pp. 1033-45.

[20] Ries, M. D., and Pruitt, L., 2005, "Effect of Cross-Linking on the Microstructure and Mechanical Properties of Ultra-High Molecular Weight Polyethylene," Clin Orthop, 440, pp. 149-56.

[21] Puertolas, J. A., Medel, F. J., Cegonino, J., Gomez-Barrena, E., and Rios, R., 2006, "Influence of the Remelting Process on the Fatigue Behavior of Electron Beam Irradiated UHMWPE," J Biomed. Mater Res B Appl Biomater, 76(2), pp. 346-53.

[22] Wright, T. M., Astion, D. J., Bansal, M., Rimnac, C. M., Green, T., Insall, J. N., and Robinson, R. P., 1988, "Failure of Carbon Fiber-Reinforced Polyethylene Total Knee-Replacement Components. A Report of Two Cases," J Bone Joint Surg Am, 70(6), pp. 926-32.

[23] Wrona, M., Mayor, M. B., Collier, J. P., and Jensen, R. E., 1994, "The Correlation between Fusion Defects and Damage in Tibial Polyethylene Bearings," Clin Orthop Relat Res, 299(299), pp. 92-103.

[24] Muratoglu, O. K., Mark, A., Vittetoe, D. A., Harris, W. H., and Rubash, H. E., 2003, “Polyethylene Damage in Total Knees and Use of Highly Crosslinked Polyethylene,” J Bone Joint Surg Am, 85-A Suppl 1, pp. S7-S13.

# CHAPTER 9

# CONCLUSIONS

## 9.1 Introduction

This research has provided theoretical analysis and laboratory validation for a novel approach to severe wear testing. The new approach employs simply shaped surrogate test specimens in lieu of full-scale components to facilitate wear testing during the early stages of material or component research and development. As an application, a wear test method using surrogate specimens to replicate the severe contact stresses of edge-loaded ceramic hip bearings was developed. The test method was validated by showing that the rank order of wear resistance in surrogate specimens, in three ceramic material pairs, was equivalent to that of edge-loaded full-scale implants in the same material pairs. This and other important outcomes of the research program are outlined and recapitulated in the following two subsections.

## 9.2 Delivered objectives

Tables 9.1 and 9.2 summarize the research program's chief objectives and associated outcomes. Table 9.1 focuses on the originally proposed objectives; most of these (1-3) were fully met, others (4-5) were mostly met, and one (5) was substantially adjusted during the course of the research to reflect new understanding from recently published scientific literature. Table 9.2 summarizes ancillary objectives that arose in the course of the research; each of these supported and expounded the original objectives via the publication of relevant discoveries.

Table 9.1. Summary of objectives and their outcomes

| Objective | Outcome |
|---|---|
| *Original, fully achieved* | |
| 1. *Lead task*: Find means to design surrogate contact and wear specimens | • Formulas for the design of spheroid-plane and spheroid-cylinder surrogate contact pairs<br>• Published in Journal of Tribology (Chap. 2) |
| 2. *Quadrant 1*: Determine accuracy of Hertzian theory for edge-loaded CoC implants | • Hertzian theory has <10% error (conservatively) for edge-load contact dimensions. Similar accuracy for stresses is expected<br>• Published in Journal of Biomechanics (Chap. 3) |
| 3. *Quadrant 3*: Validate surrogate wear test by ranking wear of three material pairs | • Matching wear rankings in surrogate and implant wear tests<br>• Ranking of $ZrO_2$ (historically a poorer wearing ceramic) as lower wearing than $Al_2O_3$ and ZTA prompted a caution that additional testing is necessary.<br>• Manuscript, prepared for submission to Journal of Orthopaedic Research (Chap. 7) |
| *Original, mostly achieved* | |
| 4. *Quadrant 2*: Build and validate FEM for dynamic edge loading; determine contact forces and stresses | • Global model with 10-15% stress error; contact force hence reliable and implemented in edge-loading wear tests.<br>• Sub-modeled contact stresses not accurately modeled due to software's lack of traction boundary conditions<br>• Documented in M.S. thesis: Deepika Kakarla [1] |
| 5. *Quadrant 4*: Repetitive impact tests of implants and surrogate specimens | • Objective modified to a dual-severity wear test<br>• Dual-severity test exposed cause of squeaking (#11 below)<br>• Built equipment, specimens for dual-severity test (Chap. 8) |

Table 9.2. Ancillary objectives

| | |
|---|---|
| 6. *Lead task*: Clarify Hertzian contact theory | • Clear derivation of Hertzian geometry using direct notation<br>• Published in Journal of Tribology (Chap. 2) |
| 7. *Quadrant 1*: Test and analyze CoM and CoP edge loading | • Demonstration that Hertzian theory is less accurate for CoM and CoP than for CoC<br>• Published in Journal of Biomechanics (Chap. 3) |
| 8. *Quadrant 2*: Analyze and test 2-rod impact with Hertzian contact | • Analytical model for rod impact with Hertzian contact<br>• Validated FEM and calibrated instrumentation. Expertise applied to dynamic edge loading analysis and testing (#4 above).<br>• Accepted for publication, 2011 Proceedings of SEM (Chap. 4) |
| 9. *Quadrant 3*: Investigate potential design/manufacturing flaw on ceramic liners | • Laboratory evidence that crest on liner's edge exacerbates edge-loading wear<br>• Published in Journal of Arthroplasty (Chap. 6) |
| 10. *Quadrant 3*: Analyze effects of friction on mechanics of edge loading | • Laboratory evidence that edge-loading normal force is strongly influenced by friction<br>• Documented in M.S. thesis: Ira Tibbitts [2] |
| 11. *Quadrant 4*: Investigate root cause of CoC squeaking | • In-vitro CoC squeaking, achieved with lubrication<br>• A theory relating squeaking with roughening<br>• Published in Journal of Orthopaedic Research (Chap. 5) |

## 9.3 Specific and novel contributions

The novel contributions of this research program (including anticipated, long-term contributions) are summarized in the following two subsections, one of which is specific to the arthroplasty field, and the other to the more general field of mechanical engineering.

### 9.3.1 Arthroplasty field

1. A surrogate wear test method, suited to simply shaped material specimens, that replicates the severe contact stresses encountered by CoC hip bearings during edge loading. The method includes the means to design the surrogate specimens. This contribution will improve the design process of new CoC implant materials by augmenting the relevance of early-stage testing and facilitating an increased number of early-stage material design iterations.
2. Validated theory for the root cause of squeaking. This contribution will help to improve future hip simulator wear test methods by clarifying the conditions that can lead to squeaking.
3. A dual-severity wear test method, suited to simply shaped material specimens, that replicates the contact stresses of concentric articulation and edge loading, combined. This test method may have a beneficial effect on par with or greater than that of the surrogate edge loading test (item 1 in this list). Ranking candidate new materials in both articulation modes may be important because success in one mode may not predict success in the other mode or both modes combined.
4. Demonstration that Hertzian contact theory is suitably accurate (<10% error in contact patch dimensions, conservatively) for analysis of edge-loaded CoC bearings. This contribution will simplify the analysis of edge loading and its effects on component stresses and wear.

5. Hertzian substitution theory. The means to design surrogate contact pairs will foster more effective testing of knee arthroplasty implants, for the same reasons that apply to hip prostheses.
6. Identification of ceramic liner design/manufacturing flaw. Manufacturers who eliminate the sharp crest on the edge of ceramic liners will prolong CoC bearing surface integrity.
7. Contact force magnitude during edge loading (documented in M.S. thesis, Deepika Kakarla [1]). Although there is growing understanding about the substantial detrimental effects of edge loading, there is little data about the forces the bearings experience during edge loading. This contribution provides such data, which is useful for design, analysis, and testing of hip arthroplasty bearings.
8. Analytical model of in-vitro edge-loading mechanics (documented in M.S. thesis, Ira Tibbitts [2]). This contribution will be valuable for potential future work to design hip simulators for wear tests that implement recurrent microseparation edge loading.
9. Data on the limited accuracy of Hertzian theory for edge-loaded CoM bearings and poor suitability for CoP. The CoM test results reasonably imply that Hertzian theory would have similar limitations if applied to MoM edge loading. Likewise, the CoP results obtained in this work can be extrapolated to the case of MoP edge loading. It is of value to understand the range of applicability of existing analytical methods to specific cases of edge loading.

### 9.3.2 Mechanical engineering field

1. Hertzian substitution theory. The capability to perform contact and wear tests using simply shaped surrogate specimens that mimic the contact mechanics of a more complicated original contact pair is broadly applicable, specifically to tribology engineering.

2. Clear, concise derivation of Hertzian contact theory's geometric propositions. It is valuable to have a clear derivation of the simplifying equations that describe the geometry of contacting surfaces in this important theory. The new derivation clearly shows the second-order accuracy of those equations. These details are rarely described in contexts that teach or use Hertzian contact theory, perhaps because previously, the derivations have been in scalar algebraic form; hence, they were more cumbersome.
3. Analytical model, using delay differential equations, of the low speed impact of 2 slender rods, including Hertzian contact. The model may be useful in other contexts involving impact testing or simulation. For instance, it may be useful for verifying numerical simulation codes used to treat impact of bodies with more complicated shapes.

## 9.4 References

[1] Kakarla, D., 2012, "Contact Force Analysis under Femoral Head Micro-Lateralization for Ceramic-on-Ceramic Hip Implants: Finite Element Analysis and Experimental Validation," M.S. thesis, University of Utah, Salt Lake City.

[2] Tibbitts, I. B., 2012, "Dual-Severity Loading Conditions in THA Implants and Their Propensity to Cause Wear-Induced Squeaking in Ceramic-on-Ceramic Bearing Couples," M.S. thesis, University of Utah, Salt Lake City.